TUM School of Natural Sciences

IMPROVEMENTS OF MAS SOLID-STATE NMR EXPERIMENTS BY OPTIMAL CONTROL

Matthias Johannes Gerhard Brandl

Vollständiger Abdruck der von der TUM School of Natural Sciences der Technischen Universität München zur Erlangung des akademischen Grades eines

Doktors der Naturwissenschaften (Dr. rer. nat.)

genehmigten Dissertation.

Vorsitz:	Priv.-Doz. Dr. Gerd Gemmecker
Prüfer der Dissertation:	1. Prof. Dr. Bernd Reif
	2. Prof. Dr. Steffen J. Glaser

Die Dissertation wurde am 18.08.2022 bei der Technischen Universität München eingereicht und durch die TUM School of Natural Sciences am 17.10.2022 angenommen.

Abstract

Magic angle spinning (MAS) solid-state nuclear magnetic resonance (NMR) has become a prime method for the investigation of large protein complexes and aggregates, such as amyloid fibrils. However, it is an intrinsically insensitive method and the amount of sample is limited both by the high cost of isotopic labeling and by the available space within a rotor. This limitation has led to numerous approaches for increasing the sensitivity and overcoming instrumental deficits. One recent such approach is based on reducing the influence of radiofrequency (rf) inhomogeneity in the NMR coil on the experimental efficiency by the creation of optimal control (OC) numerically optimized pulses, while taking the rotational modulation of the rf fields within the coil into account. This approach was proven by Tošner et al. to increase the efficiency of $^{15}N - ^{13}C$ transfers at slow MAS (20 kHz) by approximately 50 %. Here, the same approach was extended to $^{1}H - ^{15}N$ transfers at fast MAS (55 – 60 kHz). In particular, a differential alignment of the rf distribution for different channels was considered to reveal why $^{1}H - ^{15}N$ transfers do not perform as well as pulse schemes that focus only on heteronuclei. Additionally, transverse mixing pulses to enable the application of sensitivity-enhanced recording schemes in solid-state NMR were optimized. Furthermore, spin-state selective transfers were designed to allow dipolar-based transverse relaxation-optimized spectroscopy (TROSY)-type experiments. It was found that all the OC pulses tested for the property are usable at a range of MAS frequencies around the design frequency with minimal loss in experimental performance, as long as their duration and rf amplitudes are scaled accordingly.

In addition, this work led to the development of novel sealing spacers for the Bruker 1.3 mm rotor system that enlarge the available sample volume while ensuring water retention for sensitive biological samples. When combined with pulses that are sufficiently robust to rf inhomogeneity, this increase in sample amount will lead to an increase in sensitivity when compared to the previous spacers. Last, the development

of a 0.7 mm rotor filling tool for the ultracentrifuge was started and, once finished, will allow a much cleaner and more convenient filling of that rotor size.

Zusammenfassung

Die Festkörper-NMR-Spektroskopie unter Rotation im magischen Winkel ist mittlerweile zu einer wesentlichen Methode zur Untersuchung großer Proteinkomplexe und -aggregate, wie beispielsweise amyloider Fibrillen, geworden. Sie ist allerdings eine immanent unempfindliche Methode und die Probenmenge ist sowohl durch die hohen Kosten der Isotopenmarkierung als auch durch das verfügbare Probenvolumen im Rotor begrenzt. Diese Einschränkung führte zu zahlreichen Ansätzen, um die Empfindlichkeit zu erhöhen und instrumentelle Defizite zu überwinden. Ein kürzlich vorgestellter Ansatz basiert auf der Reduktion des Einflusses der Inhomogenität des durch die Messspule erzeugten Radiofrequenzfelds auf die experimentelle Effizienz, indem in die Optimierung von Pulsen durch Methoden der Optimalen Steuerung diese inhomogenen Felder einbezogen werden. Dieser Ansatz wurde durch Tošner et al. zur Erhöhung der Effizienz von $^{15}N-^{13}C$-Transfers um ca. 50 % bei niedriger Rotationsfrequenz von 20 kHz verwendet. In dieser Arbeit wurde der Ansatz auf $^{1}H-^{15}N$-Transfers bei schneller Rotation (55 – 60 kHz) erweitert. Insbesondere wurden unterschiedliche Ausrichtungen der Radiofrequenzfelder der verschiedenen Frequenzkanäle in Betracht gezogen, um die verglichen mit rein heteronuklearen Schemen niedrigere Effizienz der $^{1}H-^{15}N$-Transfers zu erklären. Zudem wurden Pulse zur transversalen Mischung optimiert, die die Verwendung von empfindlichkeitsverbesserten Messverfahren in der Festkörper-NMR-Spektroskopie erlauben. Außerdem wurden spinzustandsselektive Transfers optimiert, die auf der dipolaren Kopplung basieren und die Durchführung von TROSY-Experimenten erlauben. Ferner wurde festgestellt, dass alle auf die entsprechende Eigenschaft untersuchten Pulse mit minimalen Effizienzverlusten in einem Bereich von Rotationsfrequenzen in der Nähe der Frequenz der ursprünglichen Optimierung einsetzbar sind, solange ihre Dauer und ihre Radiofrequenzamplituden entsprechend skaliert werden.

Zusätzlich führte diese Arbeit zur Entwicklung neuer Dichtstopfen für das 1.3 mm-Rotorsystem der Firma Bruker, die unter Erhaltung des Wasserrückhaltevermögens für

empfindliche biologische Proben das verfügbare Probenvolumen vergrößern. Bei einer Kombination dieser Stopfen mit Pulsen, die ausreichend robust gegenüber inhomogenen Radiofrequenzfeldern sind, wird diese Erhöhung des Probenvolumens gegenüber den vorherigen Verhältnissen auch zu einer Erhöhung der experimentellen Empfindlichkeit führen. Zuletzt wurde die Entwicklung einer Vorrichtung zum Füllen von 0.7 mm-Rotoren in einer Ultrazentrifuge begonnen, die nach ihrer Fertigstellung ein saubereres und angenehmeres Befüllen dieser Rotorgröße erlauben wird.

Acknowledgements

First, I would like to thank Bernd Reif very much for trusting me, a biochemist with no prior experience in the field, with a highly technical project, for supporting and pushing me all this way. The discussions greatly helped progress, even though at times it didn't feel that way. I also would like to thank the whole Reif group, past and present, for being a fantastic collection of people: Manuel Hora, Markus Fleisch, Arpita Sundaria, Kai Xue, Saba Suladze, Tejaswini Pradhan, Natascha Rodina, Timur Yasko, Olga Sieluzycka and our office mate Munirah Rahim. Thank you to Asita Djamschidi, Waltraud Wolfson and Karen Biniossek for their administrative support over the years. A very special thank you should go to Riddhiman Sarkar for becoming a good friend, for his NMR expertise and his superb knowledge of the literature (both of which certainly helped in giving great suggestions for improving this thesis). A big thank you also goes to Benita Koch for managing the laboratory and for producing ever new SH3 protein. Thank you to Dennis Huber and Simon Maroldt for having been such highly motivated students.

I want to thank Steffen Glaser, Zdeněk Tošner and Jan Blahut for their collaboration on many of the topics presented in this thesis, and for keeping me on my toes and bringing in fresh ideas in the last few years. Furthermore, my gratitude goes to Michael Sattler and Johannes Buchner for trusting me with the SFB1035 SAXS instrument. I also want to acknowledge the DFG for funding my position and the computational resources provided by the LRZ that were used for all of the heavy calculations in this thesis.

Thank you to the whole of BNMRZ for creating pleasant working environment throughout the years. In particular, I would like to thank Gülden Yilmaz, Winfried Meining and Gerd Gemmecker and our former colleagues Ralf Stehle and Rainer Haeßner for their skills and expertise in keeping a research center operating. Thank you also to all

the unnamed people with whom I have crossed paths and who influenced me in one way or another.

I am grateful to my parents Hans and Marianne for their unending support in all the years. Without their guidance and their confidence in me throughout my whole life, I would not be the same person that I am today. Last, it remains to say my deepest thank you to my partner Steffi for enduring my moods and rough edges while writing this thesis, for her support and for being there in times of need, but also for enriching my life with her creativity and thoughtfulness.

Contents

List of Figures

List of Tables

List of Abbreviations

^{13}C,^{15}N-Gly	uniformly labelled ^{13}C and ^{15}N-labelled glycine 79, 83
ADC	analog-to-digital converter 15
COS	coherence order selective 49, 50
CP	cross polarization 11, 12, 21, 26, 28, 33–43, 45, 48, 61, 62, 65, 81, 85
CSA	chemical shift anisotropy 6, 8, 17, 37, 53
CW	continuous wave 12, 41
EA	echo-antiecho 49
f-(^{13}C,^{15}N)MLF	uniformly ^{13}C and ^{15}N-labelled, N-terminally formylated methionine-leucine-phenylalanine tripeptide 48, 50, 83
f-(^{2}H,^{13}C,^{15}N)-MLF	uniformly ^{2}H, ^{13}C and ^{15}N-labelled, N-terminally formylated methionine-leucine-phenylalanine tripeptide 42, 51, 83
FFKM	perfluoroelastomer 69, 70, 84
FID	free induction decay 2, 13, 49
FSLG	frequency-switched Lee-Goldburg 26
GRAPE	Gradient Ascent Pulse Engineering 24
HH	Hartmann-Hahn 11, 12, 28, 42
HPC	high performance computing 85
IAPP	islet amyloid polypeptide 36
INEPT	Insensitive nuclei enhancement by polarization transfer 10, 11, 30, 49
MAS	magic angle spinning iii, 7, 8, 10, 12, 17, 18, 23, 26, 28, 33, 34, 42, 43, 46–48, 50–52, 63, 67, 73, 77, 83, 84

NMR	nuclear magnetic resonance iii, 1–3, 6, 9, 13, 15–18, 21, 23, 24, 30, 32, 33, 37, 46, 49, 50, 52, 54, 65, 67–69, 72, 76, 77, 79, 80, 83, 85
OC	optimal control iii, 21, 23–28, 31–39, 41–48, 50, 51, 54, 56, 61, 62, 64, 72, 77–79, 81
OCXO	oven controlled crystal oscillator 15, 16
PAS	principal axis systen 5
PDB	Protein Data Bank 85
PEEK	polyether ether ketone 72, 75, 76
PEP	preservation of equivalent pathways 49, 50
PTFE	polytetrafluoroethylene 79
REDOR	Rotational Echo Double Resonance 26
rf	radiofrequency iii, 1, 3, 6, 7, 10–12, 15–17, 21, 23–28, 31, 33, 34, 40–43, 45–48, 50, 58, 59, 67, 68, 71, 72, 76–81, 85
S/N	signal-to-noise ratio 14, 35, 36, 39, 43, 46, 49–51, 54, 63, 65, 71, 78, 81
Tcl	Tool command language 28, 30
TEDOR	Transferred Echo Double Resonance 64
TPPI	time-proportional phase incrementation 49
TROSY	transverse relaxation-optimized spectroscopy iii, 52, 54, 62–65, 81
VT	variable temperature 19

List of Symbols

A_{kq}	Spatial spherical tensor operator
b_{IS}	Dipolar coupling constant
B_0	Static magnetic field
C	Desired final state
f_{Larmor}	Larmor frequency (Hertz)
$\hbar$	Dirac's constant
$\mathscr{H}$	Hamiltonian
$I_{x,y,z}$	Cartesian components of spin angular momentum operator
$\boldsymbol{I}$	Vector operator for spin angular momentum
J	Scalar coupling constant
$J(\omega)$	Spectral density function
p	Dipolar coupling constant
r	Internuclear distance
$\boldsymbol{R}$	Rotation matrix
$S_{x,y,z}$	Cartesian component of spin angular momentum operator
$\hat{T}$	Dyson time-ordering operator
T_{kq}	Spatial spherical tensor operator
U	Unitary propagator
γ	Gyromagnetic ratio
δ	Chemical shift
$\boldsymbol{\delta}$	Chemical shift tensor
δ_{iso}	Isotropic chemical shift
δ_{aniso}	Chemical shift anisotropy
ϵ	Optimization step width
η	Chemical shift asymmetry (or biaxiality)

θ	Angle relative to B_0
θ_R	Angle of the spinning axis relative to B_0
θ_m	Magic angle
ϑ	Rotor azimuth
μ_0	Vacuum permeability
ξ	Scaling factor for MAS rate adjustment of OC shapes
ρ	Spin density matrix
σ_{iso}	Isotropic chemical shielding
σ^{PAF}	Principal component of chemical shielding tensor
τ_c	Rotational correlation time
Φ	Target function
χ	Back-propagated operator
ω_0	Larmor frequency (angular frequency units)
ω_1	Radiofrequency amplitude (angular frequency units)
ω_{MAS}	Magic angle spinning rate (angular frequency units)
ω_{CS}^{aniso}	Anisotropic chemical shift (angular frequency units)
ω_{ref}	Frequency of the rotating frame
ω_{IS}	Dipolar coupling frequency
Ω_0	Offset frequency
Ω_{CS}	Chemical shift offset

1 Theory of NMR spectroscopy

Nuclear magnetic resonance (NMR) spectroscopy is an enormously powerful analytical method in chemistry and life sciences. Apart from the investigation of biological macromolecules in solution[1] and in the solid state[2], the latter of which is the prime motivation for the work in this thesis, NMR spectroscopy has found uses, among many other fields, in organic chemistry[3], metabolomics[4], food science[5], polymer science[6,7], catalysis studies[8], and battery research[9]. NMR spectroscopy utilizes the magnetic moment of nuclei with non-zero spin.

When nuclei with non-zero spin angular momentum are introduced into a magnetic field, an energy difference between the eigenstates of that spin emerges (Zeeman splitting, first discovered in optical spectroscopy[10]). A certain nuclear species with gyromagnetic ratio γ exhibits a characteristic resonant frequency (Larmor frequency: f_{Larmor} in Hz or ω_0 in angular frequency units) at a given magnetic field B_0:

$$f_{Larmor} = -\frac{\gamma}{2\pi} B_0 \tag{1a}$$

$$\omega_0 = -\gamma B_0 \tag{1b}$$

At typical magnetic fields (nowadays, up to 28.2 T magnets are available commercially for NMR applications), this frequency lies within the radiofrequency (rf) part of the electromagnetic spectrum. Its measurement is possible by rf irradiation of nuclei placed in a static magnetic field in an absorption spectroscopic manner[11] or by measuring the deflection of a beam of atoms passed through a static magnetic field and an orthogonal oscillating field[12,13]. However, by far the most applied method makes use of nuclear induction[14–16]. By applying a strong rf pulse at the Larmor frequency to the sample

in thermal equilibrium, a net transverse magnetization, called a coherence, is formed. It coherently precesses around the static field at the Larmor frequency and can be measured, e.g., with a detection coil, producing a free induction decay (FID) signal.

The analytical power of NMR spectroscopy is based on the fact that the resonance frequency of a nuclear spin does not only depend on the nuclear species, but also on the electronic, and thus the chemical, environment of the spin[17–20]. As a conjecture, these "chemical shifts" were thought to be a nuisance by the researchers who discovered them. Quite to the contrary, it is possible to gain vast insights into the environment of the nuclei and thus the structure of the chemical compound by measuring and analyzing these minute differences in resonant frequencies. The chemical shift is defined in equation 2, with $\omega_{0,ref}$ being the resonant frequency of a reference compound:

$$\delta = \frac{\omega_0 - \omega_{0,ref}}{\omega_{0,ref}} \tag{2}$$

Furthermore, the nuclei interact with each other by coupling effects, either acting directly through space (dipolar coupling), or via electrons involved in the chemical bonds (scalar or J coupling)[21–24]. These interactions have an effect on the resonant frequency of the interacting nuclei, and can be used for transferring coherent superpositions among various nuclear spin states. Tailoring the coherent superpositions according to the experimentalist's will allows the correlation of resonances of coupled nuclei, and thus the assignment of resonances to atoms within a structure.

To achieve this, the spin states have to be manipulated in a specific manner to maintain the desired information within the recorded spectra, while simultaneously avoiding any interference from undesired interactions. Because the behavior of the spins is governed by the laws of quantum mechanics, the result of a given experiment can be calculated with high precision according to the Liouville-von Neumann equation[25]:

$$\frac{\mathrm{d}}{\mathrm{d}t}\rho(t) = -\mathrm{i}[\mathscr{H}(t), \rho(t)] \tag{3}$$

Here, $\rho(t)$ is the density operator that describes the macroscopic state of the spin system. $\mathscr{H}(t)$ is the Hamilton operator, or Hamiltonian, which defines the interactions that dictate the evolution of the system. $\mathscr{H}(t)$ contains external contributions such as the static magnetic field B_0 and rf irradiation that can be controlled by the experimentalist, and internal contributions, such as the coupling and the chemical shift:

$$\mathscr{H} = \mathscr{H}^{Zeeman} + \mathscr{H}^{rf} + \mathscr{H}^{J} + \mathscr{H}^{dd} + \mathscr{H}^{cs} \tag{4}$$

The Zeeman (B_0) interaction of a spin I in the static reference frame is given by

$$\mathscr{H}_I^{Zeeman,static} = -\gamma_I B_0 I_z \tag{5}$$

where γ is the gyromagnetic ratio, B_0 is the external magnetic field, and I_z is the Cartesian z component of the spin angular momentum operator for spin I. As this interaction possesses a very high frequency and is continuously present during most common NMR experiments, it is expedient to work in a rotating reference frame. In this rotating frame, the Zeeman interaction transforms to

$$\mathscr{H}_I^{Zeeman} = (\omega_0 - \omega_{ref})I_z = \Omega_0 I_z \tag{6}$$

where ω_0 is the Larmor frequency of I, ω_{ref} is the rotation frequency of the frame, and Ω_0 is called the offset frequency. With this transformation, rf pulses lose their time dependency at the Larmor frequency. The rf Hamiltonian in the rotating frame is

$$\mathscr{H}_I^{rf} = \omega_1(I_x \cos\phi_p + I_y \sin\phi_p) \tag{7}$$

where ω_1 is the nutation frequency caused by the rf irradiation, I_x and I_y are the Cartesian x and y components of the spin angular momentum operator, and ϕ_p is the phase of the pulse.

The scalar (J) coupling Hamiltonian is isotropic and its secular approximations in the homo- and heteronuclear case, respectively, are

$$\mathscr{H}_{II}^{J} = 2\pi J_{II} \boldsymbol{I}_1 \boldsymbol{I}_2 \tag{8a}$$

$$\mathscr{H}_{IS}^{J} = 2\pi J_{IS} I_z S_z \tag{8b}$$

where J_{II} and J_{IS} are the homonuclear and heteronuclear scalar coupling constants, and $\boldsymbol{I}_1$ and $\boldsymbol{I}_2$ are the vector spin angular momentum operators.

On the other hand, both the dipolar coupling and the chemical shift interactions are anisotropic. The strength of the dipolar coupling depends on the interacting nuclear species, their distance, and their orientation. The dipolar coupling constant is

$$b_{IS} = -\frac{\mu_0 \gamma_I \gamma_S \hbar}{4\pi r_{IS}^3} \tag{9}$$

where μ_0 is the vacuum permeability, γ_I and γ_S are the gyromagnetic ratios of nuclei I and S, respectively, and r is the length of the internuclear vector. The secular approximations of the dipolar coupling Hamiltonians are then

$$\mathscr{H}_{II}^{dd} = \frac{1}{2} b_{IS} (3\cos^2\theta_{II} - 1)(3I_{1z}I_{2z} - \boldsymbol{I}_1 \cdot \boldsymbol{I}_2) \tag{10a}$$

$$\mathscr{H}_{IS}^{dd} = \frac{1}{2} b_{IS} (3\cos^2\theta_{IS} - 1)(2I_z S_z) \tag{10b}$$

for the homonuclear and the heteronuclear case, respectively, where θ_{II} or θ_{IS} is the angle between the internuclear vector and the static magnetic field.

The chemical shift is a shift in the Larmor frequency, which is represented as an offset frequency in the rotating frame:

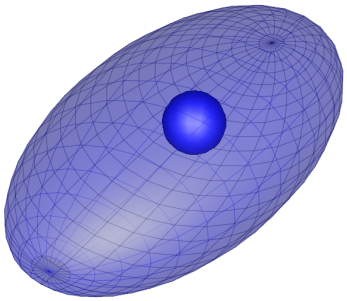

Figure 1: Triaxial ellipsoid as an illustration of a shielding tensor. The blue volume and its distribution depict the anisotropic nature of the chemical shielding as it would appear for the nucleus of the nitrogen atom of a peptide bond.

$$\mathscr{H}^{cs} = \Omega_{CS} I_z = \delta B_0 I_z \tag{11}$$

This offset frequency is governed by the chemical shielding and linearly dependent on B_0. The chemical shielding tensor may, in a general sense, be imagined as a triaxial ellipsoid whose extent describes the distribution of the chemical shielding in space (figure 1). Mathematically, it is commonly represented by a 3 x 3 matrix $\boldsymbol{\delta}$ which is diagonal in its principal axis systen (PAS):

$$\boldsymbol{\delta}^{PAS} = \begin{pmatrix} \delta_{xx}^{PAS} & 0 & 0 \\ 0 & \delta_{yy}^{PAS} & 0 \\ 0 & 0 & \delta_{zz}^{PAS} \end{pmatrix} \tag{12}$$

The principal components δ_{xx}^{PAS}, δ_{yy}^{PAS} and δ_{zz}^{PAS} may be used to calculate the isotropic chemical shift

$$\delta_{iso} = \frac{1}{3}(\delta_{xx}^{PAS} + \delta_{yy}^{PAS} + \delta_{zz}^{PAS}) \tag{13}$$

which is observed in solution samples due to molecular tumbling. In solids, the anisotropic property needs to be taken into account. By first ordering the principal

components according to their difference from δ_{iso}

$$|\delta_{zz}^{PAS} - \delta_{iso}| \geq |\delta_{xx}^{PAS} - \delta_{iso}| \geq |\delta_{yy}^{PAS} - \delta_{iso}| \tag{14}$$

they may be used to calculate the anisotropy δ_{aniso} and asymmetry (or biaxiality) η

$$\delta_{aniso} = \delta_{zz}^{PAS} - \delta_{iso} \tag{15a}$$

$$\eta = \frac{\delta_{yy}^{PAS} - \delta_{xx}^{PAS}}{\delta_{aniso}} \tag{15b}$$

that are used in the Haeberlen convention[26] to fully specify the chemical shift anisotropy (CSA) (other conventions exist, but will not be discussed here). This convention is also used by the simulation program SIMPSON[27–29] that was extensively used for this work and will be introduced later. To obtain the chemical shielding of a molecular site in the laboratory frame for solids, $\boldsymbol{\delta}_{PAS}$ needs to be transformed to $\boldsymbol{\delta}_{LAB}$ using the appropriate rotation matrix:

$$\boldsymbol{\delta}^{LAB} = \boldsymbol{R}_{LAB \to PAS} \cdot \boldsymbol{\delta}^{PAS} \cdot \boldsymbol{R}_{PAS \to LAB} \tag{16}$$

The extraordinary amount of control an experimenter has over the spin system via rf irradiation can be used to extract vast amounts of molecular information from a sample using NMR spectroscopy.

1.1 Theoretical background of MAS solid-state NMR

The molecular parameters responsible for the chemical shift and dipolar coupling are represented as anisotropic tensors. In solution, the anisotropic components are averaged

to zero to first order due to rapid molecular tumbling, leaving only the isotropic chemical shift. In contrast, the spectra of static powdered solids, or gelatinous biological solids, do generally not show sharp lines, but broad line shapes (powder or "Pake" patterns[30,31]) that result from the distribution of all possible orientations of structural features with respect to the external magnetic field.

However, despite these patterns containing information about molecular structure, they are generally undesired for biological solids, because the large number of resonances generated within the sample leads to excessive spectral crowding. For these samples, it is desirable to remove the anisotropies as far as possible and selectively reintroduce anisotropic interactions by applying specific rf pulse sequences.

Averaging the anisotropic effects can, for spins 1/2, be achieved by rotating the sample about an axis oriented at the so-called magic angle ($\theta_m \approx 54.7\,^\circ$) at a frequency larger than the size of the anisotropy[32–34]. In a pictorial way, spinning around this axis aligned with the spatial diagonal of a cube can be imagined as spinning around all three axes of Cartesian space at the same time.

For a more rigorous analysis of magic angle spinning (MAS), it is convenient to separate the spin and spatial components of the Hamiltonians by representing them in spherical tensor operators, which simplifies treatment of the time dependence caused by the rotation[35]. A general spin interaction Hamiltonian

$$\mathscr{H} = \sum_{k=0}^{2} \sum_{q=-k}^{+k} (-1)^q A_{kq}(t) T_{kq}(t') \tag{17}$$

where $A_{kq}(t)$ are the spatial components with time dependence due to sample rotation and $T_{kq}(t')$ are the spin components with time dependence due to the Zeeman interaction. Neglecting non-secular terms, and at $\omega_{MAS} \ll \omega_0$, this simplifies to

$$\mathscr{H} = A_{00}T_{00} + A_{10}(t)T_{10} + A_{20}(t)T_{20} \tag{18}$$

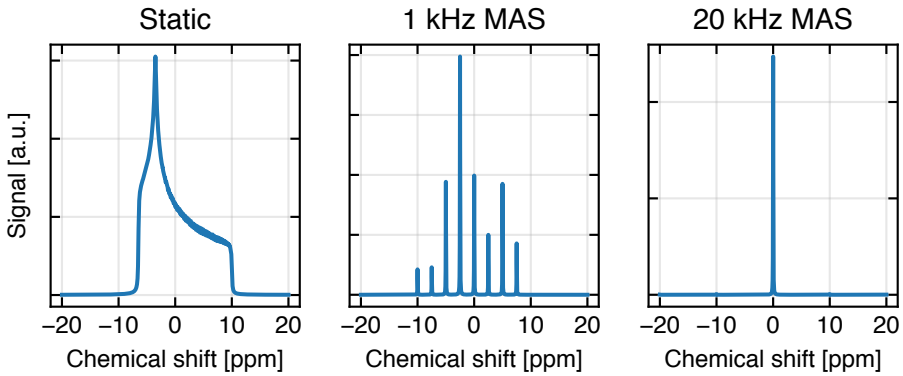

Figure 2: The effect of CSA in a static (left), slowly spinning (center) and fast spinning (right) sample. The Pake pattern of the static case transforms into spinning sidebands at a slow MAS frequency, and finally gets removed completely at a fast MAS frequency, leaving the isotropic chemical shift (in this case 0 ppm) behind.

The antisymmetric rank-1 spin component T_{10} may also be neglected, as it does not contribute to the spectrum to first order. The rank-0 component A_{00} is not affected by sample rotation and applies to the isotropic contributions. The effect of sample rotation on the remaining component $A_{20}(t)$ may be expressed as

$$A_{20}(t) = \sum_{q=-2}^{+2} A_{2q} \exp(-\mathrm{i}\omega_{MAS} t q) \exp(-\mathrm{i} q \vartheta_0) d^{(2)}_{q,0}(\theta_R) \tag{19}$$

where ϑ_0 is the initial rotor azimuth, θ_R is the angle of the spinning axis relative to B_0, and $d^{(2)}_{q,0}(\theta_R)$ are reduced Wigner rotation matrices. At a fast enough ω_{MAS}, this becomes averaged to

$$\overline{A_{20}}(t) = \frac{1}{2}(3\cos^2\theta_R - 1)A_{20} \tag{20}$$

Reintroducing the adequate spin components produces expressions for the homo- and heteronuclear dipolar coupling that are identical to equation 10, save for θ being replaced by the angle of the rotor axis θ_R. The chemical shift Hamiltonian emerges as

$$\mathscr{H}^{cs} = \delta_{iso} I_z + \frac{1}{2}(3\cos^2\theta_R - 1)(\delta_{zz}^{LAB} - \delta_{iso}) I_z \tag{21}$$

Thus, the dipolar coupling can be brought to zero, and the chemical shift to its isotropic value, by setting $3\cos^2\theta_R - 1 = 0$, which is the case for $\theta_R = \theta_m$.

With sufficiently fast spinning rates (the spinning rate needs to be at least of the same magnitude as the interaction in question), the anisotropic contributions can be fully eliminated. However, insufficient spin rates lead to spinning sidebands at integer multiples of the spin rate from the isotropic signal. An example of simulated static, slow, and fast spinning spectra of a nucleus with anisotropic shielding can be seen in figure 2. The hardware necessary to achieve these fast rotational speeds will be addressed in section 2.2.

1.2 Correlating nuclei: Couplings and coherence transfer techniques

NMR does not only allow the gathering of information about individual atoms through their chemical shifts, but also about their relationships with each other via internuclear couplings. In simple one-dimensional spectra, the couplings merely split or broaden the signals, but they may also be used to transfer coherent magnetization between nuclei, either through chemical bonds or directly through space. This allows the correlation of signals and consequently the elucidation of chemical structures.

Both the scalar (J) coupling and the dipolar coupling may be used for coherence transfers, but there are fundamental differences between the two:

Scalar coupling: The scalar coupling, which acts via the electrons of a chemical bond, is available in both liquid and solid samples. In the latter, it is also suitable for flexible regions of molecules. Its Hamiltonian was given in equation 8. However, it typically offers relatively low coupling constants, necessitating long delays for

transferring coherence between nuclei. Especially in solids, such long delays lead to a loss of experimental sensitivity due to relaxation.

Dipolar coupling: The dipolar coupling, with its Hamiltonian given in equation 10, is based on the local field produced by a given nucleus that directly influences another nucleus due to spatial proximity. In isotropic solutions, because of molecular tumbling, the dipolar coupling is averaged to zero in a first-order approximation. With the absence of molecular tumbling, the dipolar coupling is present in solids, and provides an efficient pathway for rapid coherence transfers. Its dependence on the third power of the internuclear distance and on molecular motion can be used to determine distances and molecular flexibility.

A common type of transfer via the scalar coupling is based on the Insensitive nuclei enhancement by polarization transfer (INEPT) experiment[36] (or variants thereof), which relies on $\pi/2$ and π pulses separated by delays $\tau/2 = 1/4J_{IS}$. In practice, slightly different delays may lead to better results due to relaxation. The pulse sequence for a basic INEPT experiment is illustrated in figure 3. The π pulses serve only to refocus the evolution of the chemical shift (i.e., set $\mathscr{H}^{cs}_{effective} = 0$) in a spin-echo block. Ignoring the π pulses, the initial density matrix $\rho(0)$ evolves under this pulse sequence as follows:

$$\begin{aligned}\rho(0) = I_z \xrightarrow[\mathscr{H}^{rf}]{(\pi/2)_x(I)} \rho(t_1) = -I_y \xrightarrow[\mathscr{H}^{J}]{\tau=\frac{1}{2J_{IS}}} \rho(t_2) = I_x S_z \\ \xrightarrow[\mathscr{H}^{rf}]{(\pi/2)_y(I)} \rho(t_3) = -I_z S_z \xrightarrow[\mathscr{H}^{rf}]{(\pi/2)_x(S)} \rho(t_4) = I_z S_y\end{aligned} \tag{22}$$

If, instead of the anti-phase $I_z S_y$ coherence, the detection of in-phase magnetization is desired (refocused INEPT[37]), an additional spin-echo period with the duration of τ can be inserted between the set of $\pi/2$ pulses and the detection. In the case of perfect pulses and neglecting relaxation, a full transfer of the initial coherence can be achieved by the INEPT scheme. However, in practice, imperfect pulses, relaxation, and the strong rf field inhomogeneity in MAS probes may hamper its efficiency.

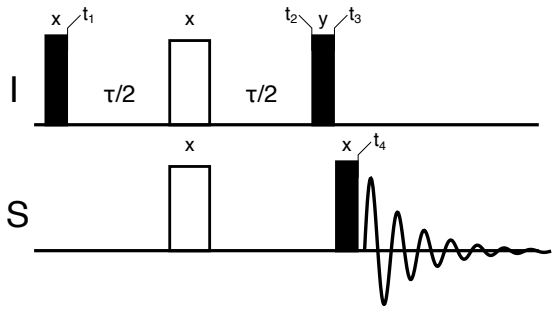

Figure 3: Pulse sequence of a basic INEPT experiment. The solid rectangles indicate $\pi/2$ pulses, the open rectangles indicate π pulses, with the phase given above the respective pulse. The π pulses refocus the evolution of chemical shifts within the transfer period.

Cross polarization (CP) transfers utilizing the dipolar coupling via rf irradiation at the Hartmann-Hahn (HH) condition may offer better transfer efficiencies due to the faster transfer made possible by the stronger coupling. In the HH condition for static samples[38,39]

$$\omega_{1,I} = \omega_{1,S} \tag{23}$$

the equal spin-lock frequencies ($\omega_{1,I}$ and $\omega_{1,S}$) on both channels generate an average Hamiltonian of the form[40]

$$\mathscr{H}_{IS}^{CP} = b_{IS}(3\cos^2\theta_{IS} - 1)(I_zS_z + I_yS_y) = \omega_{IS}(I_zS_z + I_yS_y) \tag{24}$$

for spin-lock fields along the x axis on both channels, where b_{IS} is the dipolar coupling constant introduced in equation 9. Under this Hamiltonian, I_x polarization is transferred to the S nucleus:

$$I_x \xrightarrow{(I_zS_z+I_yS_y)} I_x\frac{1}{2}(1+\cos\omega_{IS}t) + S_x\frac{1}{2}(1-\cos\omega_{IS}t) + (I_yS_z - I_zS_y)\sin\omega_{IS}t \tag{25}$$

Due to spin diffusion and the broad distribution of values for ω_{IS}, the behavior of real samples under this average Hamiltonian is normally not oscillatory. In the case of MAS, the condition is altered to

$$\omega_{1,I} = \omega_{1,S} \pm n\omega_{MAS} \tag{26}$$

with $n = 1, 2$[41].

The pulse sequences used for this kind of transfer are illustrated in figure 4. A continuous wave (CW) CP, the most basic form of this transfer, however, has a limit on its maximum efficiency of approximately 73 % set by the statistical distribution of θ_{IS} in a polycrystalline (or otherwise randomly oriented) sample[42]. In addition, it is susceptible to even slight mismatches of the HH condition, and, in the MAS case, cannot tolerate rf inhomogeneity due to the three-way matching condition from equation 26.

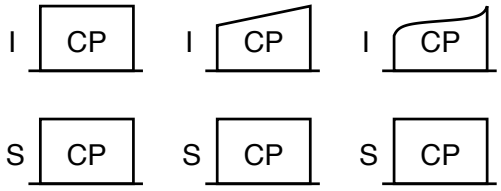

Figure 4: Pulse sequences of CP-type transfers. The left diagram shows the original CW CP, which possesses no adiabaticity and is not robust against mis-sets of the rf amplitudes and rf inhomogeneity. The center and right diagrams show ramped-amplitude and tangential shaped pulses on one channel, respectively, which are the schemes that are typically used in practice due to their adiabaticity and relative robustness.

To compensate for such effects, transfer schemes with variable amplitudes[43,44] and adiabatic-passage CP using tangential amplitude sweeps[45,46] were developed. These techniques are significantly more robust to rf inhomogeneity than their CW precursor, due to the sweep through a range of rf amplitudes and thus of HH conditions. In addition, they possess varying degrees of adiabaticity, which leads to the possibility of transfer efficiencies in excess of the theoretical limit of the CW variant.

1.3 Analysis of complex organic compounds - Multiple-resonance experiments

For the successful analysis of large molecules or specific molecular properties, a single spectral dimension can be insufficient due to spectral crowding. For example, discriminating between hundreds of ^1H resonances in a protein is impossible in a one-dimensional spectrum because of the large number of signals and the unfavorable ratio between linewidth and spectral dispersion. Similarly, experiments that correlate the signals of different nuclei are preferably recorded in several dimensions representing one kind of nucleus each.

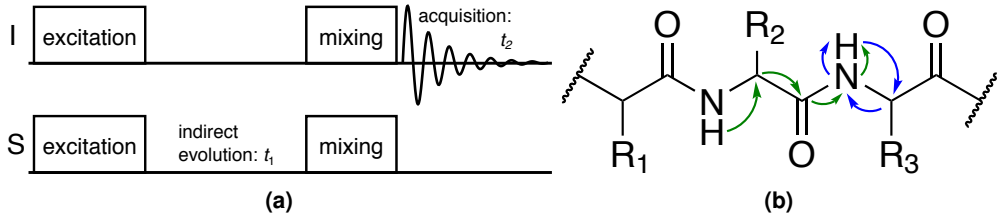

Figure 5: (a): An abstract sequence of a two-dimensional heteronuclear experiment. **(b)**: The transfer pathways in a set of hCaNH (blue) and hCacoNH (green) assignment experiments that are commonly used in solids[47].

To achieve these goals, multidimensional experiments were introduced[48]. Such experiments contain at least one indirect evolution period in addition to the acquisition period, and a mixing step between the two to correlate the two dimensions. An example is illustrated in figure 5a for a two-dimensional spectrum. While the acquisition is done in the same way as in a one-dimensional experiment, the indirect dimensions have to be acquired by repeating the pulse sequence multiple times while incrementing the indirect evolution periods. After the Fourier transformation of the directly acquired FIDs, the signals will be modulated by the indirect evolution period, and a second Fourier transformation along the indirect period will reveal the final spectrum in frequency units.

In commonly used multidimensional resonance assignment experiments in protein NMR, the chemical shift information of several defined nuclei within the backbone of a protein is correlated. By acquiring a combination of experiments such as hCaNH and hCacoNH (where capital letters denote chemical shift evolution on the respective nuclei), it is then possible to "walk" along the backbone of the protein and find which signal in the

spectrum corresponds to which atom in the main peptide chain. This is illustrated in figure 5b.

This information can then be used for analyzing further experiments that contain information on distances, dynamics or binding interfaces, gaining knowledge on a biological system with atomic resolution. However, due to the increasing number of coherence transfers involved in high-dimensional experiments, as well as the increased relaxation due to their long duration, the signal-to-noise ratio (S/N) may suffer significantly.

2 The hardware of NMR

2.1 The NMR experiment: Nuclear spin manipulation

A typical pulsed NMR experiment consists of a sequence of pulses and delays (in the most simple case a single excitation pulse), an acquisition period, and a recycle delay before the next scan that allows the relaxation of the spin system. The NMR spectrometer used for this task is composed of a number of individual devices:

1. A strong magnet (commonly superconducting cryomagnets) to greatly enhance the polarization of the spins, and additional equipment to stabilize ("lock") and homogenize ("shim") the field to ensure field uniformity throughout the experiment.

2. A probe that forms the interface between the sample and the electronics of the spectrometer, transmitting high power rf pulses into the sample and receiving the weak signals emitted by the sample.

3. An accurate frequency reference, usually an oven controlled crystal oscillator (OCXO).

4. Signal generators and power amplifiers to create carefully controlled rf pulses that allow the manipulation of the spins.

5. An extremely low-noise preamplifier, receiver, and analog-to-digital converter (ADC) for the detection and digitization of the signals emitted by the sample.

6. Accessories, e.g., a sample temperature controller, or a pneumatic control unit for sample spinning.

A schematic diagram of an NMR spectrometer is illustrated in figure 6. A prime requirement for NMR experiments is a highly accurate and stable frequency reference, commonly an OCXO. This reference signal, or derivatives thereof, are fed to the spectrometer control, the waveform generator and the receiver. The waveform generator is responsible for synthesizing the rf pulses, with the proper relative amplitude and phase at the proper time in the pulse sequence, at a low power. This signal is sent into a high power transmitter through a blanking switch that prevents noise from being amplified during delays. The amplified pulses are then fed, through the transmit/receive switch, into the NMR probe containing the sample.

To detect the very low power NMR signal (induced by the magnetic moment of the sample to the NMR coil) after it exits the probe, it is first amplified to a voltage level that is less susceptible to external disturbances by a preamplifier located close to the probe. After that, it is further amplified and digitized within the receiver, and the digitized complex signal is passed to the spectrometer control for storage and processing.

The NMR probe is perhaps the most specialized piece of the NMR spectrometer apart from the magnet: It needs to withstand rf pulses with powers on the order of 100 W and to transmit these efficiently into the sample, while at the same time (when decoupling) receiving signals emanating from the sample at a different frequency, but at a power on the order of fW[49]. To achieve this, the multi-frequency rf circuit inside the probe needs to be carefully designed, and adjustable elements need to be included for "tuning and matching". This process describes the adjustment of the impedance and the frequency response of the circuit for varying samples, which may, e.g., contain different concentrations of electrolytes and consequently have different electromagnetic characteristics.

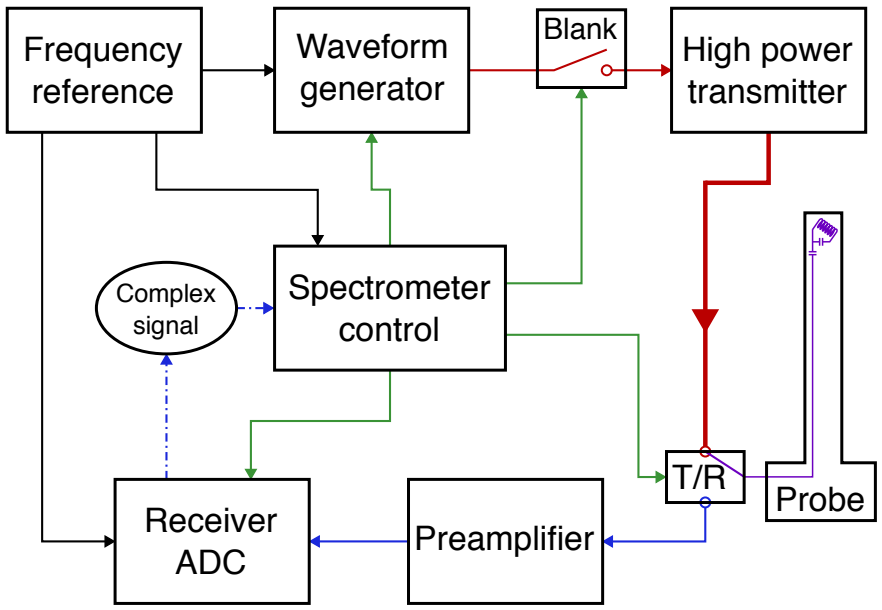

Figure 6: Schematics of the real-time signal pathway in an NMR spectrometer. Black: Frequency reference signal, green: Control signals, red: rf pulse signals, blue: NMR signal emitted from the sample. The probe circuit is involved in both the pulse and the sample signal pathways and is thus drawn in purple. Dot-dashed lines indicate digital signals. Communication whose correct timing is not critical to the pulse sequence (e.g., diagnostic signals from the transmitter) is not shown.

2.2 Mechanical implementation of MAS - Rotation and sample packing

For MAS to be effective, the spin rate needs to be significantly faster than the magnitude of the interaction to be averaged. This means in practice that spin rates on the order of kHz are necessary to remove CSA effects, and in excess of 100 kHz are needed to remove homonuclear dipolar couplings between high-γ nuclei such as ^1H or ^{19}F. The highest spin rate that has been reached at the time of writing is 170 kHz in a rotor of 0.5 mm diameter[50], while the commercially available 0.7 mm Bruker system can achieve a spin rate of 111 kHz.

High spin rates in a mechanical system are typically achieved by equipping a rotor, made from ZrO_2 ceramic or sapphire, with a cap that possesses integral turbine fins. A cutaway illustration of a 1.3 mm rotor and a comparison of several rotor sizes are shown in figure 7. The rotor is then inserted into a stator that contains jets for an air bearing

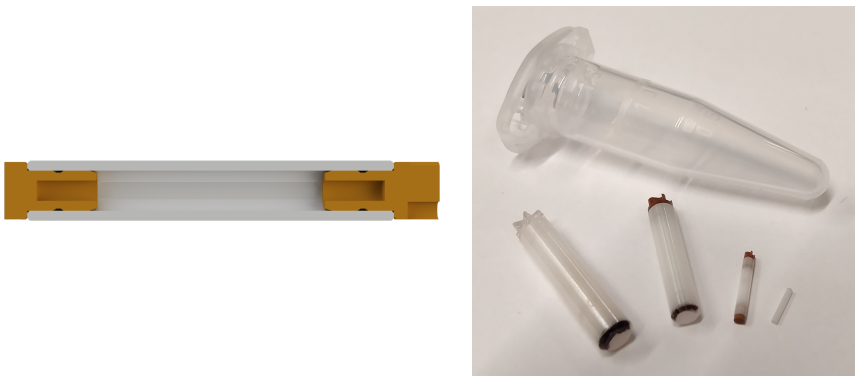

Figure 7: Left: A cutaway illustration of a 1.3 mm Bruker rotor. The space between the two brown caps is in principle available for the sample, but for substances that must not dry out, additional sealing plugs are needed besides the rotor caps. Right: A comparison of different rotor sizes, from left to right: 4.0 mm, 3.2 mm, 1.3 mm, and 0.7 mm without its caps, with a standard 1.5 mL Eppendorf tube for scale in the background.

system at the ends of the rotor, and for driving the rotor using the aforementioned turbine[51]. Around the center of the rotor, the NMR coil (commonly a solenoid) is placed with only a small gap between the conductor and the outer rotor wall to increase the efficiency of the coil (figure 8).

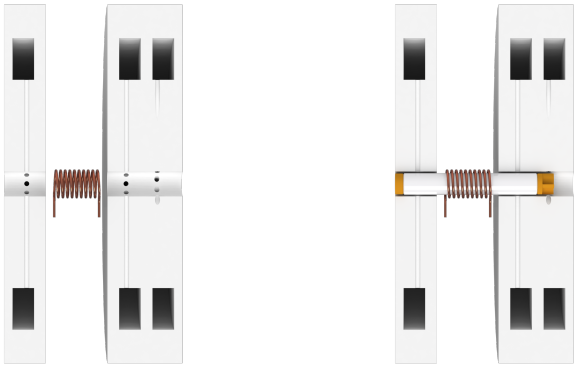

Figure 8: Illustration of the rotor-stator system used in MAS NMR probes. Left: Stator and coil without an inserted rotor. The parts of the stator immediately next to the coil form the air bearing, while the rightmost part contains the drive system that acts on the turbine fins of the rotor top cap. Right: Stator with inserted rotor.

The limit for the achievable spin rate in this arrangement is set either by the mechanical strength of the rotor material, or by the speed of sound in the drive and bearing gas. Because the fluid dynamics in the drive and bearing system change nonlinearly at

transsonic velocities, the circumferential speed of the rotor should be subsonic at all times. To achieve that, smaller rotors are beneficial, but because of the sample volume restriction at smaller diameters, the rotor walls have to shrink as well. This leads to the material strength becoming a greater factor. Of course, any damage to the rotor that forms a stress riser, such as a scratch, can have catastrophic consequences as well.

Filling a sample into the rotor can be challenging. Larger rotors, such as the 7 mm or 4 mm rotors still commonly used for materials research, can often be packed with a suitably shaped funnel and a tamper, especially when the sample is a dry powder. On the other hand, packing a biological sample into a 0.5 mm or 0.7 mm rotor requires specialized filling tools and an ultracentrifuge to succeed in packing the necessary amount of sample into the rotor. The design of a filling tool for the Bruker 0.7 mm rotor system will be outlined in section 5.2.

Another issue of the employed rotor-stator systems is frictional heating of the rotor due to the bearing and drive gas flows. Within the range of rotor sizes available from Bruker, the 1.3 mm rotors are most affected by frictional sample heating, presenting the danger of denaturation and dehydration for biological samples. While heat denaturation can be prevented by high variable temperature (VT) cooling gas flows, dehydration has to be overcome by inserting sealing plugs between the sample and the rotor caps. These plugs of course take up potentially valuable sample space, so they should be kept as small as possible. An improved plug design will be presented in section 5.1.

3 Simulation and optimization

3.1 Simulation in SIMPSON

SIMPSON, the SIMulation Program for SOlid-state Nmr spectroscopy, is a software package that allows the simulation of spin dynamics in solid-state NMR with relative ease. It was initially released in 2000[27], and was significantly extended with optimal control (OC) optimization capabilities in 2009[28]. Further enhancements were published in 2014, which include parallelization, improved computational efficiency and the option to include axial rf inhomogeneity into the calculations[29].

The latest step in the evolution of SIMPSON (programmed by Zdeněk Tošner) has not yet been published, but extensively used within the work for this thesis. It allows the consideration of pulse transients and, mainly, of radial, rotationally modulated rf inhomogeneity in the calculations. The latter concept was outlined in 2017[52], and OC optimizations run utilizing this concept led to shaped pulses that possess higher transfer efficiencies than traditional ramp-CP transfers[53].

The numerical simulation of NMR experiments in SIMPSON relies on the evaluation of the Liouville-von Neumann equation that was already introduced earlier:

$$\frac{\mathrm{d}}{\mathrm{d}t}\rho(t) = -\mathrm{i}[\mathscr{H}(t), \rho(t)] \tag{27}$$

where $\rho(t)$ is the density matrix as a representation of the state of the spin system, and $\mathscr{H}(t)$ is the time-dependent Hamiltonian that contains all relevant spin interactions and manipulations. Neglecting relaxation effects, the solution to equation 27 can be

written as

$$\rho(t) = U(t,0)\rho(0)U^{\dagger}(t,0) \tag{28}$$

where $\rho(0)$ is the initial density operator, and $U(t,0)$ is the unitary propagator that describes the spin dynamics in the time spanning between 0 and t. To obtain $U(t,0)$ from the Hamiltonian, the relationship

$$U(t,0) = \hat{T}\exp\left(-\mathrm{i}\int_0^t \mathscr{H}(t')\,\mathrm{d}t'\right) \tag{29}$$

with $\hat{T}$ being the Dyson time-ordering operator (ensuring the correct order of noncommuting interactions) can be used. For numerical simulations, this is commonly calculated as a time-ordered product, in which the Hamiltonian is considered time-independent for each of n time intervals:

$$U(t,0) = \prod_{j=0}^{n-1} \exp(-\mathrm{i}\mathscr{H}(j\Delta t)\Delta t) \tag{30}$$

By following this principle, equation 28 can be expressed with piecewise constant propagators:

$$\rho(t) = U(t_n,t_{n-1})\ldots U(t_2,t_1)U(t_1,0)\rho(0)U^{\dagger}(0,t_1)U^{\dagger}(t_1,t_2)\ldots U^{\dagger}(t_{n-1},t_n) \tag{31}$$

The total Hamiltonian (in the rotating frame) that defines the evolution of the spin system contains contributions from different interactions:

$$\mathscr{H}^{total} = \mathscr{H}^{rf} + \mathscr{H}^{cs} + \mathscr{H}^{J} + \mathscr{H}^{dd} \tag{32a}$$

$$\mathscr{H}^{total} = \mathscr{H}^{rf} + \mathscr{H}^{int} \tag{32b}$$

where $\mathscr{H}^{rf}$ contains the external influence from the applied rf fields, $\mathscr{H}^{cs}$ contains the contributions from chemical shielding, $\mathscr{H}^{J}$ contains the contributions from scalar couplings, and $\mathscr{H}^{dd}$ contains the contributions from dipolar couplings. For nuclei with $I > 1/2$, contributions from quadrupolar interactions would need to be included as well.

The internal contributions $\mathscr{H}^{cs}$, $\mathscr{H}^{J}$ and $\mathscr{H}^{dd}$ may all possess anisotropic (rank 2 tensor) components, which need to be rotated from the principal axis frame in which they are specified, through the crystal-fixed and rotor-fixed frames, into the laboratory frame. These rotations about the Euler angles contained in the spin system definition are performed in SIMPSON using rank-2 Wigner rotation matrices and reduced Wigner rotation matrices[35].

To account for different crystallite orientations in a powdered sample, the calculations can be repeated for a number of different crystallite-to-rotor orientations. For the case of MAS, all anisotropic interactions become time-dependent because of the sample rotation, necessitating additional transformations of the reference frame.

3.2 Optimal control theory

OC theory is a mathematical method of optimization largely based on work by Lev Pontryagin[54] and Richard Bellman[55,56]. OC is suitable for optimizations that involve large numbers of free variables (or "controls") such as the individual amplitudes and phases of the increments of shaped rf pulses (see figure 9 for an illustration). This has been demonstrated in a variety of NMR imaging[57–63], as well as solution-state[64–72] and solid-state[53,73–78] NMR spectroscopic applications. Hence, OC functionality has been integrated into SIMPSON in 2009[28], and this integration has been improved

in 2014[29]. Other NMR simulation frameworks, such as Spinach[79], also possess OC features, further underlining its suitability for NMR applications.

An optimization according to the Gradient Ascent Pulse Engineering (GRAPE) algorithm commonly used in NMR applications[66] would be conducted as follows: Consider, for example, a state-to-state transfer between two spin states that shall be optimized. First, the initial and desired final states $\rho(0)$ and C, respectively, the internal Hamiltonian of the spin system $\mathscr{H}^{int}$, and the available controls, which will be part of the rf Hamiltonian $\mathscr{H}^{rf}$, need to be specified. The available controls also have to be initialized with some starting values, commonly random numbers within a reasonable range. For spins with $I = 1/2$, $\mathscr{H}^{int}$ may be expressed as

$$\mathscr{H}^{int}(t) = \mathscr{H}^{cs}(t) + \mathscr{H}^{J}(t) + \mathscr{H}^{dd}(t) \tag{33}$$

and $\mathscr{H}^{rf}$ as

$$\mathscr{H}^{rf}(t) = \sum_i \omega_1^{I_{ix}}(t) I_{ix} + \omega_1^{I_{iy}}(t) I_{iy} \tag{34}$$

with x- and y-phased contributions from all available rf channels. For the numerical calculations, continuous functions are approximated by piecewise constant functions, which lead to the formulation for the calculation of the final state $\rho(T)$ introduced in equation 31 via the calculation of piecewise propagators. For an optimal transfer, the overlap between the target state and the calculated final state needs to be maximized, so the final target (or cost) function of the optimization is defined as the standard inner product:

$$\Phi_{fin} = \langle C|\rho(T)\rangle = \mathrm{Tr}\Big\{C^\dagger U \rho(0) U^\dagger\Big\} \tag{35}$$

The overall target function, which is used to evaluate the performance of the current solution, may contain other terms in addition to Φ_{fin}, such as rf energy costs or

penalties on the presence of undesired components in the final state.

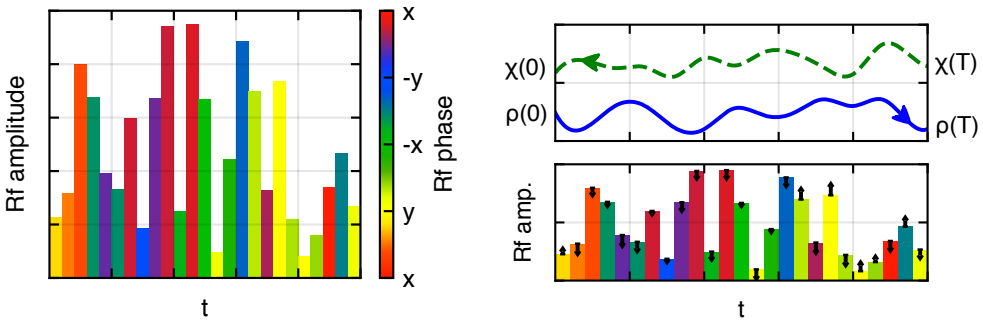

Figure 9: Left: Example of a pulse composed of increments with arbitrary amplitudes and phases. Each of the increments can be viewed as a complex variable subject to OC optimization. Right top: The forward and backward trajectories, calculated starting from the initial and desired states, respectively, will generally not overlay. Right bottom: The gradient directs changes to the pulse increments.

To guide the changes applied to the controls and thus the improvement of the overall target function, a gradient is calculated from the trajectories of the forward-propagated initial operator $\rho(0)$ and the back-propagated desired operator C (reusing the propagators from the forward propagation)

$$\chi(t_j) = U^\dagger(t_{j+1}, t_j) \dots U^\dagger(t_N, t_{N-1}) C U(t_N, t_{N-1}) \dots U(t_{j+1}, t_j). \tag{36}$$

The gradient for each of the rf controls (or element pulses) can then be calculated as

$$\frac{\partial \Phi_{fin}}{\partial \omega_1^{I_{iq}}(t_j)} = \langle \chi(t_j) | -\mathrm{i}\Delta t_j [I_{iq}, \rho(t_j)] \rangle \tag{37}$$

where $q = x, y$. The overall gradient, in analogy to the overall target function, can also include additional contributions such as penalties on excessive energy deposition or unwanted operators in the final state. The element pulses are iteratively updated according to

$$\omega_1^{I_{iq}}(t_j) \to \omega_1^{I_{iq}}(t_j) + \epsilon \, \mathrm{Tr}\Big\{ \chi^\dagger(t_j) \mathrm{i}\Delta t_j [I_{iq}, \rho(t_j)] \Big\} \tag{38}$$

where ϵ is a small real number representing the length of the step along the gradient. By iterating through this approach until a certain condition (e.g., the improvement per iteration falling below a certain threshold) is met, the initial set of controls can be improved to approximate a local minimum on the landscape of all possible controls.

3.3 Optimal control pulses for real MAS probes

While pulses designed by the use of OC can outperform analytical pulse shapes under the best realistic conditions, the approach promises even greater benefits when experimental imperfections such as rf amplitude mis-set, pulse transients or rf field inhomogeneity are present. Especially the latter is an issue in MAS probes due to the common choice of solenoids as rf resonators. While these allow high rf amplitudes and good detection sensitivity through the high achievable filling factor, their field homogeneity is lacking. Though improvements such as variable pitch coils[80], or ribbon coils with a varying width of the conductor[81], have been used and, in case of the former, even employed in commercially available probes[82], they are not commonplace.

When calculating the rf field within a solenoid[83], it becomes apparent that the field is not just dependent on the axial position within the coil, but that there are also radial deviations[52]. When the solenoid is mounted at the magic angle with respect to the external magnetic field (which defines the z axis), this means that with sample rotation the rf field becomes rotationally modulated (see figure 10).

Consequentially, rf field inhomogeneity is a problem in most MAS probes, and it reduces the efficiency of various experimental building blocks, ranging from hard pulses and techniques that rely on spin-lock fields such as CP (see figure 11) to experiments like Rotational Echo Double Resonance (REDOR) recoupling or frequency-switched Lee-Goldburg (FSLG) decoupling[84]. Due to the distribution of rf fields within the sample volume, the optimal conditions for an experiment can only be met in a small portion of the whole sample.

While the effect of the rotational modulations remains small for techniques that rely on periods of relatively constant rf irradiation that are on the order of a rotor period

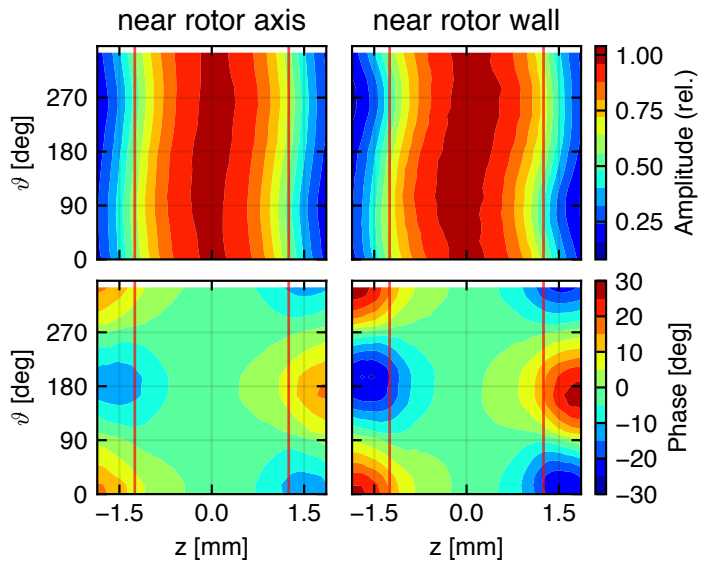

Figure 10: Rf field distribution within a 1.3 mm probe. While the field near the rotor axis is hardly dependent on the azimuth angle ϑ, near the rotor wall and especially towards the ends of the coil, the dependence becomes severe, leading to rotational modulations.

or longer, they have the potential to be especially problematic for the highly dynamic pulse shapes that tend to emerge in OC optimizations. This leads to the necessity of accounting for changes in rf irradiation during the course of a rotor period, a feature which is implemented in the aforementioned unpublished version of SIMPSON[53].

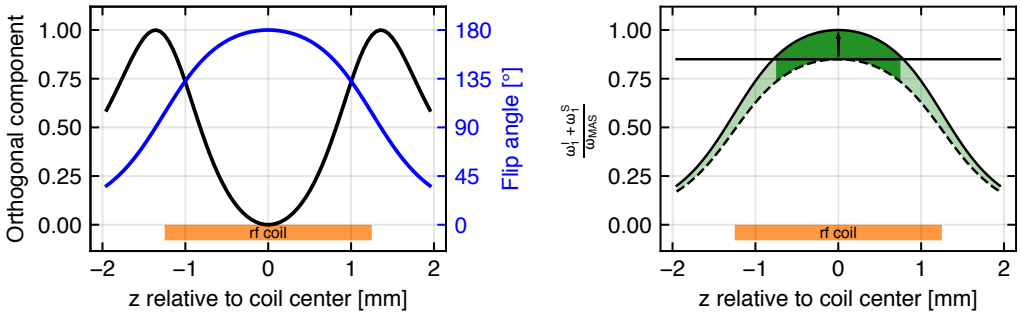

Figure 11: Left: The effect of rf inhomogeneity on the local flip angle of a hard 180 degree pulse calibrated to be accurate in the central region of the coil. Right: A thought experiment on the effect of a ramped-amplitude CP. Using a 70-100 % ramp on one channel and given the HH condition under MAS stated in equation 26, the condition can only be matched within the dark green region.

3.4 The usage of SIMPSON

SIMPSON is operated using input scripts that are written in the programming language Tool command language (Tcl) and organized in two array variables "spinsys" and "par", and at least two functions (or procedures in Tcl terminology), "pulseq" and "main". For OC optimizations, the additional functions "gradient" and "target_function" are needed. In the following, a cursory introduction shall be given, for more complete documentation please consult the publications on SIMPSON[27–29].

In the "spinsys" variable, the parameters of the spin system that is used in the simulation are provided:

```
spinsys {
    # This line gives the spectrometer channels, which will be
      referenced in the same order:
    channels 1H 15N
    # This line gives the actual nuclei, their order is equivalent to
      the numbering used later:
    nuclei 1H 15N 1H 1H
    # Next are the chemical shifts, which include the anisotropic
      components and their angles:
    shift 1 0 7.7p 0.65 74.3 -94.6 174.9
    shift 2 0 99p 0.19 90.2 73.6 -111.5
    shift 3 0 7.7p 0.65 -148.0 -146.7 -64.8
    shift 4 0 7.7p 0.65 48.0 2.6 155.0
```

```
    # Dipolar couplings are of paramount importance in solid-state NMR
        and are given next:
    dipole 1 2 10400 0 105.7 86.1
    dipole 1 3 -6773.2 0 85.6 -153.7
    dipole 1 4 -9687.3 0 142.8 -115.1
    dipole 2 3 366.9 0 98.3 41.2
    dipole 2 4 1146.3 0 163.5 -148.4
    dipole 3 4 -1697.0 0 113.4 -140.4
    # The last parameter in this file is the J coupling:
    jcoupling 1 2 -92 0 0 0 0 0
    # Any unspecified parameters will be assumed to be 0.
}
```

The "par" variable contains parameters that would be defined by the spectrometer hardware, such as Larmor frequency, and in the software, such as spectral width. It also contains parameters that are relevant to the computation, e.g., the number of CPU cores to be used by the simulation:

```
par {
    # Technical simulation parameters:
    method          direct dsyev
    verbose         1101
    num_cores       4
    ...

    # Spectrometer parameters:
    proton_frequency    800e6
    spin_rate           60000
    sw                  5e5
    np                  2048

    # Initial state and detection parameters:
    start_operator      I1z
    detect_operator     I2x

    # Averaging parameters or files for the simulation (e.g. powder
        averaging):
    crystal_file        rep3_112.cry
    gamma_angles        1
    rfmap               1p3mm_coil.dat
    averaging_file      chemical_shifts.ave
```

```
    # User-defined values
    variable contact_time           800
    variable coupling_constant      92.0
}
```

In the "pulseq" procedure, the pulse sequence is defined. Within the procedure, standard Tcl syntax can be used alongside SIMPSON-specific instructions. As an example, a $^1H - ^{15}N$ INEPT experiment shall be simulated:

```
proc pulseq {} {
    # Making the "par" array available within this procedure
    global par

    # Calculations using standard Tcl syntax
    set tau_half [expr 1.0/(4*$par(coupling_constant))]

    # Pulse sequence using SIMPSON syntax
    reset
    pulse 2.5 100000 x 0 x
    delay $tau_half
    pulse 5.0 100000 x 100000 x
    delay $tau_half
    pulse 2.5 100000 y 100000 x
    acq $par(np)
}
```

The "main" procedure is always run when an input file is passed to SIMPSON, and it defines the sequence of the whole simulation. In it, the whole course of the simulation is defined. This may include the calculation of parameters prior to the NMR simulation, or data processing, fitting and formatting after the simulation. In the example presented here, the data from the simulation shall be apodized with an exponential function, Fourier transformed and saved to disc:

```
proc main {} {
    global par

    # This line runs the NMR simulation:
    set f [fsimpson]

    # Exponential line broadening and Fourier transform
    faddlb $f 20 0
```

```
    fft $f

    # Save the data and free the memory
    fsave $f $par(name).spe
    funload $f
}
```

To use the OC capability, the additional procedures "gradient" and "target_function" and a slightly modified "pulseq" procedure are necessary.

The "gradient" procedure defines how the gradient for the OC optimization is calculated. For instance, component gradients can be combined to favor one outcome while penalizing another. It is also possible to include an energy penalty component. In this example, two rf shapes are optimized and an energy penalty is applied:

```
proc gradient {} {
    # rfsh1 and rfsh2 are variables containing rf (pulse) shapes
    global par rfsh1 rfsh2

    # For every time slice in every optimized pulse, there needs to be a
        point in the gradient
    set par(np) [expr 2*$par(plen)]

    # Calculation of the "actual" gradient
    set g [fsimpson]

    # Pulse energy penalty with weighting factor $par(lam)
    oc_grad_add_energy_penalty $g $rfsh1 -$par(lam) $rfsh2 -$par(lam)

    # The returned variable contains the gradient that is used by the
       optimization
    return $g
}
```

The calculation of the target function is defined in the "target_function" procedure. In contrast to the gradient, the target function is a single number, which can be considered a figure of merit of the current iteration:

```
proc target_function {} {
    global par rfsh1 rfsh2
```

```
    # The target function should only return a single number
    set par(np) 1

    # Calculate the first point of the FID, which contains the signal
        amplitude on the detect operator, and extract its real part
    set f [fsimpson]
    set fr [findex $f 1 -re]

    # Calculate the energies contained in the optimized shapes rfsh1 and
         rfsh2
    set en1 [shape_energy $rfsh1 $par(plen)]
    set en2 [shape_energy $rfsh2 $par(plen)]

    # Calculate the full target function and return it
    set Result [expr $fr - $par(lam) * ($en1 + $en2)]
    return $Res
}
```

This relative ease of use, combined with the ability to use a common and fully functional programming language in the input script, makes SIMPSON an excellent tool for the simulation of NMR experiments. In addition to simulating spectra that can be measured on an actual spectrometer, it is also possible to extract the exact state of a spin system at arbitrary points during an experiment. Furthermore, with its OC capabilities, it can be used to improve NMR experiments with numerically optimized pulses.

4 Results I: Optimal Control-derived shaped pulses for MAS solid-state NMR

4.1 H-N transfers in perdeuterated and reprotonated peptides at fast MAS

In many solid-state NMR investigations on proteins at fast MAS, the sample under investigation is perdeuterated and reprotonated at the exchangeable sites (such as the amide protons). These backexchanged protons often serve as the source of magnetization for experiments involving heteronuclei. One commonly used building block in these solid-state NMR experiments is the $H-N$ CP, which is used to transfer magnetization from the amide proton to the amide nitrogen via the dipolar coupling (figure 12). This transfer can also be performed in the reverse direction to utilize the higher sensitivity of ^1H nuclei during detection.

However, in the fast-spinning regime, these transfers are hampered by rf field inhomogeneity and a narrowing of the resonance condition. OC derived pulse sequences, in principle, are able to overcome these limitations to enhance transfer efficiencies compared to conventional methods[53]. In the following sections, the development of these pulses with the aim of replacing the more standard ramped-amplitude CP shall be outlined.

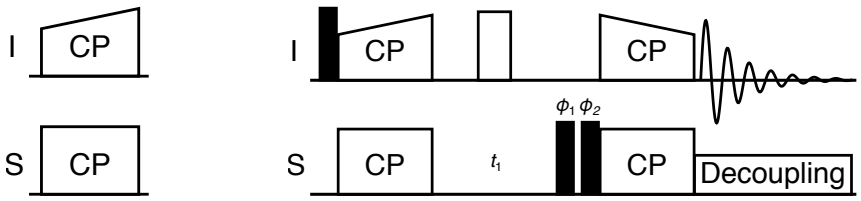

Figure 12: Left: Classical ramped-amplitude CP. The ramped amplitude introduces a degree of adiabaticity in addition to compensating the rf field inhomogeneity. Right: Application in an hNH 2D pulse sequence. The CP transfer blocks shall be replaced by OC derived transfers.

4.1.1 Simple optimizations

The first approach was the optimization of a simple state-to-state transfer of H_x magnetization to N_x magnetization (or vice versa) in a ^1H-^{15}N two-spin system, under consideration of a relevant spread of chemical shifts and rf field conditions ("robustness constraints"). These optimizations were started from a random set of variables ("seed") with a limited rf amplitude and full phase range.

The first step in the OC pulse generation process generally is determining the maximum quality factor achievable for a certain pulse duration, forming what is commonly called a "top curve" (figure 13). For these top curves, a fairly large number of optimizations (10-100 per investigated duration) without including robustness constraints is performed. Another variable to consider at this stage is the digitization step of the shaped pulse, or the duration of the single increments within the total shape. Running these calculations for the H_x-N_x, H_z-N_x and N_x-H_x state-to-state transfers makes it evident that a pulse duration of 600 µs to 1000 µs is a reasonable choice for these transfers and not much different for digitization intervals between 1 µs and 4 µs. Consequently, pulses with all of these time increments and durations were optimized for robustness towards rf inhomogeneity and a distribution of chemical shifts (or offsets) similar to the one expected in a protein sample. The constraints are implemented by averaging the gradient and target function over calculations at a range of rf and chemical shift conditions.

The resulting pulses at first glance may look much like random noise (a typical pulse is shown in figure 14a). While closer inspection reveals a certain periodicity that roughly coincides with the MAS frequency, no resemblance to known analytical transfer schemes

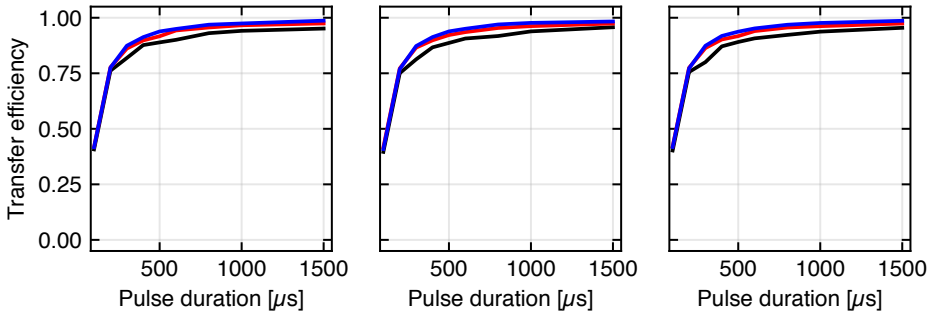

Figure 13: From left to right: Top curves for simple H_x-N_x, H_z-N_x, and N_x-H_x state-to-state transfer optimizations, with pulse increments of 1 µs (black), 2 µs (red), and 4 µs (blue).

is apparent. But despite their random appearance, *in silico* and under the conditions for which they were optimized, these pulses achieve a magnetization transfer that is more efficient than the transfer by the reference technique by approx. 60 %.

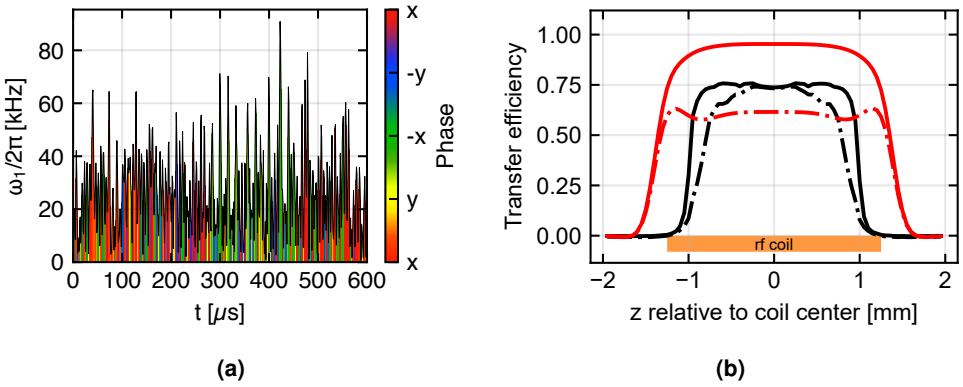

Figure 14: (a): An example for an optimized pulse. Time increment of the pulse: 1 µs. The increment phase is depicted by a circular color map[85]. **(b)**: Simulated efficiency profiles along the axial coordinate of the rotor of a 40-100 % ramp-CP (black) and a pulse from the simple optimization runs (red). The performance of both transfers was calculated in a two-spin system (solid lines) and in a spin system containing remote protons (dot-dashed lines). The ramp-CP transfers 50.5 % of the magnetization detectable by the coil in a 2-spin system and 42.5 % with remote protons, whereas the OC shape pair transfers 79.1 % in a 2-spin system and 52.5 % with remote protons.

However, the simulated performance of these pulses cannot be replicated in experiments. When experimentally compared to the most efficient ramp-CP transfers (close to the conditions used by Barbet-Massin et al.[47]), the obtained S/N is very similar between the classical experiment and the numerically optimized pulse set, with even a slight loss when using the OC shapes. This behavior is exaggerated when multiple back-and-forth

transfers are concatenated (see figure 15 and table 1). For a transfer that performs excellent in one part of the sample and not at all in other parts, one would only expect additional relaxation losses with a growing number of back-and-forth transfers. All the signal to be lost by this volume-selective transfer would be lost already in the first step. On the other hand, if a transfer is mediocre throughout the whole sample, the signal would be lost progressively with an increasing number of transfer blocks. Here, the more rapid loss of S/N for the OC transfer points to a lower maximum transfer efficiency for the OC transfer than for the ramp-CP.

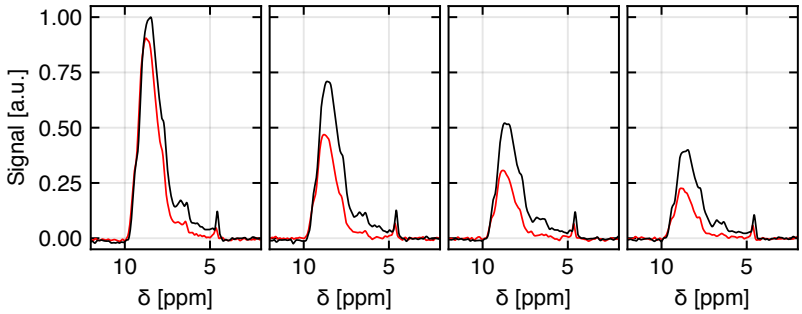

Figure 15: From left to right: Spectra of ^{2}H,^{13}C,^{15}N-labelled islet amyloid polypeptide (IAPP) (100 % protonated at the exchangeable sites) with 1, 2, 3 and 4 concatenated $H \rightarrow N \rightarrow H$ transfer blocks. Black spectra recorded with ramp-CP transfers, red spectra with a first-generation $H \rightarrow N$ OC shape pair that was time-inverted for the $N \rightarrow H$ transfer.

Transfers	2	4	6	8
Ramp-CP	1	0.71	0.73	0.77
OC transfer	0.9 x ramp	0.52	0.65	0.74

Table 1: Amount of signal left after a given number of transfer blocks (with 2 transfers each), relative to the preceding number of transfers.

This conflicts with the simulations in a two-spin system, which indicate that the OC transfer should have a much higher maximum transfer efficiency than the ramp-CP that is furthermore achieved in a larger portion of the sample. There may be a multitude of explanations for this behavior, of which the most likely was thought to be the presence of remote protons. This suspicion is supported by the results of simulations in larger spin systems either including one or two neighboring protons of the amide group in a protein backbone (figure 14b). It is clearly evident that the effect of additional protons around the amide group of interest is much larger for the OC transfer than for the ramp-CP. This was the case for all investigated pulse durations and digitization

intervals, and also for the $N \rightarrow H$ transfers, for which no data is shown. A slight increase in performance was observed for pulses that start from H_z magnetization instead of H_x (presumably through higher excitation efficiency throughout the whole sample volume), but these shapes did not match the high expectations either. It is also likely not an issue of pulses that are excessively specialized for the optimization problem, as several tested intermediate shapes (with already good transfer efficiency, but not yet meeting the technical convergence criterion) did not show more favorable behavior.

In theory, this problem might be solved by simply optimizing shapes in a more realistic spin system with multiple protons around the spin pair of interest, possibly necessitating an averaging scheme over different orientations and CSA of the remote spins. In practice, however, this is hardly doable because the computational effort necessary for simulating NMR experiments scales exponentially with the number of spins, and an additional need for averaging further increases the needed amount of computation time. Several approaches to counteract the lack of robustness towards large dipolar couplings not considered in the simulations will be discussed in the upcoming sections.

A further, minor reason for lower than expected performance of the OC transfers is the value that was initially chosen for the magnitude of the dipolar coupling between the nuclei. This value was based solely on the distance between the nuclei and did not take the flexibility of proteins into account. After reducing the magnitude from 12.8 kHz to 10.4 kHz, which appears to be a more realistic value for the rigid portions of proteins[86], OC transfers could match, but still not exceed the performance of ramp-CP transfers.

4.1.2 Creating robustness against remote protons using larger spin systems

To address the detrimental effect of remote protons on the performance of OC-optimized transfers directly, two methods to optimize shapes that are less affected by these remote protons were devised. The first method used a four-spin system that contained the two protons from the neighboring amide groups in a protein backbone. This was simple to implement, but two drawbacks are immediately obvious: The computational effort is greatly increased by doubling the spin system size, and the usage of two additional

spins with a defined spatial relationship to the amide group of interest may promote the generation of solutions specialized for this exact situation.

The second approach used a three-spin system with only one remote proton, whose dipolar coupling constant and orientation relative to the primary proton however samples a number of different values to prevent the creation of overspecialized solutions (see figure 16a). In this scenario, the coupling of the remote proton to the ^{15}N nucleus was not modified by the sampling scheme. At its relatively low magnitude of approx. 1 kHz it was deemed a less influential factor on the timescale of the transfers.

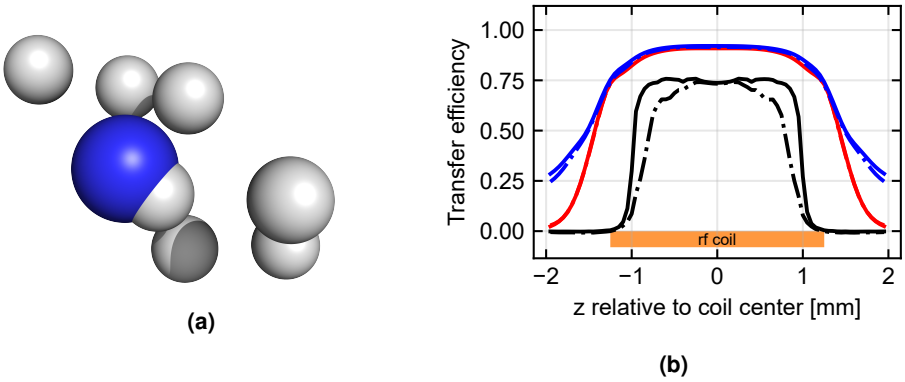

Figure 16: (a): Primary $H - N$ pair surrounded by remote protons. In the "3-spin and sampling" approach, the additional proton would sequentially assume several positions around the primary amide. **(b)**: Simulated efficiency profiles along the axial coordinate of the rotor of a 40-100 % ramp-CP (black), an OC transfer optimized using the "4-spin" approach (red), and an OC transfer optimized using the "3-spin and sampling" approach (blue). The performance of the transfers was calculated in a two-spin system (solid lines) and in a spin system containing remote protons (dot-dashed lines). The "4-spin" transfers 77.8 % of the magnetization detectable by the coil in a 2-spin system and 78.4 % with remote protons, whereas the "3-spin and sample" shape pair transfers 81.9 % in a 2-spin system and 81.0 % with remote protons.

In figure 16b one can see that the susceptibility of the new transfers to the presence of remote protons in the simulated spin system is in fact reduced to a negligible amount, when compared to the original optimizations. In addition, it seems that the concerns about overspecialized solutions from the "4-spin" approach were largely unfounded: While the transfer efficiency is indeed slightly higher in the spin system for which the transfer was optimized, the difference is well within the tolerance expected for a change within the spin system. Furthermore, also the "3-spin and sample" approach seems to produce shapes that are not significantly affected by additional protons. Both variations should enable achieving up to twofold the signal of ramped-amplitude experiments in

real samples (42.5 % vs. 78-82 % of the detectable signal is theoretically transferred).

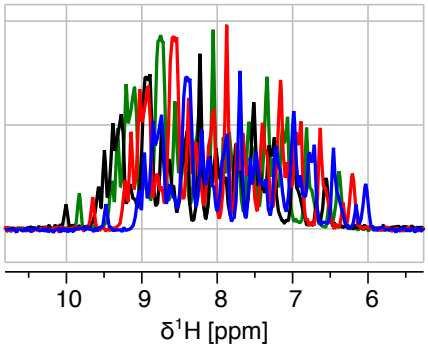

Figure 17: hnH spectra of ^{2}H,^{13}C,^{15}N-labelled microcrystalline chicken α-spectrin SH3 (10 % protonated at the exchangeable sites) using ramp-CP (black), a first-generation OC transfer (green), a "4-spin" transfer (red) and a "3-spin and sampling" transfer (blue). Spectra are shifted horizontally for better visibility of the different peak heights.

However, this advantage in simulations does not translate consistently into experimental results, as evidenced by the spectra in figure 17. While the "4-spin" transfer performs about 25 % better than the reference ramp-CP, so does the first-generation OC transfer from section 4.1 that was also tested in the same measurement session on the same sample. However, the latter transfer had previously been shown to be less efficient than the reference ramp-CP, and the increased efficiency in this setting is likely due to the lower degree of protonation at the exchangeable sites of the used sample. On the other hand, the S/N achieved by the "3-spin and sampling" optimization is only about equal to the one achieved by the ramp-CP, marking this approach as clearly suboptimal.

With the increased efficiency of the first-generation transfer in the proton-depleted sample, these results corroborate the suspicion that remote protons have a large effect on the efficiency of OC transfers. Nevertheless, neither the "4-spin" nor the "3-spin and sampling" approaches proved to be viable pathways to circumvent these issues.

4.1.3 Pulses composed of repetitive elements

In another approach to overcome the sensitivity towards interfering protons, pulses consisting of repetitive elements that were optimized by OC were created. This was done to reduce the number of degrees of freedom available to the optimization, and

thus possibly the degree of specificity for a certain set of conditions that the transfer can achieve. The concept is illustrated in figure 18. At first, top curves were calculated for several durations of the repetitive elements, ranging from a single rotor period to ten rotor periods, and a total pulse duration of up to 60 rotor periods (see figure 19). It was found that very short repetitive elements of one or two rotor periods lead to inferior transfers, and at least three periods are needed for adequate transfers.

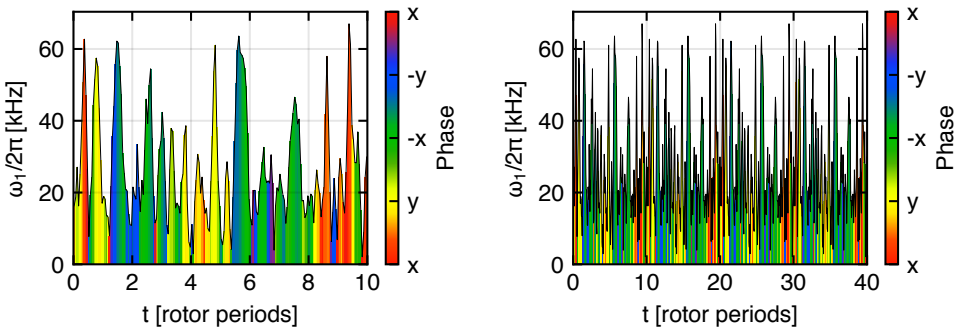

Figure 18: Left: One of the repetitive elements with a duration of 10 rotor periods. Right: The assembled pulse from four of these elements.

Optimizing the best of these transfers (with a duration of 40 or 42 rotor periods) further for robustness towards a range of chemical shift offsets and rf inhomogeneity (see figure 20) revealed that short repetitive elements can only achieve inferior transfer across a large range of rf fields and that an increased performance in larger spin systems is not automatically achieved when the number of parameters available to the optimization is lowered by this scheme. Still, some of these shapes are able to approximately match or slightly exceed the efficiency of ramp-CP in simulations.

Experimentally, most of the optimized transfers were outperformed by the reference experiment, and only one of them achieved a matching transfer efficiency. This comparison is shown in figure 21. It is nevertheless interesting that optimizing shapes consisting of repetitive elements is a possibility in principle, and should be kept in mind as an option for future optimization problems.

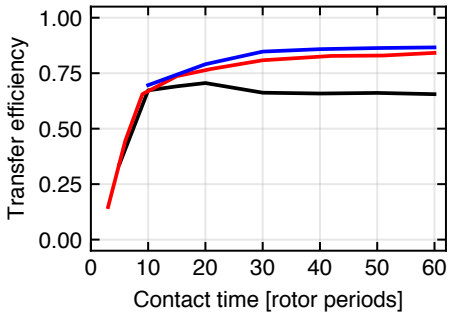

Figure 19: Top curves for H_x-N_x transfer pulses composed of repetitive elements of durations 1 (black), 3 (red), and 10 (blue) rotor periods.

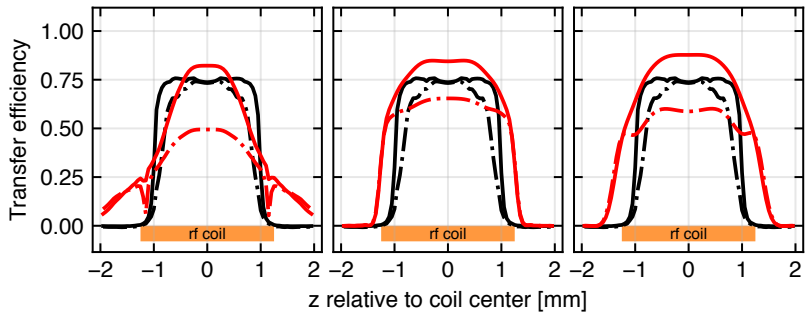

Figure 20: Simulated efficiency profiles along the axial coordinate of the rotor of a 40-100 % ramp-CP (black in all graphs), and of representative OC transfers composed of repetitive elements with a duration of 3 (left), 5 (center), and 10 (right) rotor periods per element for a total duration of 42, 40 and 40 rotor periods, respectively (red). The performance of the transfers was calculated in a two-spin system (solid lines) and in a spin system containing remote protons (dot-dashed lines). The optimized shapes transfer 53.2 %, 63.2 %, and 66.4 % of the magnetization detectable by the coil in a 2-spin system, and 35.4 %, 50.4 %, and 48.1 % with remote protons, respectively.

4.1.4 Optimizations started from conventional pulse schemes

The third approach that was tested in order to reduce the susceptibility of the OC transfers to the influence of remote protons was based on two ideas that were implemented simultaneously:

1. The rf amplitude on the ^1H channel was set to a fixed value for the whole transfer to effect a CW decoupling of sorts and possibly remove the influence of the remote protons.

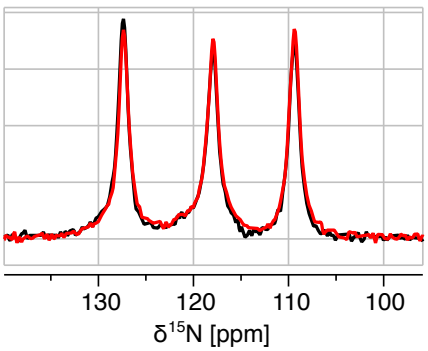

Figure 21: hN spectra of uniformly ^{2}H, ^{13}C and ^{15}N-labelled, N-terminally formylated methionine-leucine-phenylalanine tripeptide (f-(^{2}H,^{13}C,^{15}N)-MLF) using ramp-CP (black) and the most efficient repetitive-element OC transfer (repetitive elements of 10 rotor periods duration, red).

2. The starting values for the ^{15}N channel amplitudes were set to a ramp shape with a small amount of random noise (to avoid trapping in local minima). As ramp-CP transfers are robust against third-spin influence, an expectation was that optimizations started close to a known working condition would produce robust, but optimized transfers.

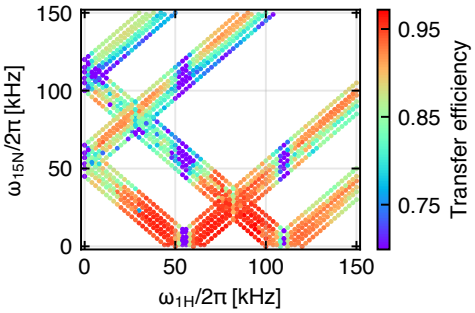

Figure 22: Transfer efficiencies of OC transfers with fixed ^{1}H amplitudes and ^{15}N amplitudes started from a ramp with random noise added. The optimizations were started close to the HH conditions at 55 kHz MAS.

Figure 22 shows the resultant transfer efficiencies from optimizations started close to known ramp-CP conditions in a two-spin system and with no robustness constraints (in essence a "top curve"). It is apparent that high initial ^{15}N rf amplitudes are detrimental to the final transfer efficiency reached by the optimization. Furthermore, very low and very high ^{1}H amplitudes are not conducive to high efficiencies either. However, within a "sweet spot" of intermediate ^{1}H and low ^{15}N starting amplitudes, very high transfer efficiencies can be achieved.

Unfortunately, trying to incorporate robustness against rf inhomogeneity into the transfer using this approach led to disappointing results, even before adding the additional robustness requirements to a range of chemical shift offsets. Therefore, this approach was abandoned without experimental tests.

4.1.5 Discussion

The results presented in the previous sections indicate that the optimization of $H-N$ transfers for MAS rates within the fast-spinning regime (about 60 kHz) is more challenging than initially anticipated. A limited discrepancy between the simulated and experimental advantages of OC optimized transfers over classical reference experiments, such as ramp-CP or adiabatic sequences, was expected. The performance of the ramp-CP used as a reference could be matched by some of the optimized transfers, and even exceeded in special circumstances, marking the approach as feasible in principle. However, the increase in the simulated transfer efficiency through the usage of OC optimized transfers would still suggest that a significant S/N advantage should be found experimentally.

The causes for this discrepancy between the expected and actual results may be manifold. The cause that was deemed most likely, and hence provoked the development of several approaches to decrease its severity, was the effect of the presence of remote protons on the transfer. Unfortunately, none of the approaches that were tried yielded satisfactory experimental results. Reducing the number of free variables in the optimization by reusing repetitive elements as in section 4.1.3 or fixing the amplitude on one rf channel as in section 4.1.4 did not yield the desired effect. Therefore, shape "over"specificity, if present at all, may be more a necessity for achieving high transfer efficiencies than an artifact of the other optimizations that needs to be avoided.

On the other hand, while the transfers shown in section 4.1.2 displayed comparatively good *in silico* performance, their experimental results were no better than those of the previous transfers. In addition and though an irrelevant finding for immediate practical applications, it is nevertheless interesting that an improvement can be measured when only one $H-N$ transfer, instead of multiple consecutive transfers, is performed. This

is the case even for the very first generation of shapes in a specific sample with low proton content (figure 23), and may indicate the presence of additional factors that are unaccounted for in the simulations hampering the experimental efficiencies of the optimized shapes.

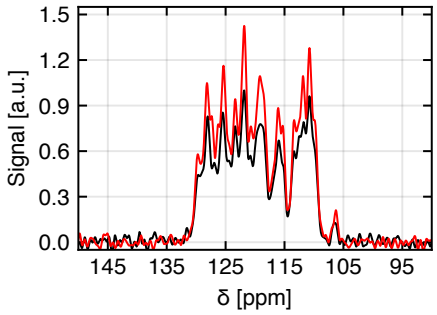

Figure 23: hN spectra using ramp-CP (black) and a two-spin OC transfer (red) of ^{2}H,^{13}C,^{15}N-labelled microcrystalline chicken α-spectrin SH3 (approx. 5 % protonated at the exchangeable sites).

This loss of efficiency through a second transfer suggests some kind of interaction between two (or more) transfers that severely decreases the overall transfer efficiency. One such factor might be the selection of certain molecular orientations with respect to the rotor (represented as crystallites in the simulation) by the OC transfers. If this selection were random, independently optimized transfers would likely have high efficiencies for different crystallites, reducing the overall transfer if these transfers were concatenated.

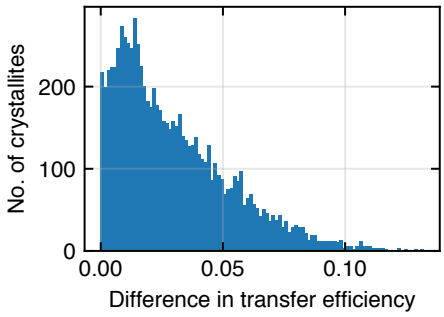

Figure 24: Histogram of the difference in transfer efficiency for a given crystallite between an $H - N$ and an $N - H$ OC transfer that were optimized independently of each other. In total, 8192 crystallites arranged according to the REPULSION powder averaging scheme[87] in its three-dimensional implementation in Spinach[79] were simulated.

Figure 24 shows, however, that the difference in the transfer efficiency for a given crystallite of two independently optimized shapes is small for the vast majority of crystallites. Hence, if the crystallite orientation at the start of the transfer is reproducible, the effect of crystallite selection should accordingly be small as well. In an idealized picture, this condition can be met when the transfers are started exactly an integer number of rotor periods apart from each other. In practice, slight variations in the rotation frequency make a perfect alignment highly unlikely and a certain amount of crystallite selection may be present. Resolving this issue would necessitate the reduction of the orientational dependency of the transfer efficiency, for example by optimizing for high-efficiency back and forth transfers with a variable delay of a duration from 0 to 1 rotor period between the individual transfer blocks. Optimizations of this kind have not been tested within the frame of this thesis.

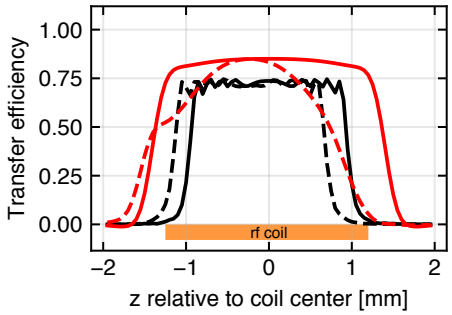

Figure 25: Effect of the misalignment of the rf profiles on the active channels: Simulated efficiency profiles along the axial coordinate of the rotor of a 40-100 % ramp-CP (black) and a pulse from the simple optimization runs (red). The performance of both transfers was calculated with aligned rf profiles on both channels (solid lines) and with the ^1H field shifted by –0.5 mm (dashed lines).

Additionally, several hardware properties may impede the performance of the OC transfers. One reason may be rf fields that are not spatially aligned on the ^1H and ^{15}N channels. This issue can be caused by improper balancing of the rf coil at the respective frequencies, leading to a distortion of the rf field and a shift of the maximum field region from the center of the coil. While this has the potential to also reduce the efficiency of standard CP transfers[88], the variable amplitude of the ramp-CP apparently compensates for this very well, and the main effect of one unbalanced channel is a shift of the transfer profile in the axial direction. On the other hand, this misalignment of the rf fields has a severe effect on the performance of OC shapes when not accounted for in the optimization (see figure 25). Because a theoretical

determination of the balance of the coil in a real probe is all but impossible, efforts were started to experimentally determine the actual rf field profiles within a coil (see section 5.3).

A lack of temporal synchronization between spectrometer channels may also present an issue, especially on older hardware. This was tested experimentally and found not to be an issue (data not shown). Furthermore, rf transients are often discussed as an experimental imperfection that causes a loss of S/N[89–93]. However, according to Tošner et al.[53], rf transients are a negligible imperfection for the discussed OC transfers and were thus disregarded in this work.

4.2 Scalability of OC-optimized shapes to different spinning frequencies

(This section briefly describes a project that has previously been published: Tošner, Z.; Brandl, M. J.; Blahut, J.; Glaser, S. J.; Reif, B. Maximizing Efficiency of Dipolar Recoupling in Solid-State NMR Using Optimal Control Sequences. Science Advances 2021, 7 (42), eabj5913[78]. See publication for author contributions.)

OC optimized shaped pulses for MAS NMR experiments are typically optimized for a single MAS frequency and only work within a small window of rotation rates surrounding the design frequency. However, different MAS rates are sometimes needed to avoid resonance conditions or due to mechanical limitations regarding the sample or probe. Conventionally, this would require the optimization of new pulse shapes for every desired spinning frequency, a process which requires a significant amount of computational effort. Therefore, the concept of scaling the shaped pulses to a desired MAS frequency was developed.

To correctly adjust an OC transfer optimized for a MAS rate ω_{MAS}^{opt} to a desired MAS rate ω_{MAS}^{new} and thus maintain rotor synchronicity, a scaling factor

$$\xi = \frac{\omega_{MAS}^{new}}{\omega_{MAS}^{opt}} \tag{39}$$

is used to scale the duration T of the shape according to

$$T_{new} = \frac{T_{opt}}{\xi} \tag{40}$$

and the rf field amplitudes ω_1 according to

$$\omega_1^{new} = \omega_1^{opt} \cdot \xi \tag{41}$$

Using these simple equations, it is possible to apply OC optimized transfers over a large range of MAS frequencies with little loss in efficiency (see figure 26 for the scalability curve of a representative OC transfer and figure 27 for an experimental example). With this approach, only a relatively small set of shapes, optimized at reasonably spaced MAS frequencies, is required for continuous MAS rate adjustability. While the scaling factor of the pulse duration needs to be accurate, the best practical results were achieved when the rf amplitudes were optimized experimentally. However, the high robustness of the OC transfers to deviations in the actual rf amplitudes ensures good performance even with misadjusted amplitudes.

A further extension of the applicable frequency range for a given OC pulse shape may be possible by incorporating scalability constraints into the optimization process, though it is unclear if the balance between the additional computational effort and the gained efficiency is favorable.

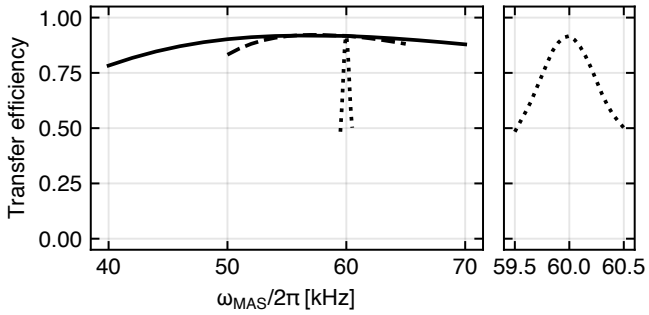

Figure 26: Simulated transfer efficiency of an $H - N$ OC transfer which was optimized for 60 kHz MAS at a range of MAS rates. Scaling was applied as explained in the text for: duration and rf amplitudes (solid line), only duration (dashed line), and not at all (dotted line).

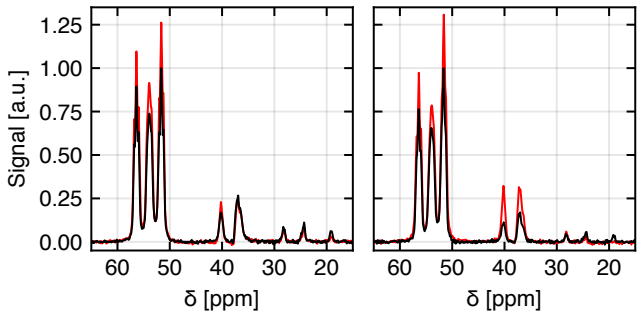

Figure 27: hnCa spectra of uniformly ^{13}C and ^{15}N-labelled, N-terminally formylated methionine-leucine-phenylalanine tripeptide (f-(^{13}C,^{15}N)MLF) recorded at 20 kHz (left) and 16.66 kHz (right) using an extensively optimized ramp-CP transfer as a reference (black) and a tm-SPICE OC transfer optimized for 20 kHz[53]. The tm-SPICE transfer was not scaled for its designed MAS rate, and scaled for the lower MAS rate of 16.66 kHz. Rf amplitudes were optimized experimentally for both rotation frequencies.

4.3 Transverse mixing sequences for phase-modulated signals from indirect dimensions

(This section describes a project also treated in a recently published paper: Blahut, J.; Brandl, M. J.; Pradhan, T.; Reif, B.; Tošner, Z. Sensitivity-Enhanced Multidimensional Solid-State NMR Spectroscopy by Optimal-Control-Based Transverse Mixing Sequences. J. Am. Chem. Soc. 2022, 144 (38), 17336–17340. doi:10.1021/jacs.2c06568. $N - H$ transfers were optimized and experiments at 55 kHz MAS were performed by the author of the thesis, other work was done by the collaborators.)

In conventional multidimensional NMR experiments, frequency discrimination in the indirect dimensions is nowadays achieved by acquiring two FIDs per increment following the States, time-proportional phase incrementation (TPPI) or States-TPPI procedure[94]. In this process, on average half of the available signal in the indirect dimension is lost by applying the frequency discrimination procedure. This signal may be recovered by utilizing a pulse scheme that transfers magnetization components oriented along both the x and y axes while conserving the orientation, and acquiring the spectrum in a manner consistent with the echo-antiecho (EA) scheme (figure 28). This methodology has also been referred to as the preservation of equivalent pathways (PEP)[95] or coherence order selective (COS)[96] technique.

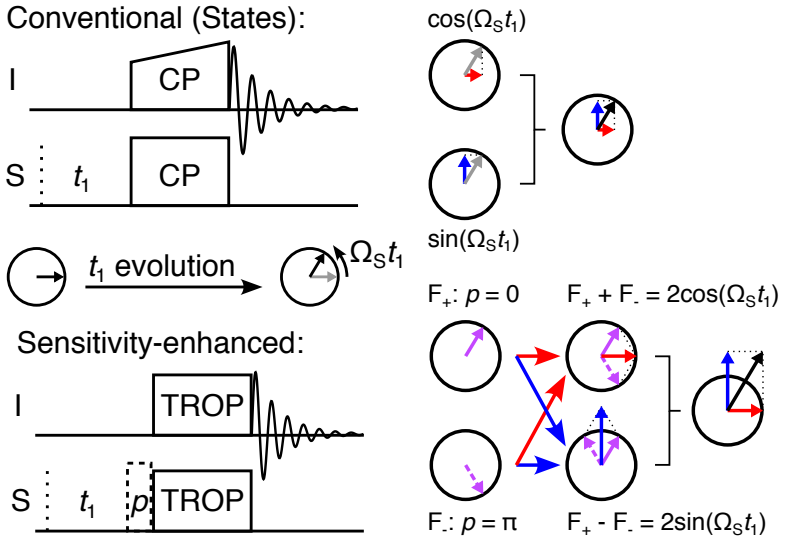

Figure 28: To achieve frequency discrimination in an indirect dimension, two components have to be acquired for each t_1 increment. In conventional sampling schemes, such as the States scheme[97], the sine and cosine (real and imaginary) components are selected and transferred in two distinct FIDs. The sensitivity-enhanced scheme records two phase-modulated FIDs through making use of a transverse mixing method (in this case called TROP: Transverse mixing Optimal control Pulses). These represent the echo (F_+) and anti-echo (F_-) pathways that may be discriminated by the π pulse *p*. By addition and subtraction of the respective FIDs, the sine and cosine components can be restored with a signal intensity increased by a factor of 2. However, due to the accumulation of independent noise, the gain in S/N is reduced to a factor of $\sqrt{2}$ per indirect dimension acquired in this manner.

In solution-state experiments, this leads to longer transfer delays due to the necessary additional INEPT-like transfer element for the second transverse component, during which the components are stored as multiple-quantum and longitudinal coherence, respectively[98]. Consequentially, the signal gained through the technique may be negated by increased relaxation during the additional duration of the pulse sequence,

making it unsuitable in particular for larger proteins with rapid relaxation rates[99]. Transverse mixing sequences and the usage of the PEP/COS principle are not new to solid-state NMR[74,100–103], but the concept has never been used for proton-detected assignment experiments.

In contrast to the double INEPT-like transfers necessary in solution-state NMR, OC optimized dipolar-based transfers (called TROP: Transverse mixing Optimal control Pulses) allow transversal transfers within the same time needed for a single-component transfer. Furthermore, the robustness of OC shapes towards rf inhomogeneity opens another avenue towards higher sensitivity independent of the gains through transverse mixing.

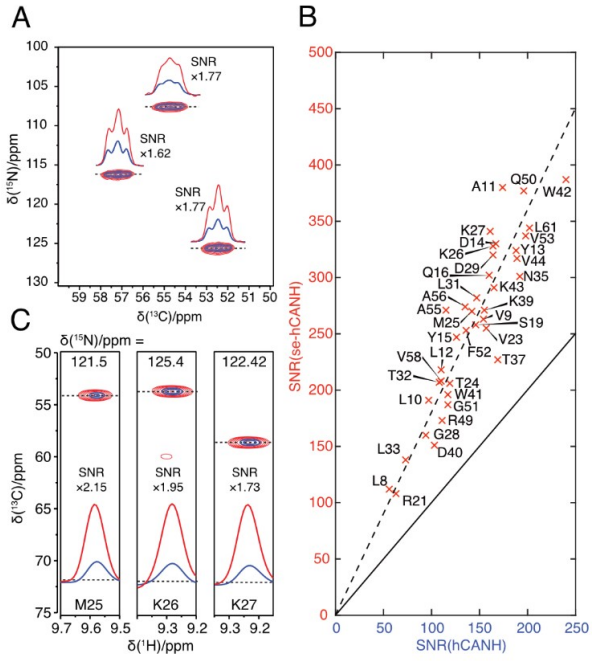

Figure 29: From the publication mentioned at the beginning of the section. Recording of (se-)hNCa spectra, data analysis and figure preparation was done by the collaborators. **A:** hNCa (blue) and se-hNCa (red) spectra of f-(^{13}C,^{15}N)MLF acquired at 20 kHz MAS, with insets showing the slices along the dashed lines and the ratio of S/N (se-hNCa / hNCa) noted beside the peaks. **B:** Residue-specific improvement of S/N in an se-hCaNH spectrum over a conventional hCaNH spectrum recorded at 55 kHz MAS on the same ^{2}H,^{13}C,^{15}N-labelled microcrystalline chicken α-spectrin SH3 sample (100 % protonated at the exchangeable sites). The solid line represents no improvement, the dashed line represents the average improvement in S/N by a factor of 1.8. **C:** $^{1}H-^{13}C$ strips from the hCaNH (blue) and se-hCaNH (red) spectra at the ^{15}N chemical shift indicated at the top, with inset 1D slices along the dashed lines.

The optimization protocol of these transverse mixing shapes was straightforward: The desired transfers $S_x \rightarrow I_x$ and $S_y \rightarrow I_y$ formed positive contributions to both the gradient and the target function. A penalty for the "cross-transfers" $S_x \rightarrow I_y$ and $S_y \rightarrow I_x$ was considered, as was a penalty for insufficient balance between the two pathways. However, both proved to be unnecessary as the transfers performed well in these respects even without additional constraints. While the $N \rightarrow H$ shapes used for the fast-spinning experiments were optimized by the author of this thesis, all $N \leftrightarrow C$ transfers were optimized by Jan Blahut and Zdeněk Tošner.

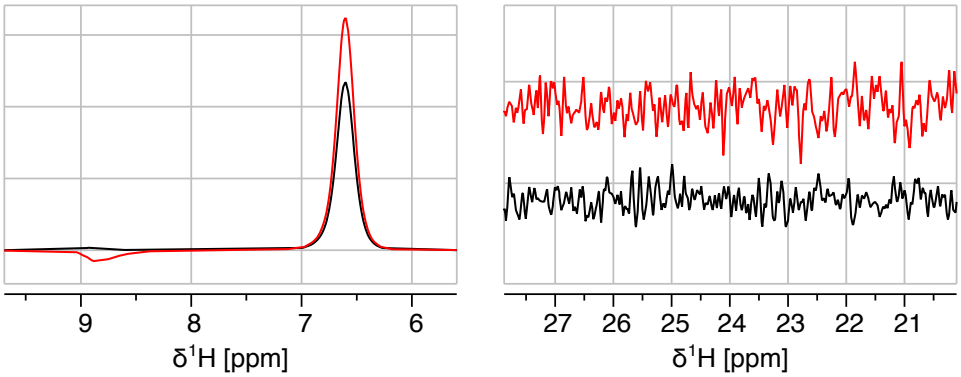

Figure 30: Slices from conventional (black) and sensitivity-enhanced (red) hNH spectra of f-(^{2}H,^{13}C,^{15}N)-MLF acquired at 55 kHz MAS. While the signal amplitude (left) is increased, the noise amplitude is increased as well by the sensitivity-enhancement recording scheme (right), negating the apparent gain in sensitivity. The observed S/N was 414 and 421 in the conventional and sensitivity-enhanced slice, respectively.

Both the gain through transverse mixing and through the enhanced robustness of OC pulses could be demonstrated in the hNCa spectrum acquired at slow spinning in figure 29. However, the average gain in the 3D experiment falls short of the theoretical gain of a factor of 2 that should be achieved through the sensitivity-enhancing recording scheme alone. This is very likely because the transverse mixing $N \rightarrow H$ pulses suffer from similar problems as the standard transfers presented in section 4.1 and do not achieve higher sensitivity than the conventional method (figure 30). Nevertheless, these shapes already allow the acquisition of three-dimensional experiments based entirely on transverse mixing pulses, and future developments towards higher-efficiency $H \leftrightarrow N$ transfers can be used as "plug-and-play" improvements in the same pulse sequences.

4.4 Spin-state selection and spin-state selective transfers

4.4.1 The TROSY effect

In standard multidimensional NMR experiments, nuclei not involved in an indirect dimension are decoupled during the respective evolution period, both to avoid splitting the fixed intensity of a single resonance into multiple signals, and to avoid the spectral crowding caused by the additional signals. However, this leads to peaks where the linewidths of the otherwise separated signals are merged. This is especially problematic for large molecules in solution[104,105] and flexible regions in solids[106,107], where the differential relaxation of the multiplet components, caused by different spin states of coupled nuclei, has a significant effect on the observed linewidths[108,109]. To exploit this, and therefore allow the investigation of larger proteins in solution, transverse relaxation-optimized spectroscopy (TROSY) experiments were developed that allow the selection and exclusive detection of the slowest-relaxing component[110,111].

An additional application of spin-state selective techniques lies in the reduction of the impact a misadjusted magic angle has on the linewidth of MAS solid-state NMR spectra[112]. This misadjustment is a major issue in probes which require flipping the stator in order to exchange the sample (predominantly standard-bore probes for large rotor sizes)[112], but even in probes with fixed stators, a precise adjustment of the magic angle can be a mechanical challenge and may shift when changing samples[113].

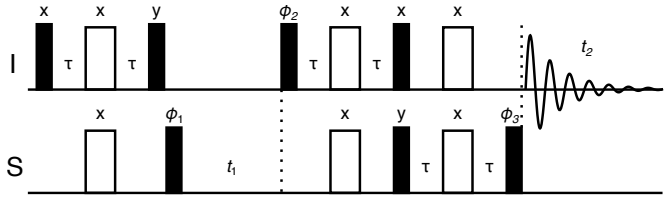

Figure 31: Original HN TROSY pulse sequence proposed by Pervushin et al.[110], albeit without the pulsed field gradients routinely employed in solution-state NMR. $\phi_1 = y, -y, -x, x$, $\phi_2 = 4(y), 4(-y)$, $\phi_3 = 4(x), 4(-x)$, $\phi_{receiver} = x, -x, -y, y, x, -x, y, -y$

In an NMR spectrum of a spin system containing two spins 1/2, I and S (^1H and ^{15}N in this case), with a scalar coupling between them, a detectable operator S_x is composed of the operators $I^{\alpha}Sx$ and $I^{\beta}S_x$, leading to a splitting of the S resonance

into two multiplet components generated by the coupling constant J. The transverse relaxation rates for the S resonance contain a dipolar coupling contribution

$$p = \frac{\gamma_I \gamma_S \hbar}{2\sqrt{2} r_{IS}^3} \tag{42}$$

and a CSA contribution

$$\delta_S = \frac{1}{3\sqrt{2}} \gamma_s B_0 \Delta\sigma_S \tag{43}$$

where γ_I and γ_S are the gyromagnetic ratios of I and S, $\hbar$ is Dirac's constant, r_{IS} is the length of the internuclear vector, and $\Delta\sigma_S$ is the difference between the largest and smallest principal components of the CSA tensor of S. The different states S^α and S^β now lead to differential transverse relaxation rates for the multiplet components

$$\begin{aligned} R_1 = (p - \delta_S)^2 (4J(0) + 3J(\omega_S)) + p^2 (J(\omega_I - \omega_S) \\ + 3J(\omega_I) + 6J(\omega_I + \omega_S)) + 3\delta_I^2 J(\omega_I) \end{aligned} \tag{44a}$$

$$\begin{aligned} R_2 = (p + \delta_S)^2 (4J(0) + 3J(\omega_S)) + p^2 (J(\omega_I - \omega_S) \\ + 3J(\omega_I) + 6J(\omega_I + \omega_S)) + 3\delta_I^2 J(\omega_I) \end{aligned} \tag{44b}$$

with ω_I and ω_S representing the respective Larmor frequencies of I and S, and $J(\omega)$ representing the spectral density function

$$J(\omega) = \frac{2\tau_c}{5(1 + (\tau_c \omega)^2)} \tag{45}$$

wherein τ_c is the rotational correlation time of the molecule. One of these relaxation rates (which one is dependent on the signs of the gyromagnetic ratios) will become small for the case $|p| \approx |\delta_S|$, leading to a narrower linewidth of the respective component[110].

Owing to the field dependence of δ_S, this effect is most pronounced at a certain B_0, whose value differs for different combinations of I and S[114].

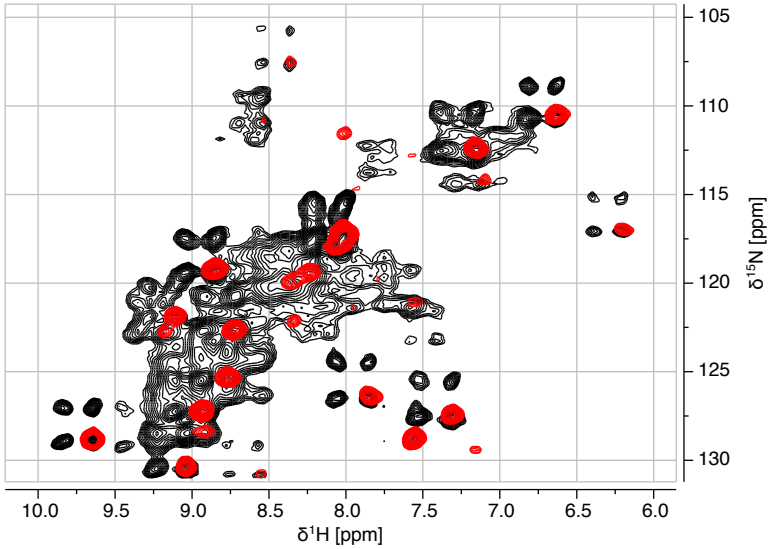

Figure 32: hNH-TROSY experiment of ^{2}H,^{13}C,^{15}N-labelled microcrystalline chicken α-spectrin SH3 (100 % protonated at the exchangeable sites) acquired with the pulse sequence from figure 31 (red) and non-decoupled hNH experiment (black).

When the slowest relaxing component (with the correspondingly narrowest linewidth) is selected, a spectrum with higher resolution will be obtained, at the expense of 75 % of the available signal. The pulse sequence originally used by Pervushin et al.[110] to record a 2-dimensional spectrum in this manner is displayed in figure 31, and a spectrum recorded of ^{2}H,^{13}C,^{15}N-labelled microcrystalline chicken α-spectrin SH3 (100 % protonated at the exchangeable sites) with the sequence from figure 31 is compared to a non-decoupled hNH spectrum containing all multiplet components in figure 32. In the 1D slices from these spectra (figure 33), it is apparent that the spin state selectivity of the sequence is excellent, even without the application of pulsed field gradients.

While the transfers utilizing the scalar coupling are an unavoidable choice in solution-state NMR, the much stronger dipolar coupling is an option for solid samples, promising higher experimental efficiencies and thus better S/N due to faster transfers and a reduction of relaxation losses. To create spin-state selective transfers via the dipolar coupling, OC optimization was employed.

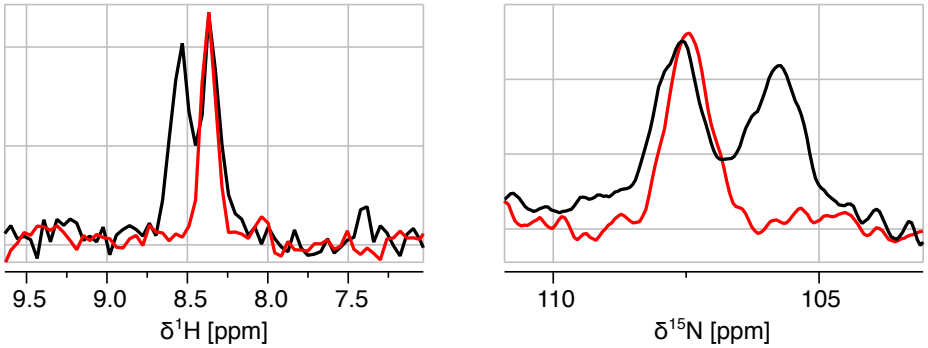

Figure 33: Traces through the TROSY component of an isolated multiplet (residue Gly51) in the spectra shown in figure 32 in the ^1H (left) and ^{15}N (right) dimension.

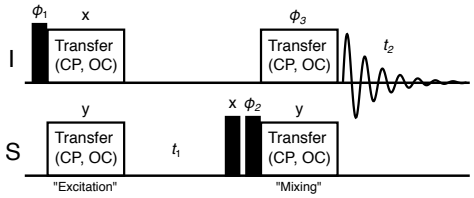

Figure 34: Pulse sequence suitable for recording non-decoupled, non-selective spectra (with non-selective transfers), semiselective spectra (with a nonselective first and a semiselective second transfer), or fully selective spectra (with two selective transfers, or a non-selective first and fully selective second transfer). $\phi_1 = y, -y, \phi_2 = 2(x), 2(-x), \phi_3 = 4(y), 4(-y), \phi_{rec} = y, -y, -y, y, -y, y, y, -y$

The required selectivity can in principle be achieved in a single fully selective mixing step, or by combining an excitation transfer selecting only the desired state of the I (^1H) spin with a mixing transfer selecting only the desired state of the S (^{15}N) spin. For both of these combinations, the pulse sequence shown in figure 34 is applicable. Another option is to use a nonselective excitation transfer followed by a selection element utilizing the scalar coupling, as shown in figure 35, which is employed in the pulse sequence shown in figure 36. All of these options were explored for this work.

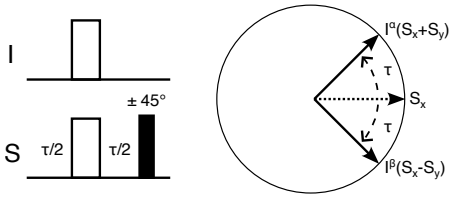

Figure 35: Pulse sequence element to select one of two components ($I^\alpha S_x$ or $I^\beta S_x$) after excitation of the S spin. After the evolution of the scalar coupling for a time $\tau = \frac{1}{4J}$, the two components are separated by 90° and one or the other component can be used further, while the other is discarded via the $\pi/2$ pulse.

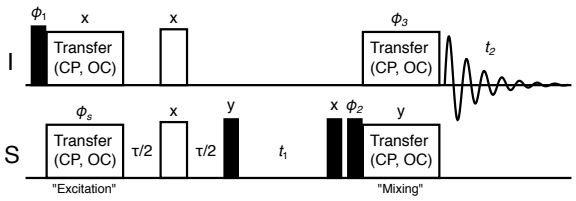

Figure 36: Pulse sequence suitable for recording fully selective spectra with only a semiselective second transfer. $\phi_1 = y, -y, \phi_s = x \pm 45°, \phi_2 = 2(x), 2(-x), \phi_3 = 4(y), 4(-y), \phi_{rec} = y, -y, -y, y, -y, y, y, -y$. The choice of the selected component is accomplished by changing ϕ_s.

Due to inconsistencies in literature and software concerning the signs and nomenclature of the specific spin states, especially considering the signs of the gyromagnetic ratios[27,94,110,115], the combination of spin states necessary to obtain the desired component was determined empirically both for the simulations and for the experiments. The nomenclature used in the following is expressed in figure 37 and consistent with the inputs given to SIMPSON for the OC optimizations. It is noteworthy that this arrangement changes when changing the `conjugate_fid` switch in the `par` section of a SIMPSON input file, and that the setting chosen by default is different from the one needed for OC optimizations. The arrangement represents a multiplet in a non-decoupled hNH experiment.

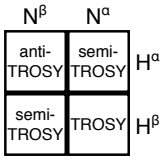

Figure 37: Mapping of the $(H|N)^{\alpha|\beta}$ spin states as defined in SIMPSON, onto a 2D hNH spectrum. The TROSY component is the narrowest, the anti-TROSY component the widest and the linewidths of the two semi-TROSY components fall in between.

4.4.2 Optimization of spin-state selective pulses

At the beginning of the optimization process, top curves for spin-state selective $H \rightarrow N$ ("excitation") and $N \rightarrow H$ ("mixing") transfers were calculated. For the excitation step, the target is clearly defined: Coherence needs to be transferred from H_x to $H^\beta N_x$ while suppressing the transfer to $H^\alpha N_x$. However, the mixing transfer may be specified with differing levels of stringency in terms of selectivity, and two approaches were used in this work. The less stringent approach aimed to transfer magnetization on the $H^\beta N_x$

operator to the correct target operator H_xN^α and to suppress transfers to H_xN^β as well as transfers to operators along the y axis, while not actively controlling transfers originating from $H^\alpha N_{x|y}$ (henceforth called "semiselective"). On the other hand, the more stringent approach also attempted to suppress transfers originating from $H^\alpha N_x$, which would make shapes of this type suitable for nonselective excitation schemes (henceforth called "fully selective").

To gauge the quality of selective transfer shapes, it is not sufficient to only look at their transfer efficiency for the desired component, but a way of quantifying their selectivity is also needed. Hence, a simple selectivity measure was used, which subtracts the sum of the absolute values of the amplitudes of all the specified undesired components ($I_{j,u}$) from the sum of the amplitudes of the desired components ($I_{i,d}$):

$$Sel = \sum_i \langle I_{i,d}|\rho(T)\rangle - \sum_j |\langle I_{j,u}|\rho(T)\rangle| \tag{46}$$

This measure of selectivity was used for all the subsequent top curves. While for the mixing shapes a rather long list of operators was counted towards the undesired components, the sum of these components was nevertheless mostly dominated by very few large contributors.

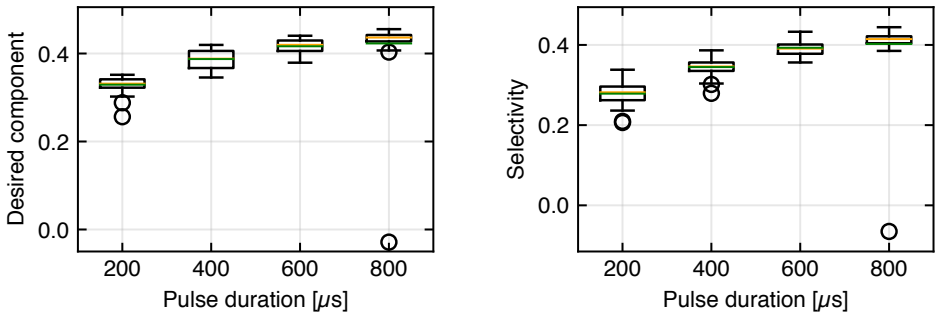

Figure 38: Top curve for a spin-state selective $H_x \rightarrow H^\beta N_x$ transfer. Left: amplitude of the desired component in the final density operator. Right: selectivity as defined in equation 46, with the undesired operator being $H^\alpha N_x$. Boxes in both plots range from the first to the third quartile, whisker length is 1.5-times the interquartile range, circles indicate fliers. Green bars indicate the median and orange bars indicate the mean of the data for each duration.

In the top curve of the excitation transfer (figure 38), it is apparent that both high

Robustness	none		+ Offset		+ rf inhomogeneity	
Run	$H^\beta N_x$	$H^\alpha N_x$	$H^\beta N_x$	$H^\alpha N_x$	$H^\beta N_x$	$H^\alpha N_x$
1 (600 µs)	0.440	0.007	0.455	0.018	0.416	0.033
2 (600 µs)	0.440	0.021	0.455	0.017	0.420	0.028
5 (800 µs)	0.455	0.011	0.459	0.014	0.428	0.022
6 (800 µs)	0.451	0.016	0.461	0.014	0.432	0.024

Table 2: Calculated resultant components of the optimized $H_x \rightarrow H^\beta N_x$ transfer shapes, $H^\alpha N_x$ being the undesired component. Numbers without robustness are directly taken from the top curve calculation.

transfer efficiencies and good selectivity can be achieved computationally. At a pulse duration of 600-800 µs, the transfer efficiency is approaching the theoretical maximum of 0.5, and the undesired operator is almost completely suppressed (see table 2). Therefore, pulses with these durations were optimized for robustness against frequency offset and rf inhomogeneity starting from the best resultant shapes from the set that went into the top curve. These further optimizations resulted in shapes that still display good transfer efficiencies and selectivities.

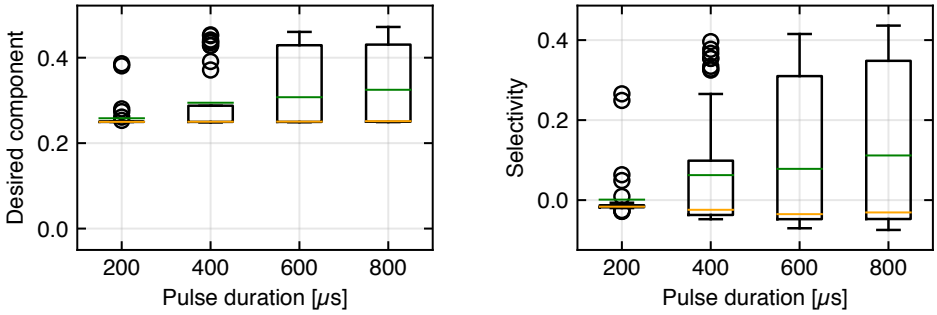

Figure 39: Top curve for a partially spin-state selective ("semiselective") $H^\beta N_x \rightarrow H_x N^\alpha$ transfer. The left graph indicates the amplitude of the desired component in the final density operator, the right graph represents the selectivity as defined in equation 46, with the undesired pathways being $H^\beta N_x \rightarrow H_x N^\beta | H_y N^{\alpha|\beta}, H^\beta N_y \rightarrow H_{x|y} N^{\alpha|\beta}$. Other transfer pathways, in particular $H^\alpha N_x \rightarrow H_x N^\beta$, were not controlled against. Boxes in both graphs range from the first to the third quartile, whisker length is 1.5-times the interquartile range, circles indicate fliers. Green bars indicate the median and orange bars indicate the mean of the data for each duration.

For the semiselective mixing transfer, the situation looks quite different and most of the optimized shapes display low transfer efficiencies combined with lackluster selectivities (figure 39). However, a subset of the random initial conditions produced shapes with both good efficiency and selectivity. The best of these, at a duration of 600 µs were

Robustness	none		+ Offset		+ rf inhomogeneity	
Run	Desired	Undesired	Desired	Undesired	Desired	Undesired
1	0.460	[a]: 0.030	0.467	[a]: 0.031	0.428	[a]: 0.033
		[b]: 0.013		[b]: <0.01		[b]: 0.018
2	0.459	[a]: 0.023	0.464	[a]: 0.031	0.435	[a]: 0.057
		[b]: 0.012		[b]: 0.050		[b]: <0.01
3	0.458	[a]: 0.028	0.459	[a]: 0.039	0.435	[a]: 0.061
		[b]: 0.058		[b]: <0.01		[b]: <0.01

Table 3: Calculated resultant components of the optimized $H^{\beta}N_x \rightarrow H_xN^{\alpha}$ transfer shapes, the undesired pathways being [a]: $H^{\beta}N_x \rightarrow H_xN^{\beta}$ (semi-TROSY), [b]: $H^{\beta}N_y \rightarrow H_yN^{\alpha}$ (orthogonal to the desired component). All other undesired pathways exhibit amplitudes below 0.01. Numbers without robustness are directly taken from the top curve calculation.

selected for further optimization including robustness constraints. The progress of these optimizations can be reviewed in table 3, where it is apparent that both transfer efficiency and selectivity only suffer slightly when enhanced robustness against offset ranges or rf inhomogeneity is demanded. Although in the top curve, several seeds at 400 µs duration almost meet the performance of the most efficient shapes at longer durations, no shorter shapes were optimized further.

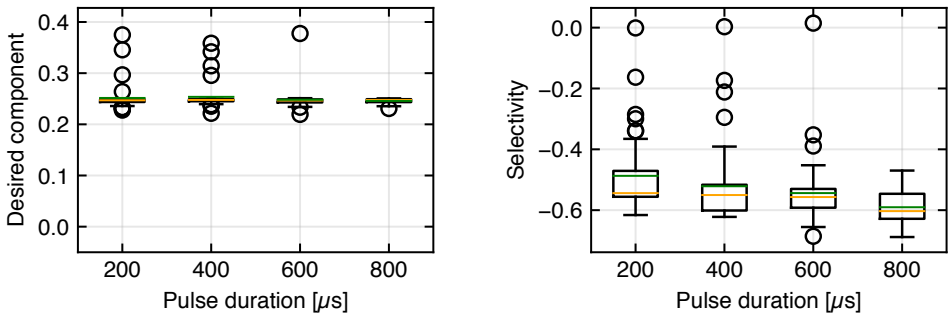

Figure 40: Top curve for a fully spin-state selective $H^{\beta}N_x \rightarrow H_xN^{\alpha}$ transfer. The left graph indicates the amplitude of the desired component in the final density operator, the right graph represents the selectivity as defined in equation 46, with the undesired pathways being $H^{\beta}N_x \rightarrow H_xN^{\beta}|H_yN^{\alpha|\beta}, H^{\beta}N_y \rightarrow H_{x|y}N^{\alpha|\beta}, H^{\alpha}N_{x|y} \rightarrow H_{x|y}N^{\alpha|\beta}$. Boxes in both graphs range from the first to the third quartile, whisker length is 1.5-times the interquartile range, circles indicate fliers. Green bars indicate the median and orange bars indicate the mean of the data for each duration.

Finally, the top curves for the fully selective mixing transfer display that this problem appears to be exceedingly difficult to solve (figure 40). While most seeds result in a transfer efficiency for the desired component around 0.25 with a very narrow distribution

regardless of the pulse duration, some outliers present better efficiencies. However, the amplitudes of the undesired components overshadowed even the performance of the best shapes.

Figure 41: Simulated efficiencies of the transfers corresponding to the respective multiplet components effected by the shape pair used to record the red spectrum in figure 45, over the course of its optimization. The rightmost matrix represents the pulses that were used in the experiment, the two panels to the left represent intermediate stages of the optimization.

Nevertheless, optimizations of several shapes for robustness was attempted, and the result of the most successful run is illustrated in figure 41. It is clearly visible that additional robustness requirements strongly reduce the transfer efficiency for the desired TROSY component, while the suppression of the anti-TROSY component is worsened. The amplitudes of the two semi-TROSY components are largely unaffected by the robustness constraints.

4.4.3 Experimental results

In the next step, the shapes optimized for robustness were applied in experiments to test whether they would meet the expected selectivity criteria. Therefore, hNH spectra of SH3 were recorded with appropriate pulse sequences to show faults in the expected selectivity.

For testing the excitation transfer shapes, the pulse sequence shown in figure 34 (no additional selection element) was used. As the first transfer of the sequence, an optimized shape pair was used, and the second transfer was accomplished by a ramp-CP. A representative spectrum (red) is compared against a non-decoupled, non-selective hNH spectrum (black) in figure 42. It is obvious that the transfer shape pair that effects a spin-state selective transfer in simulation does transfer polarization, but does not

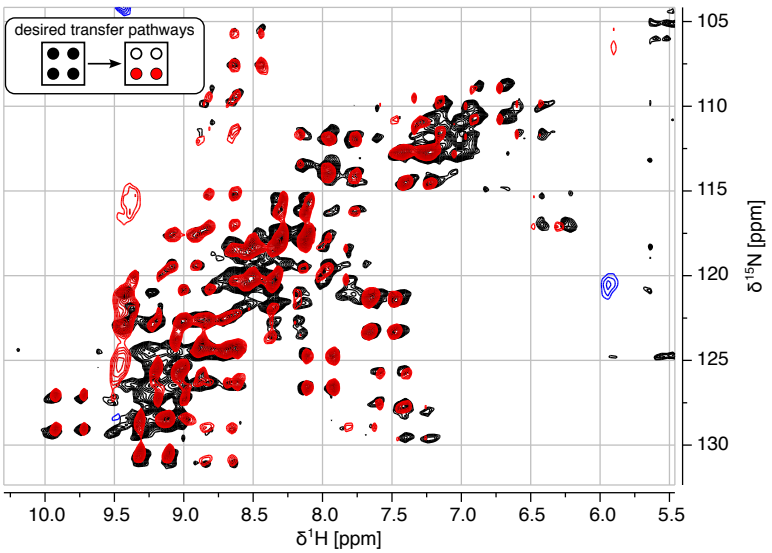

Figure 42: Spectra displaying the experimental effect of an OC optimized spin-state selective $H-N$ transfer shape pair. Black: Non-decoupled hNH spectrum of ^{2}H,^{13}C,^{15}N-labelled microcrystalline chicken α-spectrin SH3 (approx. 5 % protonated at the exchangeable sites). Red: Spectrum of SH3 (10 % protonated at the exchangeable sites) acquired using the optimized shape pair for the $H-N$ transfer and a ramp-CP for the $N-H$ transfer. Inset shows the desired selectivity.

exhibit any appreciable selectivity, in the experiment. Furthermore, the distribution of transfer efficiencies for different residues and multiplet component seems rather heterogeneous.

The semiselective mixing transfers were first tested in the same pulse sequence, but with a ramp-CP for the first transfer and the shape pair in test as the second transfer. A representative test is shown in figure 43 (black). As may be expected for shapes not optimized to suppress transfers from $H^{\alpha}N_{x|y}$, the selectivity is not complete. This type of shape permits both the TROSY and anti-TROSY components, while fully suppressing the semi-TROSY components. In preceding optimizations performed by Dennis Huber, shapes that suppress the TROSY and anti-TROSY components while permitting both semi-TROSY components were also generated due to the aforementioned difficulties surrounding sign conventions (data not shown).

To achieve complete selectivity in an experiment with only these semiselective shapes, the additional selection element, explained in figure 35 and included in the pulse sequence in figure 36, was introduced. By appropriately choosing the relative phase

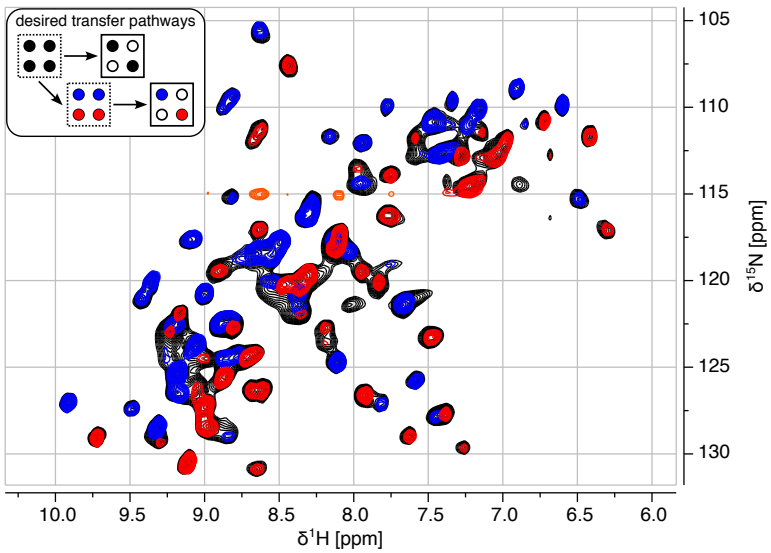

Figure 43: Spectra of ^{2}H,^{13}C,^{15}N-labelled microcrystalline chicken α-spectrin SH3 (10 % protonated at the exchangeable sites) displaying the effect of the semiselective transfer, and the additional scalar selection element. Black: hNH spectrum acquired with ramp-CP $H-N$ transfer and semiselective $N-H$ transfer. Red and blue: Pulse sequence with the scalar selection element (figure 36) with phases to select the TROSY and anti-TROSY component, respectively. Inset shows the desired selectivities, multiplets in dotted boxes represent intermediate stages of the experiments.

between the excitation transfer pulse and the first $\pi/2$ pulse on the S channel, one can select one or the other row of the multiplet, from which the desired single component is then selected by the semiselective OC shape pair (red and blue spectra in figure 43).

From the traces through the TROSY component of the Gly51 signal in these spectra (shown in figure 44), it becomes apparent that the scalar element slightly affects the signal amplitude of the desired component. Hence, full selectivity without additional pulse sequence elements would be preferred. On the other hand, the suppression of the semi-TROSY components through the OC optimized shape pair is highly effective.

However, although full spin-state selectivity without additional selection elements would be desirable, the optimized "fully selective" shape pair only yielded disappointing results (see figure 45). While transfer is achieved, it is no more selective than the semiselective shape pair (figure 46 shows a comparison between the TROSY and anti-TROSY components from the "fully selective" spectrum), but with less than half the transfer efficiency (see figure 47). Hence, this optimization protocol does not seem to

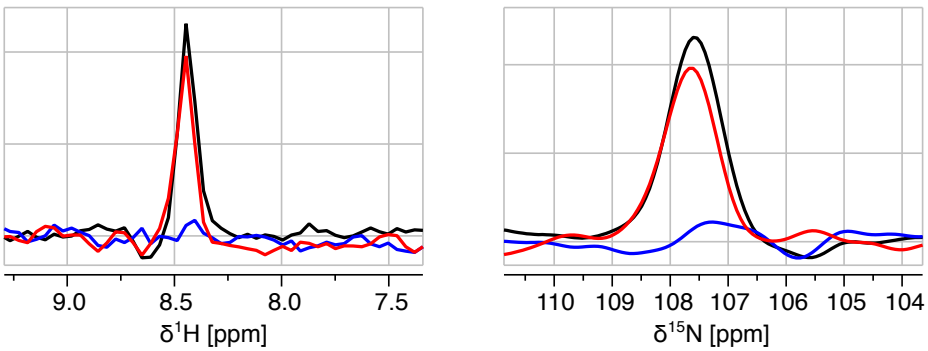

Figure 44: Traces through the TROSY component of an isolated multiplet (residue Gly51) in the spectra shown in figure 43 in the ^1H (left) and ^{15}N (right) dimension.

offer any advantage over the semiselective protocol.

4.4.4 Discussion and outlook

The most successful approach from the ones outlined above is doubtless the usage of the scalar selection element together with a semiselective mixing shape pair. This combination yields good spin-state selectivity combined with only a small penalty in S/N from the scalar element. Unfortunately, at the time of writing no experiments had been performed that would allow a comparison of the S/N of this scheme to the original TROSY sequence (the spectra in figures 32 and 43 were recorded on different samples with different degrees of protonation at the exchangeable sites).

On the other hand, both the excitation and the fully selective mixing transfers failed to experimentally fulfill the expectations built by the simulations for unknown reasons. Since in both cases transfer was actually achieved, but without the intended selectivity, user error in the experimental implementation can probably be excluded. Other possible reasons for the failure could lie in effects unaccounted for in the simulations, such as the $H-C_\alpha$ dipolar coupling, whose magnitude, at approximately 3 kHz, would be sufficient to interfere significantly within the duration of the transfer pulses. However, its effects should be adequately removed by the employed 55 kHz MAS. It is also conceivable that there are physical barriers that prevent these kinds of transfers in general, but in this case they should also fail to work in the numerical simulations. Including a phase

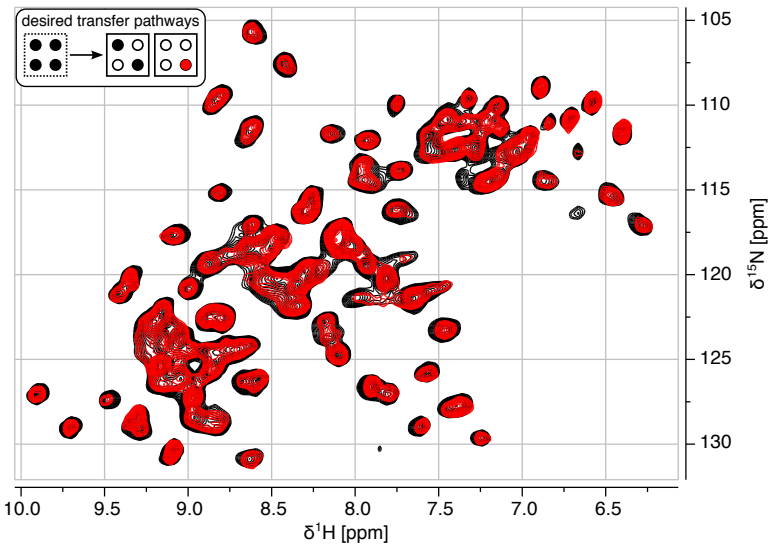

Figure 45: Spectra of ^{2}H,^{13}C,^{15}N-labelled microcrystalline chicken α-spectrin SH3 (10 % protonated at the exchangeable sites) displaying the effect of the fully selective transfer (red) compared to the semiselective transfer (black). Inset shows the desired selectivities, the multiplet in the dotted box represents an intermediate stage of the experiments.

cycle into the optimization to potentially simplify the selection of the correct coherence transfer may be an option, but this has not been tried yet.

Spin state selection through a Transferred Echo Double Resonance (TEDOR)[116]-like pulse sequence, with an average Hamiltonian analog to the one of the selection element, was tested in simulations and works for a two-spin system within a single crystal, but not for multiple crystallites with a random distribution due to the orientational modulation of the dipolar coupling. However, it may be possible through OC optimization to generate shaped pulses to serve the same purpose as the scalar selection element, but in a shorter time through the usage of the dipolar coupling. In a second step, such a selection element could be directly coupled to a standard transfer shape and cooperatively optimized, increasing experimental efficiency both through a higher transfer efficiency and through the reduction of relaxation losses.

An issue of dipolar-based spin-state selective shapes may be that the effective dipolar coupling is reduced in residues with high flexibilities (low order parameters). However, these flexible regions benefit most from the application of TROSY techniques[106,107]. This would likely necessitate the optimization of different shapes that are tailored to

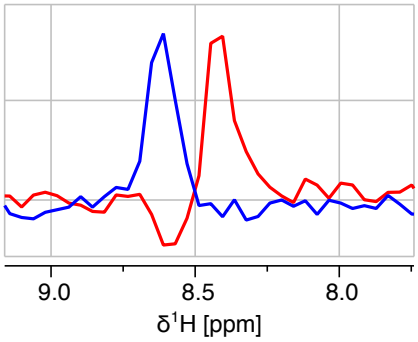

Figure 46: Traces through the top (blue) and bottom (red) peaks of an isolated multiplet (residue Gly51) in the fully selective spectrum shown in figure 45.

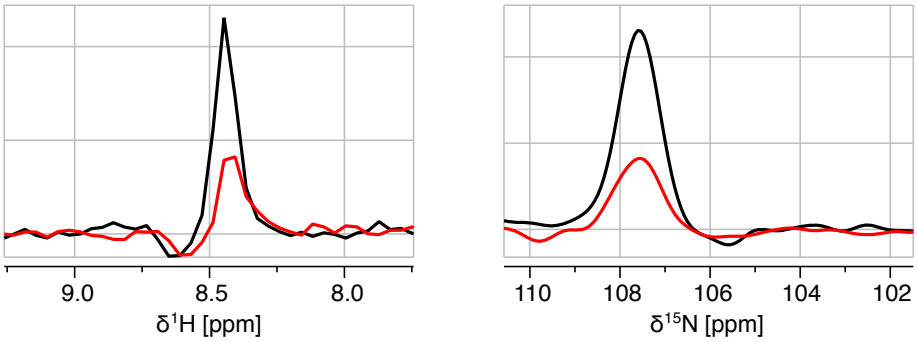

Figure 47: Traces through the TROSY component of an isolated multiplet (residue Gly51) in the spectra shown in figure 45 in the ^{1}H (left) and ^{15}N (right) dimension.

the weaker dipolar coupling, but should not pose a fundamental problem. Potentially reduced spin-state selectivity of such shapes for rigid regions may be countered by including a short "purge CP", which would only affect these regions with high order parameters and high effective dipolar couplings, to negate all signal from these rigid portions of the sample.

One further option for enhancing the S/N of solid-state TROSY experiments is the application of pulse sequences and transfers that lead to phase-modulated signals in the indirect dimension, employing the concept presented in section 4.3 to spin-state selective experiments. This approach has already been applied in solution-state NMR by Pervushin et al.[111] and would increase the S/N by $\sqrt{2}$ for each indirect dimension, if the creation of spin-state selective shapes that effect transverse mixing is possible. It would also allow the application of the TROSY concept within higher-dimensional experiments without an excessive loss in S/N.

5 Results II: Countering challenges of MAS NMR hardware

The challenge of spinning a sample at a frequency on the order of 100 kHz necessitates several compromises in the design of the probe and the rotor. For instance, the frictional heating of the rotor by its air bearings can lead to the loss of water from the sample, which will likely destroy the structural integrity of biological substances. This must be prevented by adequately sealing the rotor. Another issue is the packing of wet biological samples into ever smaller rotors, a task which is nowadays accomplished with an ultracentrifuge and needs adequate fixtures. Finally, the rf circuit within the probe will generally react differently depending on the frequency, leading to field distributions that are not identical for all the nuclei within an NMR experiment. This chapter will present approaches to lessen the impact of these issues.

5.1 Water retention in 1.3 mm rotors

The air bearings used in MAS rotor-stator systems lead to significant heating of the rotor while spinning fast, which may damage biological samples through the elevated temperature alone[51]. However, a problem that is particularly pronounced in the Bruker 1.3 mm rotor system is that the samples tend to dehydrate even after short periods of spinning. Therefore, the water needs to be retained by the use of sealing spacers ("plugs") made from an elastic material (see figure 48a). However, while the plugs offered by Bruker are very effective against dehydration, they occupy 2.2 mm of the 5 mm of available sample volume inside the rotor. Due to a shift of the NMR coil within the stator, a significant portion of the volume occupied by one of the plugs is still in a volume inside the coil with high rf field. Therefore, some sample volume that

would be available for detectable sample is wasted. To ameliorate this disadvantage, specially shaped sealing spacers were designed to better utilize the available sensitivity of the coil (see figure 48b).

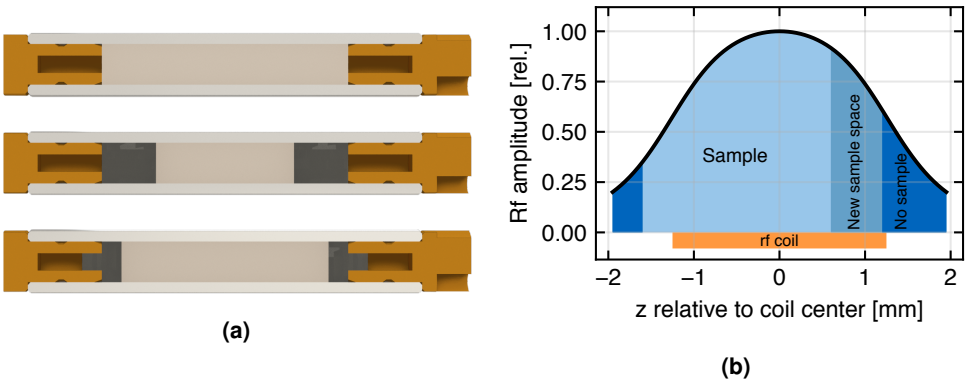

Figure 48: (a): From top to bottom: Assembled rotor without spacers, with Bruker sealing spacers, and with newly designed sealing spacers. **(b)**: Sample distribution within the rf field of the NMR coil: Due to the shift of the coil from the center of the rotor, potential sample volume is lost by the usage of the Bruker plugs and can be regained by utilizing shortened sealing elements.

These new spacers were originally designed to only occupy 0.5 mm of the available sample space per side, a dimension which could later be improved to 0.4 mm, allowing for a theoretical gain of 21 % and 23 %, respectively, in signal amplitude assuming perfect excitation within the full sample volume. However, in contrast to the Bruker spacers which are die-cut from a sheet of material and roughly cylindrical, the new design with its more intricate shape has to be cast or injection molded.

The actual sealing element of these spacers is a disc with a thickness of 0.5 mm (later reduced to 0.4 mm). To prevent this relatively thin disc from tilting within the rotor, which would open a gap for water to escape, a stem was added to interface with the center bore of the rotor cap.

For testing the design, a mold was manufactured by the machine shop of the department according to the drawings shown in figure 49. This mold consists of a base, the plate actually containing the individual cavities shaped in the negative shape of the plugs, a rim to contain the uncured material, and a top plate to cap the individual cavities of the central mold plate. However, the top plate was no longer used after the first try, as it was easier to remove the plugs from the mold while they were still attached to the

excess layer of material on top of the mold plate (see figure 50). They were later cut free from that excess layer using a scalpel.

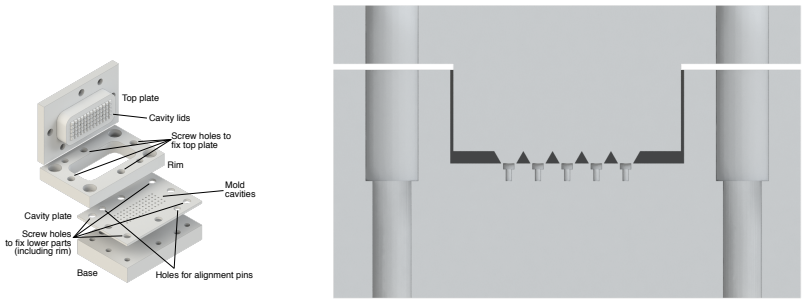

Figure 49: Left: Exploded view of the mold designed to form the prototype plugs from silicone potting compound. Right: Cross-section of the fully assembled mold.

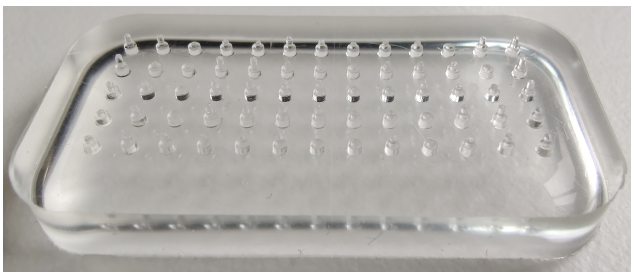

Figure 50: Layer of excess material from the mold with the silicone plugs still attached. They would later be cut free with a scalpel.

This test mold was used to shape plugs from a silicone potting compound, Dow Sylgard 184. While convenient for testing, the presence of abundant protons within the compound made it potentially suboptimal for proton-detected NMR applications. In addition, its Shore A durometer of 43 (according to manufacturer specifications) in the cured state was too low for the plugs to be practical. However, these tests showed that the principle was sound and the plugs could prevent sample dehydration.

After changing the design of the plugs slightly by shortening the stem from 1 mm to 0.4 mm, and thinning the sealing element to 0.4 mm as well, a batch of perfluoroelastomer (FFKM) plugs was ordered from the Taiwanese company Fluorez which specializes in the manufacture of fluoroelastomer parts. For further testing, they were manufactured from two similar compounds (FC750B and FU750N), both of which possess a Shore A durometer of 75. While this still proved to be rather soft considering the size of the plugs, it is nevertheless much more practical than the silicone potting compound. Both

of the plug designs are shown in figure 51.

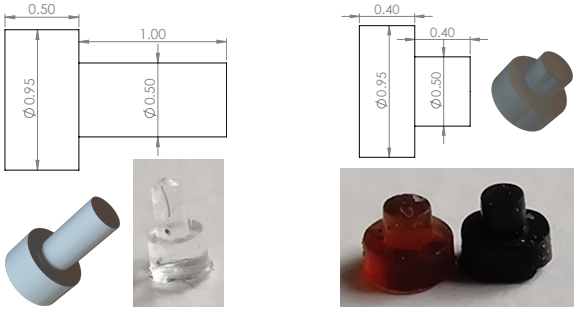

Figure 51: Drawing, render and photo of an initial silicone plug (left) and of final FFKM plugs (right). The amber FFKM plug is manufactured from the FU750N material, the black one from the FC750B compound. Note the shortened stem of the final plugs when compared to the initial design of the silicone plugs.

The handling and installation of the spacers into a rotor remains an issue. Originally, it was planned that the stem of the spacer could be inserted into the central bore of the rotor cap and this "plug-cap unit" could then be inserted into the rotor with relative ease. However, the high elasticity of the material and the small size of the stem in combination with manufacturing tolerances in both the plugs and the rotor caps generally make this impossible: The stem cannot easily be inserted into the rotor cap. Carefully inserting the plug into the rotor using tweezers and then pushing it into its final position when inserting the rotor cap proved to be a viable option, although it requires rather fine motor skills. Making the stem narrower would possibly help in this regard, but it would necessitate the considerable additional expense of manufacturing a new injection mold.

The two tested compounds differ in their 100 % modulus as well as their chemical properties: The FC750B compound is specified as a "chemical resistance enhanced" compound, the FU750N compound is listed as "ultra-pure, low outgassing", without more exact specification of the nature of the outgassed chemicals in either case. While both batches of spacers are usable, and it is unlikely that any chemicals emitted by the spacers would significantly influence a sample, for exceptionally important or sensitive samples, using the ultra-pure material may be advisable. However, due to the lower 100 % modulus of the material, they require slightly more delicate handling to insert them into a rotor.

From the ^{13}C direct excitation spectrum in figure 52, it is apparent that there is a

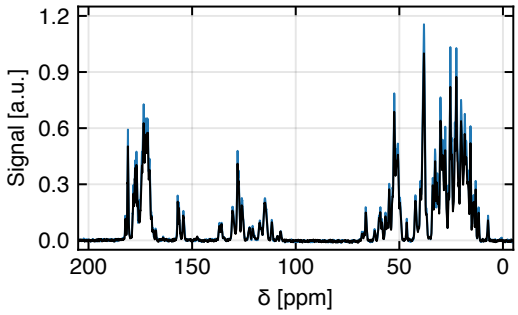

Figure 52: ^{13}C direct excitation spectra of microcrystalline SH3 protein in a rotor sealed with Bruker (black) and newly designed silicone (blue) plugs.

practical gain in S/N from the utilization of a shorter plug at the bottom of the rotor, which can be quantified to 16 %. This compares reasonably well to the 21 % that may be expected from the difference in sample volume and the detection efficiency, and proves that an improvement of S/N is possible by extending the available sample volume. However, a small discrepancy exists, and three reasons may be responsible for that.

First, the excitation in the sample volume enabled by the usage of the new plug is not fully efficient. This is due to the flip angle of the excitation pulse, which was calibrated for the whole sample, and represents a compromise probably most ideal for the region of highest rf field. Second, a certain margin of error needs to be allowed for when packing the sample: Once the plug is inserted into the rotor, it is all but impossible to remove again without also at least partially removing the sample (it needs to be pushed out from the other side). If there were too much sample in the rotor and one were not able to close the cap, this would mean the potential loss of some or all of the sample already packed into the rotor. Third, the rf field may be asymmetric about the center of the coil (see section 5.3), hampering the detection efficiency within the volume that was previously occupied by a spacer.

However, reaping a benefit in S/N from the usage of shorter sealing elements still is a challenge at the time of writing. The coil does produce a relatively high rf field in the additional sample volume, which by the principle of reciprocity means that the detection efficiency is also high. On the other hand, it is already outside the volume where most conventional ramp-CP transfers display high (or any at all) transfer efficiency. This

further highlights the need for OC optimized shapes that effect a highly efficient transfer across a large range of rf fields.

5.2 Packing tools for ultrafast MAS rotors

A very common way of packing solid-state NMR samples into rotors is by using an ultracentrifuge. This approach can be applied to microcrystalline and fibrillar proteins to greatly facilitate the packing process, but it also allows the direct sedimentation of macromolecules into the rotor without prior crystallization[117–121]. The latter approach enables the use of solid-state NMR techniques on macromolecules that are not easily investigated by solution-state NMR due to their size, but also cannot be crystallized[122].

However, at the time of writing of this thesis, no commercial tools for packing 0.7 mm rotors were available, and 0.7 mm rotors were routinely packed by placing them inside a 1.3 mm rotor and using the packing tool for this rotor size. While this method does work, it contaminates the outside of the 0.7 mm rotor with sample, and it leads to a considerable amount of sample being wasted due to the difference in volume between the rotors. Furthermore, it is possible that one or both of the rotors are damaged by the direct ceramic to ceramic contact, which may lead to a rotor crash when spinning is attempted.

Rebecca A. Stevens has published designs for such tools in her thesis[123], but the drawings describe an implementation that is not suitable for our ultracentrifuge rotor. In addition, her designs require direct handling of the tiny 0.7 mm rotors, which is not optimal.

As a consequence, her design was first adapted to the dimensions of the buckets in our ultracentrifuge and the capabilities of the departmental machine shop. Later, changes were made to enable the usage of the toolkit provided by Bruker for the handling of their 0.7 mm rotors. Both variants of the tool were manufactured by the departmental machine shop from polyether ether ketone (PEEK).

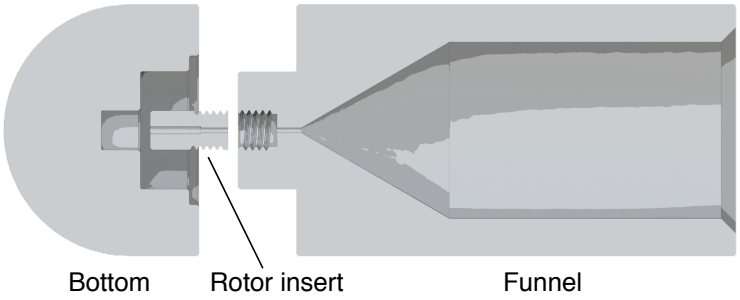

Figure 53: Rotor packing tool based on a design from Rebecca A. Stevens' thesis[123] for use with the ultracentrifuge rotor model Beckman SW-32 Ti.

The first iteration of changes concerned mainly the external dimensions of the tool, because the buckets on the ultracentrifuge rotor available in the author's laboratory are much bigger than the tool was originally designed for. Hence, the overall length of the tool was expanded to 65 mm and its diameter to 25.65 mm. These changes also allow the sedimentation from a larger amount of sample solution in one run.

An additional change is the increase of the included angle of the funnel. The very steep angle in the drawings from Warwick University is necessary for their workflow, which includes the sedimentation of proteins at very high acceleration in a fixed-angle ultracentrifuge rotor. The included angle in the funnel must therefore be acute enough to allow the passage of protein into the reservoir bore while at the fixed angle of the rotor. This is not necessary for our intended use in a swinging-bucket rotor only. A more obtuse included angle is much easier to machine and provides an even larger volume from which sample can be sedimented in a single centrifuge run, which is preferable for some of our use cases. This initial version can be viewed in figure 53.

During the first dry assembly of this tool with a MAS rotor, the rotor could not be removed from the rotor insert without destroying the latter in the process. This was due to a manufacturing issue: The hole receiving the rotor and connecting it to the funnel was not designed with a consistent diameter. The part of the hole that only passes sample into the rotor is specified to have the same inner diameter as the rotor itself, whereas the part that receives the rotor has to be large enough to do so. The larger part of the hole was made with a standard drill bit with a conical angle at its tip, and when the rotor was inserted, it was pushed into this cone and could not be

removed without enlarging the narrower part of the hole.

Possibly this issue could have been resolved by slightly widening the bore that receives the rotor in the design to make for a looser fit, but this route was not taken and the first iteration of the tool was never tested for actually packing a sample. Instead, the tool was redesigned significantly to eliminate the need for manually handling the 0.7 mm rotors by allowing the usage of the provided handling toolkit.

The main part of this kit is the rotor grabber, which has a locating section with a diameter of 13 mm. While using the full length of the locating section is not required as the front face may be used for reference, the proper diameter of the corresponding counterbore is critical for centering the rotor. Additionally, having the rotor protrude by the correct amount (2.6 mm) is important to ensure the proper function of the grabber and to allow a transfer of the rotor to other tools from the kit.

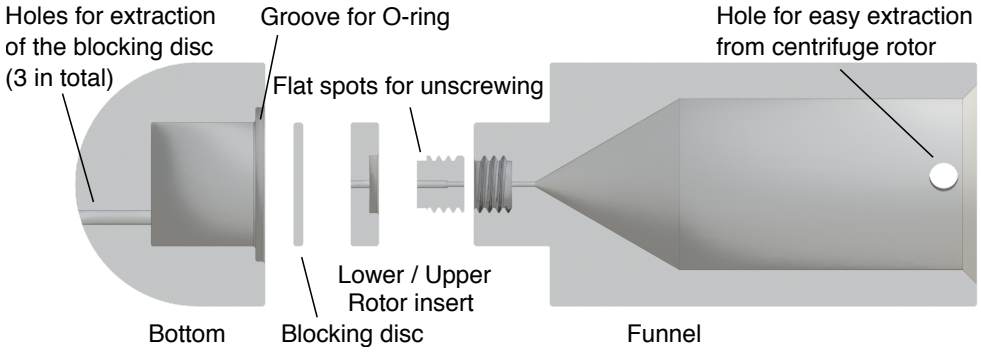

Figure 54: Rotor packing tool adapted for compatibility with the Bruker rotor grabber.

The redesigned packing tool (shown in figures 54 and 55) splits the bore that accepts the rotor into two parts (the lower and upper rotor insert), so that an inserted rotor will protrude from one of them at all times and is easier to remove than one that completely vanishes into a hole. Cleaning the tool is simplified by giving the lower rotor insert a through-hole and adding the blocking disc to stop the rotor at the bottom. Both the lower rotor insert and the blocking disc may be extracted from the tool bottom by pushing them out via a set of three holes. Because the length of the rotor is now distributed into two parts, the upper rotor insert is shorter and flats are added to simplify unscrewing it from the funnel.

Figure 55: Rotor packing tool adapted for compatibility with the Bruker rotor grabber, disassembled.

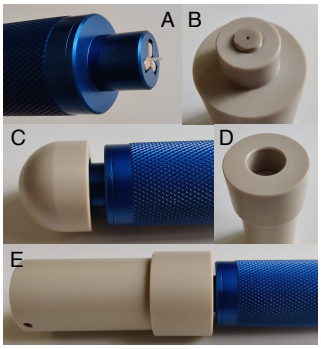

Figure 56: Usage of the packing tool with the Bruker rotor grabber. A: Placement of the rotor in the rotor grabber. B: Underside of the funnel with the upper rotor insert installed. C: Rotor grabber inserted into the bottom (after the blocking disc and lower rotor insert have been installed). D: Plastic sleeve installed on the funnel. E: Rotor grabber inserted into the plastic sleeve.

To allow the use of the rotor grabber, the diameter of the main bore in the bottom part of the tool was chosen to be 13 mm, the diameter of registering part of the grabber. In addition, a sleeve with the same inner diameter was made to fit over the assembled upper part of the tool and extract a rotor that stayed in the upper rotor insert. The handling of the tool is shown in figure 56

This tool was tested with water and found to be leaking when used in the ultracentrifuge. The exact place of the leak could not be identified at the time of writing. However, using a blocking disc manufactured of rubber instead of the hard PEEK and installing an O-ring into the groove that was already present in the first design should theoretically

eliminate all possible leaks to the outside of the tool. To ensure success, care has to be taken to choose the right thickness of sealing materials so that both seals are slightly compressed under the high acceleration in the ultracentrifuge.

Preventing leakage from the inside of the funnel and rotor to the rest of the tool is more challenging and would require a precise adjustment of the lengths of the rotor inserts with respect to the length of the rotor itself. If the rotor cavity is slightly shorter than the rotor it is meant to receive, the rotor will be clamped between the parts of the tool surrounding it, likely forming a tight seal even with the hard PEEK. Unfortunately, due to the leak and a lack of time, the usefulness of the new design could not yet be evaluated properly.

5.3 Rf coil balance measurements

In an idealized picture, the axial rf field profile of a solenoid is symmetrical about its center. However, this assumption only holds as long as the coil is resonated within a balanced rf circuit with equal capacitances at both termini of the coil[88,124]. In a real NMR probe, this is not necessarily the case, and an unbalanced coil will display an asymmetric field profile. Both cases can be examined in figure 57.

The field distributions for any condition ranging from fully balanced to fully unbalanced can be simulated relatively easily, and this was done by Ralf Haueisen (Bruker) for the 1.3 mm coil and the two extreme conditions. However, it is harder to predict which condition is actually present at a certain frequency in a given probe, as all materials present in the probe will affect the resonant circuit. For an accurate determination of the balancing, the whole probe would have to be modeled and simulated at a high resolution, which is not feasible. The influence of the exact probe construction also means that the coil balancing is likely different between any two probes.

Thus, if data on the exact distribution is needed, it needs to be determined experimentally. To achieve this, several approaches are possible:

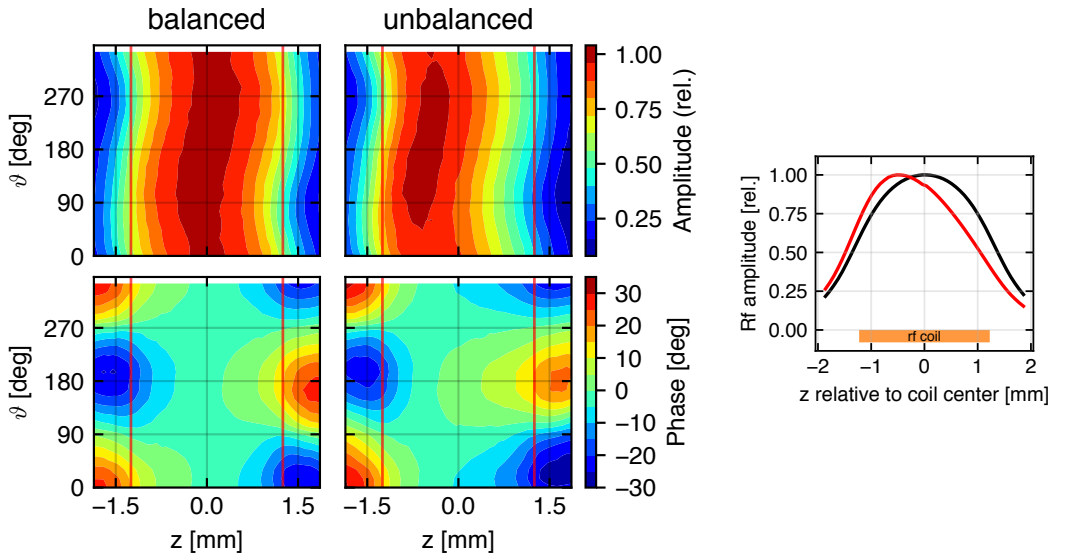

Figure 57: Left: Comparison of the rf fields generated by a fully balanced and fully unbalanced coil as a function of position along the coil axis (x axes) and azimuth (y axes) at a radial position 0.375 mm removed from the coil axis. It is clearly visible that both the rf amplitude maximum and the (coincident) "disc of smallest phase distortion" are shifted from the center of the coil in the unbalanced case. Right: Axial rf profile of a fully balanced (black) and fully unbalanced (red) coil.

1D imaging Using a gradient along the rotor axis, the rf profile can be determined by measurement of the nutation frequency as a function of the axial coordinate. However, few MAS probes, and none of our 1.3 mm probes are equipped with gradient coils, so this option could not be pursued.

Specific pulses Dissimilar rf field profiles at the involved frequencies cause a deterioration in transfer performance for the OC pulses, as shown in section 4.1.5. This may enable the determination of the actual balancing by testing OC transfer pulses optimized for a certain set of rf profiles.

Phantom samples Pursuing the same concept as the first approach, but without the capacity to image a single sample, the preparation of phantom rotors containing thin layers (or discs) of active sample precisely positioned between NMR-inactive spacers also allows the determination of the rf profile. However, this involves the fabrication of a relatively large number of phantom samples.

Tuning frequency perturbation By placing a thin disc of conductive material (e.g., copper) into the coil at varying positions, the tuning frequency of the circuit is shifted proportionally to the square of the rf amplitude at the position of the disc[88,125]. However, for this method either a set of samples needs to be prepared akin to the approach previously mentioned, or an attachment for the stator (like by Paulson et al.[88]) needs to be designed to accurately position the conductive disc within the coil. Hence, this approach was not a primary choice.

As the first approach was not accessible due to the aforementioned hardware limitations and the last two approaches were deemed mechanically challenging due to the small size of 1.3 mm rotors and the precise sample positioning required, the second option was pursued first. Informed by the designers of the probe, OC pulses for the most likely range of rf field distributions were calculated and tested experimentally.

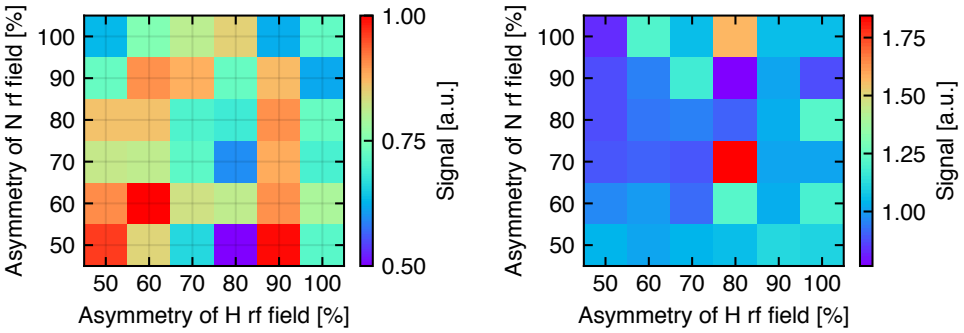

Figure 58: Performance of pulses optimized at a specific combination of rf field profiles (indicated on the x and y axes). Left panel: Without any applied normalization. Right panel: With normalization for the expected (simulated) performance.

Unfortunately, the obtained results were inconclusive regarding the actual field distribution, as no clear maximum or trend could be observed in the array of optimized pulses (see figure 58). Even after normalization of the signal amplitudes for their expected value at the respective combination of field profiles, the picture does not become clearer. Another possibility for analyzing the data would be to find the single combination of field profiles with the overall best agreement between simulated and experimental transfer efficiencies, by simulating all the generated shapes in all conceivable field profile combinations. This option was not pursued because the S/N in the data was deemed too low still.

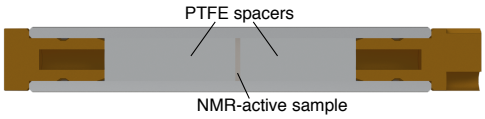

Figure 59: Cutaway view of an rf balance determination phantom sample.

It is noteworthy that there is one optimized transfer that far exceeds the expected performance, but performs relatively poorly when compared to the average of the whole set. This is likely not an indication for the agreement of the actual rf fields and the ones used during the optimization, but due to an anomaly in the optimization process, as this one transfer showed far worse simulated performance than the rest of the set.

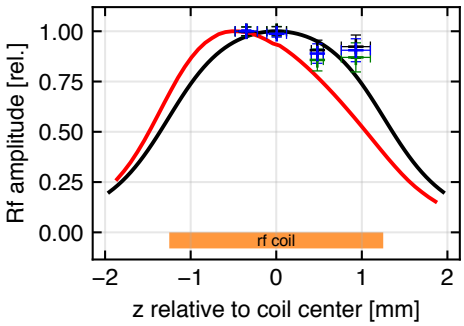

Figure 60: Measurement of the first constructed phantoms for rf field determination. Error bars designate the extent of the sample volume as determined during the assembly in the x-axis, and the linewidth at half height in the y-axis. Green markers designate the ^{1}H channel, black markers the ^{13}C channel and blue markers the ^{15}N channel. The rf profiles of a perfectly balanced (black) and a fully unbalanced (red) coil are overlaid for visual guidance.

As a consequence of the failure of this method, phantom samples were constructed using polytetrafluoroethylene (PTFE) spacers, and a small amount of uniformly labelled ^{13}C and ^{15}N-labelled glycine (^{13}C,^{15}N-Gly) to form a disc between the spacers (see figure 59). These phantoms allow the determination of ^{1}H, ^{13}C and ^{15}N nutation frequencies at the axial coordinate of the NMR-active disc. The obtained results looked more promising, but did not allow a proper determination of the field profile mainly due to inaccuracies in positioning and dimensioning the active sample layer (figure 60). However, with increases in the number of phantom samples and in precision of assembly, the determination of the actual rf profile appears to be feasible in this manner.

Once the actual rf profiles are established, the optimization of OC shapes for a given

probe will be possible. In addition, because the phantom samples are robust and not subject to deterioration, they can be given to other users in order to map their coils, and also to gather a collection of data on typical degrees of rf balancing in commercial NMR probes.

6 Summarized outlook

The prime future development based on the work presented in this thesis ought to be OC transfers that outperform the conventionally used ramp-CP. Achieving this would be the prerequisite for making the usage of the newly developed sealing plugs for the 1.3 mm rotors worthwhile, because with the ramp-CP, the additional sample volume goes largely unused. The insights gained in the process may also be useful for optimizing enhanced $H \leftrightarrow C$ transfers which suffer from similar issues at the moment (personal conversations with and tests of shapes optimized by Zdeněk Tošner). Furthermore, the sensitivity enhancement by the transverse mixing sequences would be improved as well by refined $H - N$ transfers. A prerequisite for these goals will be the accurate determination of the actual rf profiles within the coil. However, the appearance of further issues may still impede such developments.

Concerning the spin-state selective transfers, developments towards OC-derived spin state filters with improved robustness towards rf inhomogeneity are desirable, as well as transfers and filters optimized for the lower dipolar couplings present in flexible regions of proteins. Moreover, the transverse mixing approach should be extendable to this type of experiment as well, partially recovering the loss in S/N incurred by discarding the unwanted components and allowing the incorporation of the TROSY concept into higher-dimensional sensitivity-enhanced experiments.

The usage of the new sealing plugs for samples of high biological interest will require training the users in their application, because the new plugs are not as straightforward to install as the standard seals. However, since working with the 1.3 mm rotor system already requires a certain delicacy on the part of the user, this obstacle should not be insurmountable.

Finally, the 0.7 mm rotor filling tool will provide a greatly improved way to pack

samples into 0.7 mm rotors compared with the "rotor in rotor" method, once the leaks are properly sealed. As packing tools for larger rotors of various designs have been created and are commercially available, no fundamental problem should preclude this.

7 Materials and methods

7.1 Materials

7.1.1 Instruments

All NMR experiments were performed on Bruker (Billerica, USA) Avance, Avance III, Avance III HD, or Avance Neo NMR spectrometers, using Bruker room-temperature MAS probes.

7.1.2 Samples and reagents

Reagents for protein expression and purification were obtained from a variety of manufacturers and may have changed during the work presented in this thesis. Possible sources may include, but are not necessarily limited to: Carl Roth (Karlsruhe, Germany), Sigma Aldrich (St. Louis, USA), Merck (Darmstadt, Germany), Eurisotop (Saint-Aubin, France), Cambridge Isotope Laboratories (Tewksbury, Massachusetts, USA), Cortecnet (Les Ulis, France).

f-(^{13}C,^{15}N)MLF and f-(^{2}H,^{13}C,^{15}N)-MLF were obtained commercially from Giotto Biotech (Florence, Italy). ^{13}C,^{15}N-Gly was obtained commercially from Cortecnet (Les Ulis, France).

For the in-house manufacturing of the silicone sealing spacers, the silicone potting compound SYLGARD 184 (The Dow Chemical Company, Midland, USA) was used.

7.1.3 Expression of SH3 protein

Protein expression and purification was performed by Benita Koch. The chicken α-spectrin SH3 domain used in this work was expressed by in M9 minimal medium (100 % D_2O) supplemented with $^{15}NH_4Cl$ and D-Glucose-$^{13}C_6$, C-d_7. Expression was carried out overnight at 22 °C. The protein was purified via anion exchange (HiLoad 16/10 Q-Sepharose High Performance, GE Healthcare (formerly) or Cytiva Life Sciences, Marlborough, USA) and size exclusion chromatography (HiLoad 16/600 Superdex 75 pg, GE Healthcare (formerly) or Cytiva Life Sciences, Marlborough, USA) as described before[126,127]. The pure protein was lyophilized and dissolved in a mixture of H_2O and D_2O appropriate for the desired degree of backprotonation. A solution of $(NH_4)_2SO_4$ in the same mixture of H_2O and D_2O was added to reach a final concentration of 100 mM and the pH was adjusted to 8.0 by addition of NaOH/NaOD.

7.1.4 Other materials

MAS rotors manufactured by Bruker were obtained from Cortecnet (Les Ulis, France) or Bruker (Billerica, USA).

Sealing spacers from FFKM were produced by Fluorez (Taipei City, Taiwan) from two different FFKM compounds, FC750B and FU750N.

7.2 Sample preparation

Dry powder samples were prepared by tightly packing the powder into a MAS rotor after grinding it very finely in a mortar and pestle.

Protein samples were packed using filling tools for 1.3 mm Bruker rotors manufactured by Giotto Biotech. The actual filling process was conducted in an ultracentrifuge, spinning the sample into the rotor at 28 000 g for 30–60 min for microcrystalline proteins and as long as necessary for the passage through the packing tool for fibrillized proteins.

7.3 NMR simulations

Solid-state NMR simulations were performed in SIMPSON, either on a local PC using version 4.2.1, or on Leibniz Supercomputing Centre (LRZ) high performance computing (HPC) clusters using a customized version. In that version, the effect of rotationally modulated rf inhomogeneity can be taken into account in the simulation.

Spin systems for these simulations were obtained from the Protein Data Bank (PDB) structures of chicken α-spectrin SH3 (PDB code 2NUZ), ubiquitin (PDB code 1UBQ) or fMLF peptide (PDB code 1Q7O) using the VMD plugin SIMMOLvmd. The obtained dipolar coupling constants were then reduced to represent the lowering of the order parameter in slightly flexible samples such as proteins[86].

Radiofrequency field maps were created by a MATLAB script provided by Zdeněk Tošner, which implements the method described by Frank Engelke[83], or by converting full field maps calculated by Ralf Haueisen (Bruker) in a microwave simulation software (unpublished data) into the SIMPSON format using a Python script.

7.4 NMR experiments

Hard pulse and rf amplitude calibration were performed by looking for a null signal. In case of ^1H pulses, this was achieved by calibrating the duration of a 2π pulse. For ^{13}C and ^{15}N pulses, CP experiments were used, where the coherence transfer was followed by a $\pi/2$ pulse whose duration was calibrated.

For the calibration of CP transfers, array optimizations of the rf amplitudes looking for maximum signal amplitude were conducted, followed by an optimization of the contact time if necessary. Decoupling amplitudes and schemes were optimized similarly according to signal amplitude.

8 References

(1) Marion, D. (2013). An Introduction to Biological NMR Spectroscopy *. *Mol. Cell. Proteomics 12*, 3006–3025.

(2) Reif, B., Ashbrook, S. E., Emsley, L., and Hong, M. (2021). Solid-State NMR Spectroscopy. *Nat. Rev. Methods Primer 1*, 1–23.

(3) Fleming, I., and Williams, D., *Spectroscopic Methods in Organic Chemistry*; Springer International Publishing: Cham, 2019.

(4) Emwas, A.-H., Roy, R., McKay, R. T., Tenori, L., Saccenti, E., Gowda, G. A. N., Raftery, D., Alahmari, F., Jaremko, L., Jaremko, M., and Wishart, D. S. (2019). NMR Spectroscopy for Metabolomics Research. *Metabolites 9*, 123.

(5) Hatzakis, E. (2019). Nuclear Magnetic Resonance (NMR) Spectroscopy in Food Science: A Comprehensive Review. *Compr. Rev. Food Sci. Food Saf. 18*, 189–220.

(6) McBrierty, V. J. (1974). N.m.r. of Solid Polymers: A Review. *Polymer 15*, 503–520.

(7) Adams, A. (2016). Analysis of Solid Technical Polymers by Compact NMR. *TrAC Trends Anal. Chem. 83*, 107–119.

(8) Hunger, M. (2004). In Situ NMR Spectroscopy in Heterogeneous Catalysis. *Catal. Today 97*, 3–12.

(9) Blanc, F., Leskes, M., and Grey, C. P. (2013). In Situ Solid-State NMR Spectroscopy of Electrochemical Cells: Batteries, Supercapacitors, and Fuel Cells. *Acc. Chem. Res. 46*, 1952–1963.

(10) Zeeman, P. (1896). Ueber Einen Einfluss Der Magnetisirung Auf Die Natur Des von Einer Substanz Emittirten Lichtes. *Verhandlungen Phys. Ges. Zu Berl. 15*, 128–130.

(11) Purcell, E. M., Torrey, H. C., and Pound, R. V. (1946). Resonance Absorption by Nuclear Magnetic Moments in a Solid. *Phys. Rev. 69*, 37–38.

(12) Kellogg, J. M. B., Rabi, I. I., and Zacharias, J. R. (1936). The Gyromagnetic Properties of the Hydrogens. *Phys. Rev. 50*, 472–481.

(13) Rabi, I. I., Zacharias, J. R., Millman, S., and Kusch, P. (1938). A New Method of Measuring Nuclear Magnetic Moment. *Phys. Rev. 53*, 318–318.

(14) Bloch, F., Hansen, W. W., and Packard, M. (1946). Nuclear Induction. *Phys. Rev. 69*, 127–127.

(15) Bloch, F. (1946). Nuclear Induction. *Phys. Rev. 70*, 460–474.

(16) Hahn, E. L. (1950). Nuclear Induction Due to Free Larmor Precession. *Phys. Rev. 77*, 297–298.

(17) Knight, W. D. (1949). Nuclear Magnetic Resonance Shift in Metals. *Phys. Rev. 76*, 1259–1260.

(18) Gutowsky, H. S., and Hoffman, C. J. (1950). Chemical Shifts in the Magnetic Resonance of F19. *Phys. Rev. 80*, 110–111.

(19) Proctor, W. G., and Yu, F. C. (1950). The Dependence of a Nuclear Magnetic Resonance Frequency upon Chemical Compound. *Phys. Rev. 77*, 717–717.

(20) Wertz, J. E. (1955). Nuclear And Electronic Spin Magnetic Resonance. *Chem. Rev. 55*, 829–955.

(21) Proctor, W. G., and Yu, F. C. (1951). On the Nuclear Magnetic Moments of Several Stable Isotopes. *Phys. Rev. 81*, 20–30.

(22) Gutowsky, H. S., and McCall, D. W. (1951). Nuclear Magnetic Resonance Fine Structure in Liquids. *Phys. Rev. 82*, 748–749.

(23) Gutowsky, H. S., McCall, D. W., and Slichter, C. P. (1951). Coupling among Nuclear Magnetic Dipoles in Molecules. *Phys. Rev. 84*, 589–590.

(24) Ramsey, N. F., and Purcell, E. M. (1952). Interactions between Nuclear Spins in Molecules. *Phys. Rev. 85*, 143–144.

(25) Levitt, M. H., *Spin Dynamics: Basics of Nuclear Magnetic Resonance*, 2nd ed; John Wiley & Sons: Chichester, England ; Hoboken, NJ, 2008; 714 pp.

(26) Haeberlen, U. In *Advances in Magnetic Resonance*, 1st ed.; Elsevier Science: Saint Louis, 1976.

(27) Bak, M., Rasmussen, J. T., and Nielsen, N. C. (2000). SIMPSON: A General Simulation Program for Solid-State NMR Spectroscopy. *J. Magn. Reson. 147*, 296–330.

(28) Tošner, Z., Vosegaard, T., Kehlet, C., Khaneja, N., Glaser, S. J., and Nielsen, N. C. (2009). Optimal Control in NMR Spectroscopy: Numerical Implementation in SIMPSON. *J. Magn. Reson. 197*, 120–134.

(29) Tošner, Z., Andersen, R., Stevensson, B., Edén, M., Nielsen, N. C., and Vosegaard, T. (2014). Computer-Intensive Simulation of Solid-State NMR Experiments Using SIMPSON. *J. Magn. Reson. 246*, 79–93.

(30) Pake, G. E. (1948). Nuclear Resonance Absorption in Hydrated Crystals: Fine Structure of the Proton Line. *J. Chem. Phys. 16*, 327–336.

(31) Bielecki, A., and Pines, A. (1987). Pake Patterns from Zero to High Field. *J. Magn. Reson. 1969 74*, 381–385.

(32) Andrew, E. R., Bradbury, A., and Eades, R. G. (1959). Removal of Dipolar Broadening of Nuclear Magnetic Resonance Spectra of Solids by Specimen Rotation. *Nature 183*, 1802–1803.

(33) Lowe, I. J. (1959). Free Induction Decays of Rotating Solids. *Phys. Rev. Lett. 2*, 285–287.

(34) Andrew, E. R., Wynn, V. T., and Eley, D. D. (1966). Solid-State 31P Magnetic Resonance Shifts and Fine Structure. *Proc. R. Soc. Lond. Ser. Math. Phys. Sci. 291*, 257–266.

(35) Mehring, M., *Principles of High Resolution NMR in Solids*, 2nd ed.; NMR - Basic Principles and Progress, Vol. 11; Springer Berlin, Heidelberg: Heidelberg, 1983; VIII, 344.

(36) Morris, G. A., and Freeman, R. (1979). Enhancement of Nuclear Magnetic Resonance Signals by Polarization Transfer. *J. Am. Chem. Soc.*, 3.

(37) Burum, D. P., and Ernst, R. R. (1980). Net Polarization Transfer via a J-ordered State for Signal Enhancement of Low-Sensitivity Nuclei. *Journal of Magnetic Resonance (1969) 39*, 163–168.

(38) Hartmann, S. R., and Hahn, E. L. (1962). Nuclear Double Resonance in the Rotating Frame. *Phys. Rev. 128*, 2042–2053.

(39) Pines, A., Gibby, M. G., and Waugh, J. S. (1973). Proton-enhanced NMR of Dilute Spins in Solids. *J. Chem. Phys. 59*, 569–590.

(40) Schmidt-Rohr, K., and Spiess, H. W., *Multidimensional Solid-State NMR and Polymers*; Academic Press: London, 1994; 486 pp.

(41) Stejskal, E. O., Schaefer, J., and Waugh, J. S. (1977). Magic-Angle Spinning and Polarization Transfer in Proton-Enhanced NMR. *J. Magn. Reson. 1969 28*, 105–112.

(42) Nielsen, N. C., Bildsøe, H., Jakobsen, H. J., and Levitt, M. H. (1994). Double-quantum Homonuclear Rotary Resonance: Efficient Dipolar Recovery in Magic-angle Spinning Nuclear Magnetic Resonance. *J. Chem. Phys. 101*, 1805–1812.

(43) Peersen, O., Wu, X., Kustanovich, I., and Smith, S. (1993). Variable-Amplitude Cross-Polarization MAS NMR. *J. Magn. Reson. A 104*, 334–339.

(44) Metz, G., Wu, X., and Smith, S. (1994). Ramped-Amplitude Cross Polarization in Magic-Angle-Spinning NMR. *J. Magn. Reson. A 110*, 219–227.

(45) Hediger, S., Meier, B., Kurur, N. D., Bodenhausen, G., and Ernst, R. (1994). NMR Cross Polarization by Adiabatic Passage through the Hartmann—Hahn Condition (APHH). *Chem. Phys. Lett. 223*, 283–288.

(46) Hediger, S., Meier, B., and Ernst, R. (1995). Adiabatic Passage Hartmann-Hahn Cross Polarization in NMR under Magic Angle Sample Spinning. *Chem. Phys. Lett. 240*, 449–456.

(47) Barbet-Massin, E. et al. (2014). Rapid Proton-Detected NMR Assignment for Proteins with Fast Magic Angle Spinning. *J. Am. Chem. Soc. 136*, 12489–12497.

(48) Aue, W. P., Bartholdi, E., and Ernst, R. R. (1976). Two-dimensional Spectroscopy. Application to Nuclear Magnetic Resonance. *J. Chem. Phys. 64*, 2229–2246.

(49) Kolar, P., Grbić, M. S., and Hrabar, S. (2019). Sensitivity Enhancement of NMR Spectroscopy Receiving Chain Used in Condensed Matter Physics. *Sensors 19*, 3064.

(50) Samoson, A. (2019). H-MAS. *J. Magn. Reson. 306*, 167–172.

(51) Wilhelm, D., Purea, A., and Engelke, F. (2015). Fluid Flow Dynamics in MAS Systems. *J. Magn. Reson. 257*, 51–63.

(52) Tošner, Z., Purea, A., Struppe, J. O., Wegner, S., Engelke, F., Glaser, S. J., and Reif, B. (2017). Radiofrequency Fields in MAS Solid State NMR Probes. *J. Magn. Reson. 284*, 20–32.

(53) Tošner, Z., Sarkar, R., Becker-Baldus, J., Glaubitz, C., Wegner, S., Engelke, F., Glaser, S. J., and Reif, B. (2018). Overcoming Volume Selectivity of Dipolar Recoupling in Biological Solid-State NMR Spectroscopy. *Angew. Chem. Int. Ed. 57*, 14514–14518.

(54) Pontryagin, L. S., Boltyanskii, V. G., Gamkrelidze, R. V., and Mishchenko, E. F., The Mathematical Theory of Optimal Processes, 4 vols.; L. S. Pontryagin Selected Works, Vol. 4; Wiley-Interscience: New York, 1962.

(55) Bellman, R. (1952). On the Theory of Dynamic Programming. *Proc. Natl. Acad. Sci. 38*, 716–719.

(56) Bellman, R. (1954). Dynamic Programming and a New Formalism in the Calculus of Variations. *Proc. Natl. Acad. Sci. 40*, 231–235.

(57) Conolly, S., Nishimura, D., and Macovski, A. (1986). Optimal Control Solutions to the Magnetic Resonance Selective Excitation Problem. *IEEE Trans. Med. Imaging 5*, 106–115.

(58) Mao, J., Mareci, T. H., Scott, K. N., and Andrew, E. R. (1986). Selective Inversion Radiofrequency Pulses by Optimal Control. *J. Magn. Reson. 1969 70*, 310–318.

(59) Rosenfeld, D., and Zur, Y. (1996). Design of Adiabatic Selective Pulses Using Optimal Control Theory. *Magn. Reson. Med. 36*, 401–409.

(60) Xu, D., King, K. F., Zhu, Y., McKinnon, G. C., and Liang, Z.-P. (2008). Designing Multichannel, Multidimensional, Arbitrary Flip Angle RF Pulses Using an Optimal Control Approach. *Magn. Reson. Med. 59*, 547–560.

(61) Bonnard, B., Cots, O., Glaser, S. J., Lapert, M., Sugny, D., and Zhang, Y. (2012). Geometric Optimal Control of the Contrast Imaging Problem in Nuclear Magnetic Resonance. *IEEE Trans. Autom. Control 57*, 1957–1969.

(62) Lapert, M., Zhang, Y., Janich, M. A., Glaser, S. J., and Sugny, D. (2012). Exploring the Physical Limits of Saturation Contrast in Magnetic Resonance Imaging. *Sci. Rep. 2*, 589.

(63) Van Reeth, E., Ratiney, H., Lapert, M., Glaser, S. J., and Sugny, D. (2017). Optimal Control Theory for Applications in Magnetic Resonance Imaging. *Pac. J. Math. Ind. 9*, 9.

(64) Khaneja, N., Reiss, T., Luy, B., and Glaser, S. J. (2003). Optimal Control of Spin Dynamics in the Presence of Relaxation. *J. Magn. Reson. 162*, 311–319.

(65) Skinner, T. E., Reiss, T. O., Luy, B., Khaneja, N., and Glaser, S. J. (2003). Application of Optimal Control Theory to the Design of Broadband Excitation Pulses for High-Resolution NMR. *J. Magn. Reson. 163*, 8–15.

(66) Khaneja, N., Reiss, T., Kehlet, C., Schulte-Herbrüggen, T., and Glaser, S. J. (2005). Optimal Control of Coupled Spin Dynamics: Design of NMR Pulse Sequences by Gradient Ascent Algorithms. *J. Magn. Reson. 172*, 296–305.

(67) Frueh, D. P., Ito, T., Li, J.-S., Wagner, G., Glaser, S. J., and Khaneja, N. (2005). Sensitivity Enhancement in NMR of Macromolecules by Application of Optimal Control Theory. *J. Biomol. NMR 32*, 23–30.

(68) Skinner, T. E., Kobzar, K., Luy, B., Bendall, M. R., Bermel, W., Khaneja, N., and Glaser, S. J. (2006). Optimal Control Design of Constant Amplitude Phase-Modulated Pulses: Application to Calibration-Free Broadband Excitation. *J. Magn. Reson. 179*, 241–249.

(69) Gershenzon, N. I., Kobzar, K., Luy, B., Glaser, S. J., and Skinner, T. E. (2007). Optimal Control Design of Excitation Pulses That Accommodate Relaxation. *J. Magn. Reson. 188*, 330–336.

(70) Skinner, T. E., Gershenzon, N. I., Nimbalkar, M., and Glaser, S. J. (2012). Optimal Control Design of Band-Selective Excitation Pulses That Accommodate Relaxation and RF Inhomogeneity. *J. Magn. Reson. 217*, 53–60.

(71) Kallies, W., and Glaser, S. J. (2018). Cooperative Broadband Spin Echoes through Optimal Control. *J. Magn. Reson. 286*, 115–137.

(72) Asami, S., Kallies, W., Günther, J. C., Stavropoulou, M., Glaser, S. J., and Sattler, M. (2018). Ultrashort Broadband Cooperative Pulses for Multidimensional Biomolecular NMR Experiments. *Angew. Chem. - Int. Ed. 57*, 14498–14502.

(73) Kehlet, C. T., Sivertsen, A. C., Bjerring, M., Reiss, T. O., Khaneja, N., Glaser, S. J., and Nielsen, N. C. (2004). Improving Solid-State NMR Dipolar Recoupling by Optimal Control. *J. Am. Chem. Soc. 126*, 10202–10203.

(74) Tošner, Z., Glaser, S. J., Khaneja, N., and Nielsen, N. C. (2006). Effective Hamiltonians by Optimal Control: Solid-state NMR Double-Quantum Planar and Isotropic Dipolar Recoupling. *J. Chem. Phys. 125*, 184502.

(75) Kehlet, C., Bjerring, M., Sivertsen, A. C., Kristensen, T., Enghild, J. J., Glaser, S. J., Khaneja, N., and Nielsen, N. C. (2007). Optimal Control Based NCO and NCA Experiments for Spectral Assignment in Biological Solid-State NMR Spectroscopy. *J. Magn. Reson. 188*, 216–230.

(76) Nielsen, A. B., Bjerring, M., Nielsen, J. T., and Nielsen, N. C. (2009). Symmetry-Based Dipolar Recoupling by Optimal Control: Band-selective Experiments for Assignment of Solid-State NMR Spectra of Proteins. *J. Chem. Phys. 131*, 025101.

(77) Kehlet, C., Nielsen, J. T., Tosner, Z., and Nielsen, N. C. (2011). Resolution-Enhanced Solid-State NMR 13C-13C Correlation Spectroscopy by Optimal Control Dipolar-Driven Spin-State-Selective Coherence Transfer. *J. Phys. Chem. Lett. 2*, 543–547.

(78) Tošner, Z., Brandl, M. J., Blahut, J., Glaser, S. J., and Reif, B. (2021). Maximizing Efficiency of Dipolar Recoupling in Solid-State NMR Using Optimal Control Sequences. *Sci. Adv. 7*, eabj5913.

(79) Hogben, H., Krzystyniak, M., Charnock, G., Hore, P., and Kuprov, I. (2011). Spinach – A Software Library for Simulation of Spin Dynamics in Large Spin Systems. *J. Magn. Reson. 208*, 179–194.

(80) Idziak, S., and Haeberlen, U. (1982). Design and Construction of a High Homogeneity Rf Coil for Solid-State Multiple-Pulse NMR. *J. Magn. Reson. 1969 50*, 281–288.

(81) Privalov, A., Dvinskikh, S., and Vieth, H.-M. (1996). Coil Design for Large-Volume High-B1 Homogeneity for Solid-State NMR Applications. *J. Magn. Reson. A 123*, 157–160.

(82) Rosay, M., Blank, M., and Engelke, F. (2016). Instrumentation for Solid-State Dynamic Nuclear Polarization with Magic Angle Spinning NMR. *J. Magn. Reson. 264*, 88–98.

(83) Engelke, F. (2002). Electromagnetic Wave Compression and Radio Frequency Homogeneity in NMR Solenoidal Coils: Computational Approach. *Concepts Magn. Reson. Part B Magn. Reson. Eng. 15*, 129–155.

(84) Aebischer, K., Tošner, Z., and Ernst, M. (2021). Effects of Radial Radio-Frequency Field Inhomogeneity on MAS Solid-State NMR Experiments. *Magn. Reson. 2*, 523–543.

(85) Köcher, S., Heydenreich, T., and Glaser, S. (2014). Visualization and Analysis of Modulated Pulses in Magnetic Resonance by Joint Time–Frequency Representations. *J. Magn. Reson. 249*, 63–71.

(86) Chevelkov, V., Fink, U., and Reif, B. (2009). Accurate Determination of Order Parameters from 1 H, 15 N Dipolar Couplings in MAS Solid-State NMR Experiments. *J. Am. Chem. Soc. 131*, 14018–14022.

(87) Bak, M., and Nielsen, N. C. (1997). REPULSION, A Novel Approach to Efficient Powder Averaging in Solid-State NMR. *J. Magn. Reson. 125*, 132–139.

(88) Paulson, E. K., Martin, R. W., and Zilm, K. W. (2004). Cross Polarization, Radio Frequency Field Homogeneity, and Circuit Balancing in High Field Solid State NMR Probes. *J. Magn. Reson. 171*, 314–323.

(89) Vega, A. J. (2004). Controlling the Effects of Pulse Transients and RF Inhomogeneity in Phase-Modulated Multiple-Pulse Sequences for Homonuclear Decoupling in Solid-State Proton NMR. *J. Magn. Reson. 170*, 22–41.

(90) Wittmann, J. J., Takeda, K., Meier, B. H., and Ernst, M. (2015). Compensating Pulse Imperfections in Solid-State NMR Spectroscopy: A Key to Better Reproducibility and Performance. *Angew. Chem. Int. Ed. 54*, 12592–12596.

(91) Wittmann, J. J., Mertens, V., Takeda, K., Meier, B. H., and Ernst, M. (2016). Quantification and Compensation of the Influence of Pulse Transients on Symmetry-Based Recoupling Sequences. *J. Magn. Reson. 263*, 7–18.

(92) Hellwagner, J., Sharma, K., Tan, K. O., Wittmann, J. J., Meier, B. H., Madhu, P. K., and Ernst, M. (2017). Optimizing Symmetry-Based Recoupling Sequences in Solid-State NMR by Pulse-Transient Compensation and Asynchronous Implementation. *J. Chem. Phys. 146*, 244202.

(93) Hellwagner, J., Wili, N., Ibáñez, L. F., Wittmann, J. J., Meier, B. H., and Ernst, M. (2018). Transient Effects in π-Pulse Sequences in MAS Solid-State NMR. *J. Magn. Reson. 287*, 65–73.

(94) Cavanagh, J., Fairbrother, W. J., Palmer, A. G., Rance, M., and Skelton, N. J., *Protein NMR Spectroscopy: Principles and Practice*, 2nd ed; Academic Press: Amsterdam ; Boston, 2007; 885 pp.

(95) Cavanagh, J., and Rance, M. In *Annual Reports on NMR Spectroscopy*, Webb, G. A., Ed.; Academic Press: 1993; Vol. 27, pp 1–58.

(96) Schleucher, J., Sattler, M., and Griesinger, C. (1993). Coherence Selection by Gradients without Signal Attenuation: Application to the Three-Dimensional HNCO Experiment. *Angew. Chem. Int. Ed. Engl. 32*, 1489–1491.

(97) States, D. J., Haberkorn, R. A., and Ruben, D. J. (1982). A Two-Dimensional Nuclear Overhauser Experiment with Pure Absorption Phase in Four Quadrants. *J. Magn. Reson. 1969 48*, 286–292.

(98) Palmer, A. G., Cavanagh, J., Wright, P. E., and Rance, M. (1991). Sensitivity Improvement in Proton-Detected Two-Dimensional Heteronuclear Correlation NMR Spectroscopy. *J. Magn. Reson. 1969 93*, 151–170.

(99) Sattler, M., Schwendinger, M. G., Schleucher, J., and Griesinger, C. (1995). Novel Strategies for Sensitivity Enhancement in Heteronuclear Multi-Dimensional NMR Experiments Employing Pulsed Field Gradients. *J. Biomol. NMR 6*, 11–22.

(100) Tycko, R. (2004). Sensitivity Enhancement in Two-Dimensional Solid-State NMR Spectroscopy by Transverse Mixing. *ChemPhysChem 5*, 863–868.

(101) Khaneja, N. (2006). Sensitivity Enhanced Recoupling Experiments in Solid-State NMR by γ Preparation. *J. Magn. Reson. 183*, 242–251.

(102) Gopinath, T., and Veglia, G. (2009). Sensitivity Enhancement in Static Solid-State NMR Experiments via Single- and Multiple-Quantum Dipolar Coherences. *J. Am. Chem. Soc. 131*, 5754–5756.

(103) Gopinath, T., Mote, K. R., and Veglia, G. (2013). Sensitivity and Resolution Enhancement of Oriented Solid-State NMR: Application to Membrane Proteins. *Prog. Nucl. Magn. Reson. Spectrosc. 75*, 50–68.

(104) Riek, R., Pervushin, K., and Wüthrich, K. (2000). TROSY and CRINEPT: NMR with Large Molecular and Supramolecular Structures in Solution. *Trends Biochem. Sci. 25*, 462–468.

(105) Xu, Y., and Matthews, S. In *Modern NMR Methodology*, Heise, H., and Matthews, S., Eds.; Topics in Current Chemistry; Springer: Berlin, Heidelberg, 2013, pp 97–119.

(106) Chevelkov, V., Faelber, K., Schrey, A., Rehbein, K., Diehl, A., and Reif, B. (2007). Differential Line Broadening in MAS Solid-State NMR Due to Dynamic Interference. *J. Am. Chem. Soc. 129*, 10195–10200.

(107) Linser, R., Fink, U., and Reif, B. (2010). Assignment of Dynamic Regions in Biological Solids Enabled by Spin-State Selective NMR Experiments. *J. Am. Chem. Soc. 132*, 8891–8893.

(108) Vold, R. L., and Vold, R. R. (1978). Nuclear Magnetic Relaxation in Coupled Spin Systems. *Prog. Nucl. Magn. Reson. Spectrosc. 12*, 79–133.

(109) Guéron, M., Leroy, J. L., and Griffey, R. H. (1983). Proton Nuclear Magnetic Relaxation of Nitrogen-15-Labeled Nucleic Acids via Dipolar Coupling and Chemical Shift Anisotropy. *J. Am. Chem. Soc. 105*, 7262–7266.

(110) Pervushin, K., Riek, R., Wider, G., and Wuthrich, K. (1997). Attenuated T2 Relaxation by Mutual Cancellation of Dipole-Dipole Coupling and Chemical Shift Anisotropy Indicates an Avenue to NMR Structures of Very Large Biological Macromolecules in Solution. *Proc. Natl. Acad. Sci. 94*, 12366–12371.

(111) Pervushin, K. V., Wider, G., and Wüthrich, K. (1998). Single Transition-to-Single Transition Polarization Transfer (ST2-PT) in [15N,1H]-TROSY. *J. Biomol. NMR 12*, 345–348.

(112) Sarkar, R., Rodriguez Camargo, D. C., Pintacuda, G., and Reif, B. (2015). Restoring Resolution in Biological Solid-State NMR under Conditions of Off-Magic-Angle Spinning. *J. Phys. Chem. Lett. 6*, 5040–5044.

(113) Penzel, S., Smith, A. A., Ernst, M., and Meier, B. H. (2018). Setting the Magic Angle for Fast Magic-Angle Spinning Probes. *J. Magn. Reson. 293*, 115–122.

(114) Takeuchi, K., Arthanari, H., and Wagner, G. (2016). Perspective: Revisiting the Field Dependence of TROSY Sensitivity. *J. Biomol. NMR 66*, 221–225.

(115) Levitt, M. H. (1997). The Signs of Frequencies and Phases in NMR. *J. Magn. Reson. 126*, 164–182.

(116) Hing, A. W., Vega, S., and Schaefer, J. (1992). Transferred-Echo Double-Resonance NMR. *J. Magn. Reson. 1969 96*, 205–209.

(117) Böckmann, A., Gardiennet, C., Verel, R., Hunkeler, A., Loquet, A., Pintacuda, G., Emsley, L., Meier, B. H., and Lesage, A. (2009). Characterization of Different Water Pools in Solid-State NMR Protein Samples. *J. Biomol. NMR 45*, 319.

(118) Bertini, I., Engelke, F., Luchinat, C., Parigi, G., Ravera, E., Rosa, C., and Turano, P. (2012). NMR Properties of Sedimented Solutes. *Phys. Chem. Chem. Phys. 14*, 439–447.

(119) Bertini, I., Engelke, F., Gonnelli, L., Knott, B., Luchinat, C., Osen, D., and Ravera, E. (2012). On the Use of Ultracentrifugal Devices for Sedimented Solute NMR. *J. Biomol. NMR 54*, 123–127.

(120) Gardiennet, C., Schütz, A. K., Hunkeler, A., Kunert, B., Terradot, L., Böckmann, A., and Meier, B. H. (2012). A Sedimented Sample of a 59 kDa Dodecameric Helicase Yields High-Resolution Solid-State NMR Spectra. *Angew. Chem. Int. Ed. 51*, 7855–7858.

(121) Mandal, A., Boatz, J. C., Wheeler, T. B., and van der Wel, P. C. A. (2017). On the Use of Ultracentrifugal Devices for Routine Sample Preparation in Biomolecular Magic-Angle-Spinning NMR. *J. Biomol. NMR 67*, 165–178.

(122) Bertini, I., Luchinat, C., Parigi, G., Ravera, E., Reif, B., and Turano, P. (2011). Solid-State NMR of Proteins Sedimented by Ultracentrifugation. *Proc. Natl. Acad. Sci. 108*, 10396–10399.

(123) Stevens, R. A. The Development of Solid-State NMR Methodology to Study the Dynamics of Proteins and Ice, Ph.D. Thesis, Warwick: University of Warwick, 2018, 246 pp.

(124) Martin, R. W., Paulson, E. K., and Zilm, K. W. (2003). Design of a Triple Resonance Magic Angle Sample Spinning Probe for High Field Solid State Nuclear Magnetic Resonance. *Rev. Sci. Instrum. 74*, 3045–3061.

(125) Ginzton, E. L. In *Microwave Measurements*; McGraw-Hill: 1957, pp 435–461.

(126) Pauli, J., van Rossum, B., Förster, H., de Groot, H. J. M., and Oschkinat, H. (2000). Sample Optimization and Identification of Signal Patterns of Amino Acid Side Chains in 2D RFDR Spectra of the α-Spectrin SH3 Domain. *J. Magn. Reson. 143*, 411–416.

(127) Chevelkov, V., Rehbein, K., Diehl, A., and Reif, B. (2006). Ultrahigh Resolution in Proton Solid-State NMR Spectroscopy at High Levels of Deuteration. *Angew. Chem. Int. Ed. 45*, 3878–3881.

A Additional figures

A.1 H-N transfers: Detailed top curves for first generation optimizations

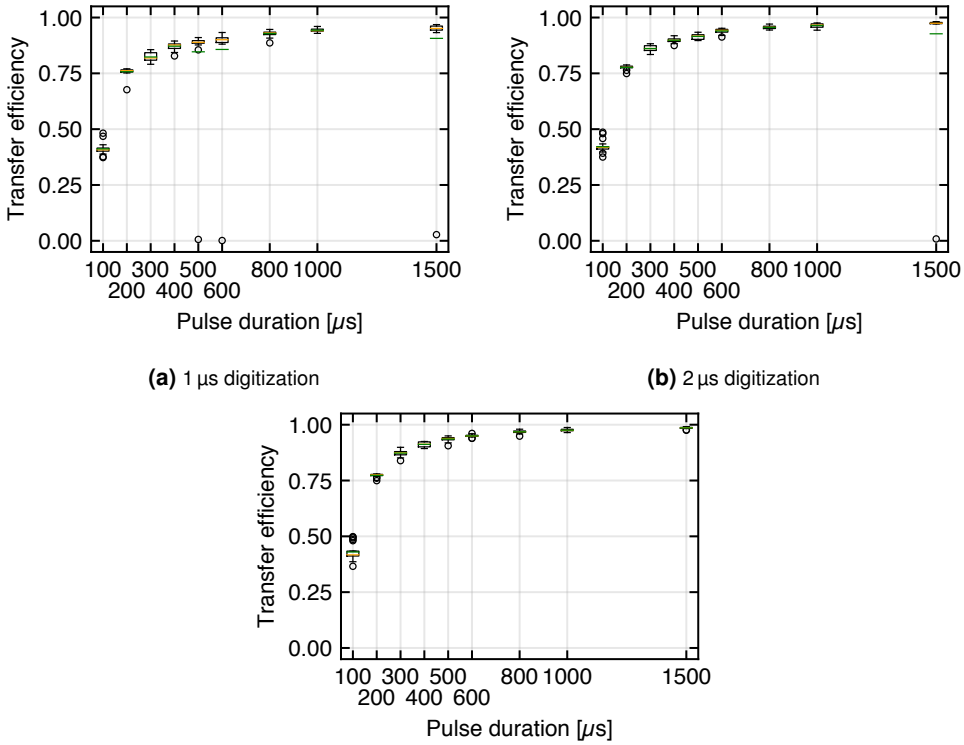

(a) 1 µs digitization

(b) 2 µs digitization

(c) 4 µs digitization

Figure A.1: Top curves for basic $H_x - N_x$ state-to-state transfer optimizations. Boxes range from the first to the third quartile, whisker length is 1.5-times the interquartile range, circles indicate fliers. Green bars indicate the median and orange bars indicate the mean of the data for each duration.

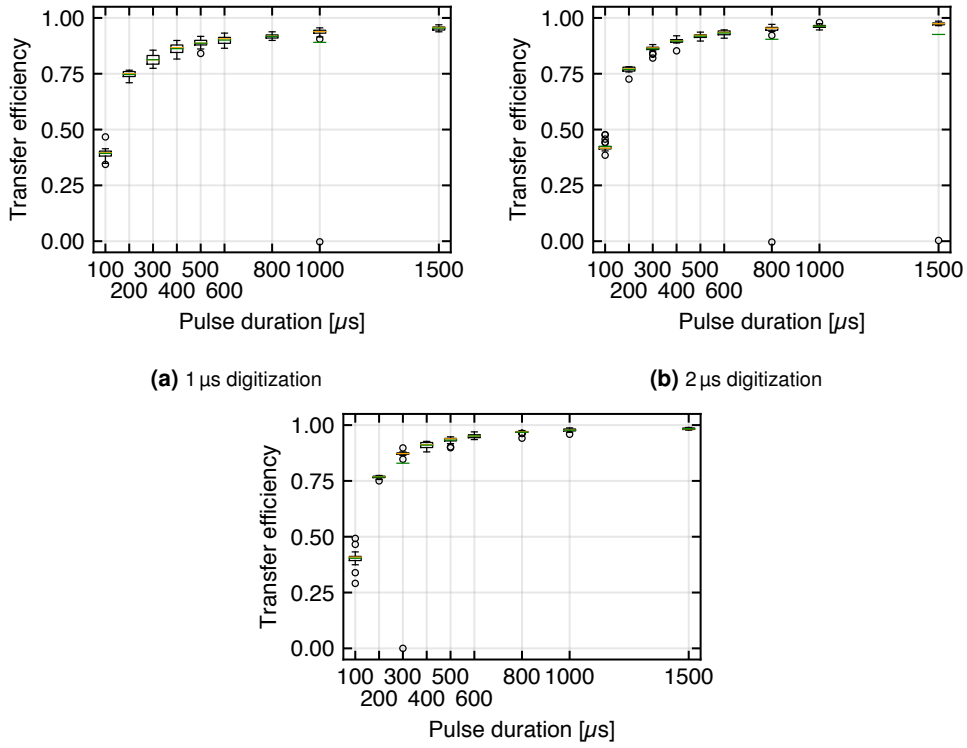

(a) 1 µs digitization

(b) 2 µs digitization

(c) 4 µs digitization

Figure A.2: Top curves for basic $H_z - N_x$ state-to-state transfer optimizations. Boxes range from the first to the third quartile, whisker length is 1.5-times the interquartile range, circles indicate fliers. Green bars indicate the median and orange bars indicate the mean of the data for each duration.

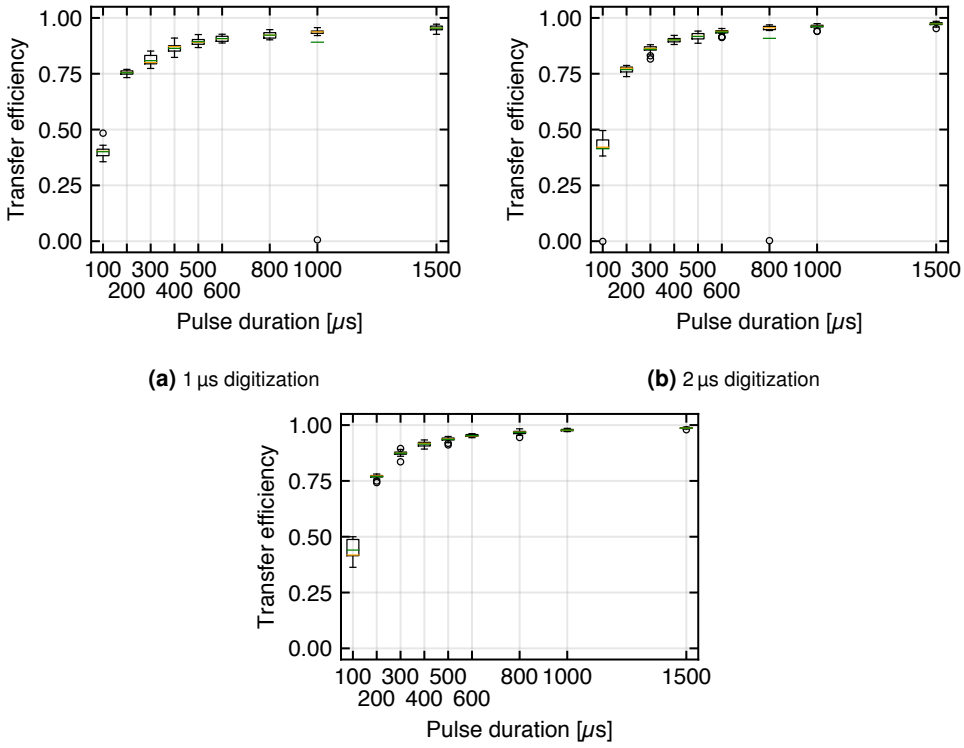

(a) 1 µs digitization

(b) 2 µs digitization

(c) 4 µs digitization

Figure A.3: Top curves for basic $N_x - H_x$ state-to-state transfer optimizations. Boxes range from the first to the third quartile, whisker length is 1.5-times the interquartile range, circles indicate fliers. Green bars indicate the median and orange bars indicate the mean of the data for each duration.

A.2 H-N transfers: Detailed top curves for shapes composed of repetitive elements

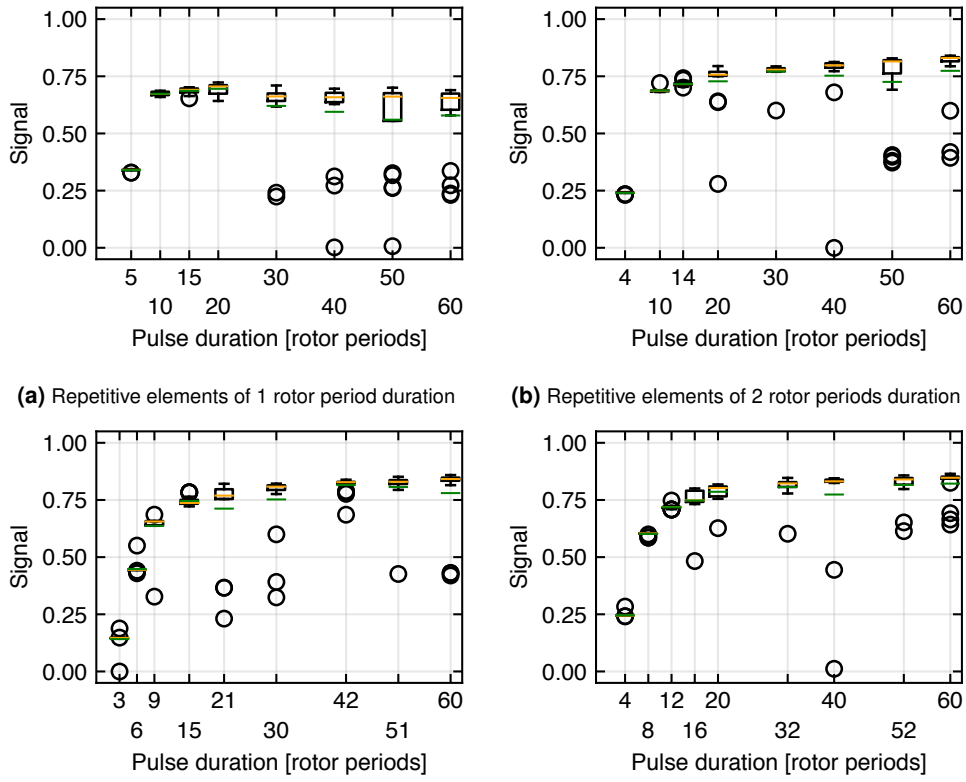

(a) Repetitive elements of 1 rotor period duration

(b) Repetitive elements of 2 rotor periods duration

(c) Repetitive elements of 3 rotor periods duration

(d) Repetitive elements of 4 rotor periods duration

Figure A.4: Top curves for $H_x - N_x$ state-to-state transfer optimizations of pulses composed of repetitive elements. Boxes range from the first to the third quartile, whisker length is 1.5-times the interquartile range, circles indicate fliers. Green bars indicate the median and orange bars indicate the mean of the data for each duration.

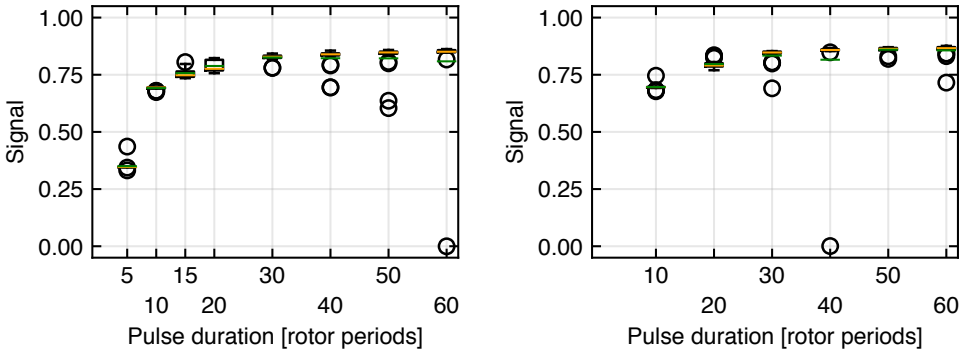

(e) Repetitive elements of 5 rotor periods duration

(f) Repetitive elements of 10 rotor periods duration

Figure A.4: Top curves for $H_x - N_x$ state-to-state transfer optimizations of pulses composed of repetitive elements (cont.).

A.3 Drawing of the rotor packing tool

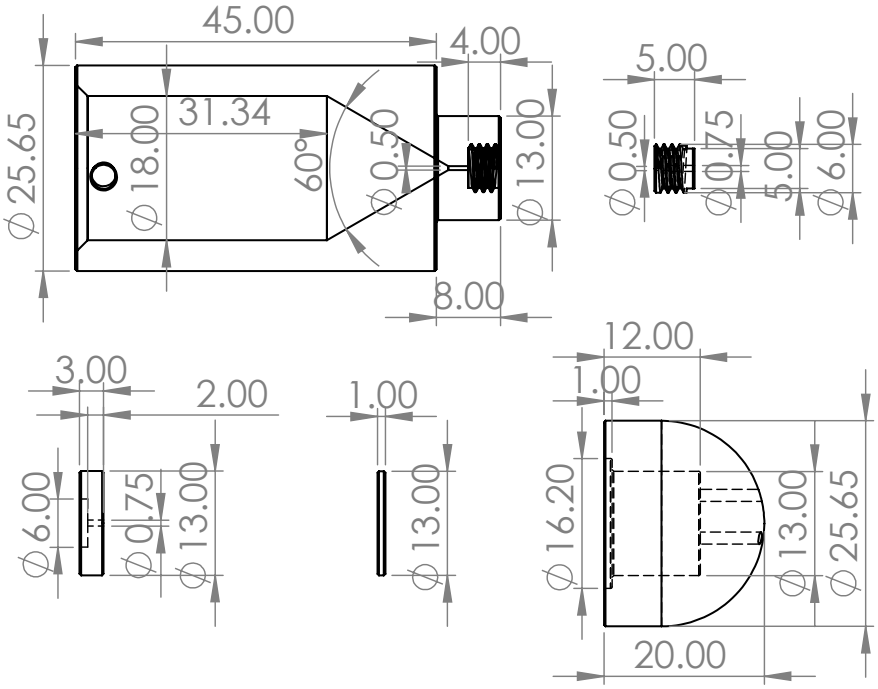

Figure A.5: Technical drawing of the rotor packing tool designed for use with the Bruker rotor handling toolkit.

B Examples of complete SIMPSON input files

B.1 Input file for basic transfer optimization

Based on code from Zdeněk Tošner.

```
spinsys {
# NH pair from ubiquitin structure
    channels 1H 15N
    nuclei   1H 15N
    shift 1 0p 7.7p 0.65 112.6 134.15 73.352
    shift 2 0p 99p 0.19 -48.529 62.139 160.36
    dipole 1 2 10400 0 106.01 -32.815
    jcoupling 1 2 -92 0 0 0 0 0
}

par {
    method   direct dsyev
    spin_rate 55000
    crystal_file rep3_112.cry
    gamma_angles 1
    variable Nspins 2
    variable recalc pow(2,2-Nspins)
    variable lam   2.0e-9

    start_operator       I1x
    detect_operator      I2x
    proton_frequency     800e6
    sw                   1e6

    # Parallelization is done via MPI, num_cores per thread therefore 1
    num_cores 1

    oc_grad_level 2
```

```
    oc_var_save_iter 2
    oc_var_save_proc rfstore

    # This MUST be used when working with optimal control!
    conjugate_fid false
}

proc rfstore {} {
# Storage of intermediate pulses during the optimization process
    global par rfsh1 rfsh2 optname itercount fout tfcomponents

    incr itercount $par(oc_var_save_iter)
    save_shape $rfsh1 $optname\_H_temp_$itercount.dat
    save_shape $rfsh2 $optname\_N_temp_$itercount.dat
    set a [lindex $tfcomponents 0]
    set b [lindex $tfcomponents 1]
    puts $fout "Iter␣$itercount␣:␣$a␣-␣$b␣=␣[expr␣$a␣-␣$b]"
    flush $fout
}

proc pulseq_OC {} {
# Optimization without 3D rf inhomogeneity
    global par rfsh1 rfsh2

    maxdt 1
    reset
    pulse_shaped $par(duration) $rfsh1 $rfsh2
    oc_acq_hermit
}

proc pulseq_OC_rotmod {} {
# Optimization with 3D rf inhomogeneity
    global par rfsh1 rfsh2

    maxdt 1
    reset
    pulse_shaped_rotormodulated $par(duration) $rfsh1 $rfsh2
    oc_acq_hermit
}

proc gradient {} {
    global par rfsh1 rfsh2  tfcomponents
```

```
    # FID length needs to be equal to number of optimized variables
    set par(np) [expr 2*$par(Norig) ]
    set f [fsimpson]
    fscale $f -scale $par(recalc)
    oc_grad_add_energy_penalty $f $rfsh1 -$par(lam) $rfsh2 -$par(lam)
    set en1 [shape_energy $rfsh1 $par(duration)]
    set en2 [shape_energy $rfsh2 $par(duration)]
    set tfcomponents [list [expr $par(_phivals_)*$par(recalc)] [expr
        $par(lam)*($en1+$en2)] ]
    return $f
}

proc target_function {} {
    global par rfsh1 rfsh2

    set par(np) 1
    set f [fsimpson]
    set Res [expr [findex $f 1 -re]*$par(recalc) ]
    funload $f
    set en1 [shape_energy $rfsh1 $par(duration)]
    set en2 [shape_energy $rfsh2 $par(duration)]
    set Res [expr $Res - $par(lam)*($en1+$en2)]
    return [format "%.20f" $Res]
}

proc main {} {
    global par rfsh1 rfsh2 limsC limsN optname itercount fout
        tfcomponents

    set tfcomponents [list 0.0 0.0]

    set par(duration) 600
    set par(Norig) 600
    # Load shapes from optimization for CS robustness
    set rfsh1 [load_shape shape_lev2_H_final.dat]
    set rfsh2 [load_shape shape_lev2_N_final.dat]
    set par(averaging_file) HN_6_7.ave

    # Level 3: All robustness constraints in optimization
    set optname shape_lev3
    set par(rfmap) coil_1p3_HN_2newplugs_normweight_asymH0N0.dat
    set fout [open $optname\_output.txt w]
```

```
    set par(pulse_sequence) pulseq_OC_rotmod
    set itercount 0
    set par(oc_method) CG
    set par(oc_max_iter) 3000
    set tfopt [oc_optimize $rfsh1 -max 100000 $rfsh2 -max 60000]
    save_shape $rfsh1 $optname\_final_H.dat
    save_shape $rfsh2 $optname\_final_N.dat
    close $fout

    free_all_shapes
}
```

B.2 Input file for optimization of shapes composed of repetitive elements

Based on code from Zdeněk Tošner.

```
spinsys {
# NH pair from ubiquitin structure
    channels 1H 15N
    nuclei   1H 15N
    shift 1 0p 7.7p 0.65 112.6 134.15 73.352
    shift 2 0p 99p 0.19 -48.529 62.139 160.36
    dipole 1 2 10400 0 106.01 -32.815
    jcoupling 1 2 -92 0 0 0 0 0
}

par {
    method   direct dsyev
    spin_rate 55000
    crystal_file rep3_112.cry
    gamma_angles 1
    variable Nspins 2
    variable recalc pow(2,2-Nspins)
    variable lam 2.0e-9

    averaging_file ave/HN_2sp_5_4.ave
    rfmap coil_1p3_HN_2newplugs_normweight_asymH0N0.dat
```

```
    start_operator       I1x
    detect_operator      I2x
    proton_frequency     800e6
    sw                   1e6

    # Parallelization is done via MPI, num_cores per thread therefore 1
    num_cores 1

    oc_grad_level 2

    oc_var_save_iter 1
    oc_var_save_proc rfstore

    # This MUST be used when working with optimal control!
    conjugate_fid false
}

proc rfstore {} {
# Storage of intermediate pulses during the optimization process
    global par rfsh1 rfsh2 optname itercount tempstore fn

    incr itercount $par(oc_var_save_iter)

    save_shape $rfsh1 shapes/$optname\_H_temp_$itercount\.dat
    save_shape $rfsh2 shapes/$optname\_N_temp_$itercount\.dat
    puts $fn "Iter␣$itercount␣[format␣"%10.6f"␣[lindex␣$tempstore␣0]]␣
        penalty␣[format␣"%10.6f"␣[lindex␣$tempstore␣1]]␣"
    flush $fn
}

proc pulseq_OC {} {
# Optimization without 3D rf inhomogeneity
    global par rfsh1 rfsh2 rfsh3 rfsh4 dur pregrad postgrad gradswitch

    if {$gradswitch == 1} {
        reset
        for {set i 0} {$i < $pregrad} {incr i} {
            pulse_shaped $par(duration) $rfsh3 $rfsh4
        }
        pulse_shaped $par(duration) $rfsh1 $rfsh2
        for {set i 0} {$i < $postgrad} {incr i} {
            pulse_shaped $par(duration) $rfsh3 $rfsh4
        }
```

```
        oc_acq_hermit
    } else {
        reset
        for {set i 0} {$i < $dur} {incr i} {
            pulse_shaped $par(duration) $rfsh1 $rfsh2
        }
        oc_acq_hermit
    }
}

proc pulseq_OC_rotmod {} {
# Optimization with 3D rf inhomogeneity
    global par rfsh1 rfsh2 rfsh3 rfsh4 dur pregrad postgrad gradswitch

    if {$gradswitch == 1} {
        reset
        for {set i 0} {$i < $pregrad} {incr i} {
            pulse_shaped_rotormodulated $par(duration) $rfsh3 $rfsh4
        }
        pulse_shaped_rotormodulated $par(duration) $rfsh1 $rfsh2
        for {set i 0} {$i < $postgrad} {incr i} {
            pulse_shaped_rotormodulated $par(duration) $rfsh3 $rfsh4
        }
        oc_acq_hermit
    } else {
        reset
        for {set i 0} {$i < $dur} {incr i} {
            pulse_shaped_rotormodulated $par(duration) $rfsh1 $rfsh2
        }
        oc_acq_hermit
    }
}

proc gradient {} {
    global par rfsh1 rfsh2 rfsh3 rfsh4 dur pregrad postgrad gradswitch

    set gradswitch 1

    set rfsh3 [shape_dup $rfsh1 0]
    set rfsh4 [shape_dup $rfsh2 0]

    # FID length needs to be equal to number of optimized variables
    set par(np) [expr 2*$par(Norig) ]
```

```
    set f [fcreate -np $par(np) -sw $par(sw)]

    # Gradient calculation for every position of the repetitive
    # element within the pulse and summation
    for {set i 0} {$i < $dur} {incr i} {
        set pregrad $i
        set postgrad [expr $dur - $i - 1]
        set g [fsimpson]
        fadd $f $g
        funload $g
    }

    free_shape $rfsh3
    free_shape $rfsh4

    oc_grad_add_energy_penalty $f $rfsh1 -$par(lam) $rfsh2 -$par(lam)

    fscale $f -scale $par(recalc)
    return $f
}

proc target_function {} {
    global par rfsh1 rfsh2 rfsh3 rfsh4 gradswitch enpen tempstore

    set rfsh3 [shape_dup $rfsh1 0]
    set rfsh4 [shape_dup $rfsh2 0]

    set gradswitch 0
    set par(np) 1

    set f [fsimpson]
    set Resraw [expr [findex $f 1 -re]*$par(recalc) ]
    funload $f

    set en1 [shape_energy $rfsh1 $par(duration)]
    set en2 [shape_energy $rfsh2 $par(duration)]
    set Res [expr $Resraw - $par(lam)*($en1+$en2)]
    set enpen [expr $par(lam)*($en1 + $en2)]

    free_shape $rfsh3
    free_shape $rfsh4

    set tempstore [list $Resraw $enpen]
```

```
    return [format "%.20f" $Res]
}

proc main {} {
    global par rfsh1 rfsh2 limsN limsH optname dur enpen itercount
        tempstore fn

    # Number of rotor periods per repetitive element
    set numperiods 3
    # dur = number of repetitive elements in pulse
    set dur 14
    set run 1

    set itercount 0
    # Level 3: All robustness constraints in optimization
    set optname rep_elem_$numperiods\periods_run$run\_lev3
    set fn [open $optname\_results.txt w]
    set enpen 0.0
    set tempstore [list 0.0 0.0]

    set par(duration) [expr ($numperiods * 1.0e6) / $par(spin_rate)]
    set par(lam) [expr $dur * 2.0e-9]
    set par(Norig) [expr $numperiods * 20]

    # Load shapes from optimization for CS robustness
    set rfsh1 [load_shape shape_lev2_H_final.dat]
    set rfsh2 [load_shape shape_lev2_N_final.dat]
    set par(pulse_sequence) pulseq_OC_rotmod
    set par(oc_method) CG
    set par(oc_max_iter) 2000
    set tfopt [oc_optimize $rfsh1 -max 100000 $rfsh2 -max 70000]
    save_shape $rfsh1 $optname\_H.dat
    save_shape $rfsh2 $optname\_N.dat

    puts $fn "$optname␣[format␣"%10.6f"␣$tfopt]␣penalty␣[format␣"%10.6f"
        ␣$enpen]␣"

    flush $fn
    free_all_shapes
}
```

B.3 Input file for semi-spin-state selective optimization

Based on code from Zdeněk Tošner and Kasimir Buhr.

```
spinsys {
# NH pair from ubiquitin structure
    channels 1H 15N
    nuclei   1H 15N
    shift 1 0p 7.7p 0.65 112.6 134.15 73.352
    shift 2 0p 99p 0.19 -48.529 62.139 160.36
    dipole 1 2 10400 0 106.01 -32.815
    jcoupling 1 2 -92 0 0 0 0 0
}

par {
    method   direct dsyev
    spin_rate 55000
    crystal_file rep3_128.cry
    gamma_angles 1

    start_operator       I1b*I2x I1b*I2x I1b*I2x I1b*I2x I1b*I2y I1b*I2y
        I1b*I2y I1b*I2y
    detect_operator      I1x*I2a I1x*I2b I1y*I2b I1y*I2a I1x*I2b I1x*I2a
        I1y*I2b I1y*I2a
    # Operators:         wanted  --------- UNWANTED
       ------------------------------------

    proton_frequency     800e6
    sw                   1e6

    # Intel Xeon Phi cluster, 4-way hyperthreading per core
    num_cores 4

    variable lam 2.0e-9
    oc_grad_level 2
    oc_var_save_iter 5
    oc_var_save_proc rfstore

    # This MUST be used when working with optimal control!
    conjugate_fid false
}
```

```
proc rfstore {} {
# Storage of intermediate pulses during the optimization process
    global par rfsh1 rfsh2 optname vals storetotal itercount fn pen

    incr itercount $par(oc_var_save_iter)
    save_shape $rfsh1 shapes/$optname\_H_temp_$itercount\.dat
    save_shape $rfsh2 shapes/$optname\_N_temp_$itercount\.dat
    puts $fn "Iteration␣$itercount␣[format␣"%10.6f"␣$storetotal]␣:␣
        I1x*I2a␣=␣[format␣"%10.6f"␣[lindex␣$vals␣0]]␣:␣I1x*I2b␣=␣[format
        ␣"%10.6f"␣[lindex␣$vals␣1]]␣:␣penalty␣=␣[format␣"%10.6f"␣$pen]␣"
    flush $fn
}

proc pulseq_OC {} {
# Optimization without 3D rf inhomogeneity
    global par rfsh1 rfsh2

    reset
    pulse_shaped $par(duration) $rfsh1 $rfsh2
    oc_acq_hermit
}

proc pulseq_OC_rotmod {} {
# Optimization with 3D rf inhomogeneity
    global par rfsh1 rfsh2

    reset
    pulse_shaped_rotormodulated $par(duration) $rfsh1 $rfsh2
    oc_acq_hermit
}

proc gradient {} {
    global par rfsh1 rfsh2

    # FID length needs to be equal to number of optimized variables
    set par(np) [expr 2*$par(Norig) ]
    set f [fcreate -np $par(np) -sw $par(sw)]
    # Calculate gradients for all start-detect operator pairs at once
    set g [fsimpson]

    # Split gradients into separated gradient vectors
    set gg [fsplit $g]
    set g1 [lindex $gg 0]
```

```
set g2 [lindex $gg 1]
set gbx2 [lindex $gg 2]
set gbx3 [lindex $gg 3]
set gby1 [lindex $gg 4]
set gby2 [lindex $gg 5]
set gby3 [lindex $gg 6]
set gby4 [lindex $gg 7]

# Get oc_acq_* values
set v1 [lindex $par(_phivals_) 0]
set v2 [lindex $par(_phivals_) 1]
set bx2 [lindex $par(_phivals_) 2]
set bx3 [lindex $par(_phivals_) 3]
set by1 [lindex $par(_phivals_) 4]
set by2 [lindex $par(_phivals_) 5]
set by3 [lindex $par(_phivals_) 6]
set by4 [lindex $par(_phivals_) 7]
funload $g

# Combine data into complete gradient
# Wanted part
fadd $f $g1
funload $g1

# Unwanted parts: Subtracted from wanted part
set scl [expr 2.0*$v2*$par(penalty_factor)]
if {$scl<1e-4} {set scl 0.0}
fscale $g2 -scale $scl
fsub $f $g2
funload $g2

set scl [expr 2.0*$bx2*$par(penalty_factor)]
if {$scl<1e-4} {set scl 0.0}
fscale $gbx2 -scale $scl
fsub $f $gbx2
funload $gbx2

set scl [expr 2.0*$bx3*$par(penalty_factor)]
if {$scl<1e-4} {set scl 0.0}
fscale $gbx3 -scale $scl
fsub $f $gbx3
funload $gbx3
```

```
    set scl [expr 2.0*$by1*$par(penalty_factor)]
    if {$scl<1e-4} {set scl 0.0}
    fscale $gby1 -scale $scl
    fsub $f $gby1
    funload $gby1

    set scl [expr 2.0*$by2*$par(penalty_factor)]
    if {$scl<1e-4} {set scl 0.0}
    fscale $gby2 -scale $scl
    fsub $f $gby2
    funload $gby2

    set scl [expr 2.0*$by3*$par(penalty_factor)]
    if {$scl<1e-4} {set scl 0.0}
    fscale $gby3 -scale $scl
    fsub $f $gby3
    funload $gby3

    set scl [expr 2.0*$by4*$par(penalty_factor)]
    if {$scl<1e-4} {set scl 0.0}
    fscale $gby4 -scale $scl
    fsub $f $gby4
    funload $gby4

    oc_grad_add_energy_penalty $f $rfsh1 -$par(lam) $rfsh2 -$par(lam)

    return $f
}

proc target_function {} {
    global par vals storetotal pen rfsh1 rfsh2

    set par(np) 1
    # All operator pairs calculated at the same time
    set g [fsimpson]

    # Split values for different operator pairs
    set gg [fsplit $g]
    set g1 [lindex $gg 0]
    set g2 [lindex $gg 1]
    set bx2 [lindex $gg 2]
    set bx3 [lindex $gg 3]
    set by1 [lindex $gg 4]
```

```
    set by2 [lindex $gg 5]
    set by3 [lindex $gg 6]
    set by4 [lindex $gg 7]

    # Wanted transfer
    set v1 [expr [findex $g1 1 -re] ]

    # Undesired transfers
    set v2 [expr [findex $g2 1 -re] ]
    set v3 [expr [findex $bx2 1 -re] ]
    set v4 [expr [findex $bx3 1 -re] ]
    set v5 [expr [findex $by1 1 -re] ]
    set v6 [expr [findex $by2 1 -re] ]
    set v7 [expr [findex $by3 1 -re] ]
    set v8 [expr [findex $by4 1 -re] ]

    funload $g
    funload $g1
    funload $g2
    funload $bx2
    funload $bx3
    funload $by1
    funload $by2
    funload $by3
    funload $by4

    set en1 [shape_energy $rfsh1 $par(duration)]
    set en2 [shape_energy $rfsh2 $par(duration)]
    set pen [expr $par(lam)*($en1 + $en2)]

    # Squares of undesired transfers:
    # - To get positive numbers
    # - To make the penalty progressive
    set Res [expr $v1 - $par(penalty_factor)*$v2*$v2 - $par(
        penalty_factor)*$v3*$v3 - $par(penalty_factor)*$v4*$v4 - $par(
        penalty_factor)*$v5*$v5 - $par(penalty_factor)*$v6*$v6 - $par(
        penalty_factor)*$v7*$v7 - $par(penalty_factor)*$v8*$v8]
    set vals [list $v1 $v2 $v3 $v4 $v5 $v6 $v7 $v8]
    set storetotal $Res
    set Res [expr $Res - $pen]
    return [format "%.20f" $Res]
}
```

```
proc main {} {
    global par rfsh1 rfsh2 limsC limsH optname vals itercount fn

    # Level 3: All robustness constraints in optimization
    set optname atob_r1_lev3
    set par(averaging_file) HN_2sp_4_4.ave
    set par(rfmap) rf/coil_1p3_800MHz_H_N_detweights.dat
    set itercount 0
    set run [lindex $::argv 1]
    set fn [open $optname\_results.txt w]

    set dur 600
    set par(duration) $dur
    set par(Norig) $dur
    # Load shapes from optimization for CS robustness
    set rfsh1 [load_shape atob_r1_lev2_final_H.dat]
    set rfsh2 [load_shape atob_r1_lev2_final_N.dat]
    set par(pulse_sequence) pulseq_OC_rotmod
    set par(oc_method) CG
    set par(oc_max_iter) 2000
    set par(penalty_factor) 1.0
    set tfopt [oc_optimize $rfsh1 $rfsh2 ]
    save_shape $rfsh1 $optname\_final_H.dat
    save_shape $rfsh2 $optname\_final_N.dat
    set f [fsimpson]
    set ff [fsplit $f]
    funload $f
    for {set ii 0} {$ii<[llength $par(detect_operator)]} {incr ii} {
        set fii [lindex $ff $ii]
        set vv  [findex $fii 1 -re]
        puts $fn "\t␣␣[lindex␣$par(start_operator)␣$ii]␣[lindex␣$par(
            detect_operator)␣$ii]␣␣␣:␣[format␣"%10.6f"␣$vv]"
        funload $fii
    }
    flush $fn
    free_all_shapes
}
```

C List of previous publications

Weber, B.; **Brandl, M. J.**; Pulido Cendales, M. D.; Berner, C.; Pradhan, T.; Feind, G. M.; Zacharias, M.; Reif, B.; Buchner, J., *A Single Residue Switch Reveals Principles of Antibody Domain Integrity.* Journal of Biological Chemistry 2018, 293 (44), 17107–17118. doi:10.1074/jbc.RA118.005475. *Project is not part of the thesis.*

Tošner, Z.; **Brandl, M. J.**; Blahut, J.; Glaser, S. J.; Reif, B., *Maximizing Efficiency of Dipolar Recoupling in Solid-State NMR Using Optimal Control Sequences.* Science Advances 2021, 7 (42), eabj5913. doi:10.1126/sciadv.abj5913.

Blahut, J., **Brandl, M. J.**, Pradhan, T., Reif, B., Tošner, Z., *Sensitivity-enhanced multidimensional solid-state NMR spectroscopy by optimal-control-based transverse mixing sequences.* Submitted to the Journal of the American Chemical Society 2022.